UC San Diego

UC San Diego Electronic Theses and Dissertations

Title

Structure, chemical dynamics and electron localization in the mineral and surface interface

Permalink

https://escholarship.org/uc/item/1vj3p2tx

Author

Song, Duo

Publication Date

2019

Peer reviewed|Thesis/dissertation

eScholarship.org Powered by the California Digital Library
University of California

UNIVERSITY OF CALIFORNIA SAN DIEGO

Structure, Chemical Dynamics and Electron Localization in the Mineral and Surface Interface

A dissertation submitted in partial satisfaction of the
requirements for the degree
Doctor of Philosophy

in

Chemistry

by

Duo Song

Committee in charge:

Professor John Weare, Chair
Professor Douglas Magde
Professor James Andrew McCammon
Professor Faik Akif Tezcan
Professor Michael Holst

2019

Copyright
Duo Song, 2019
All rights reserved.

The dissertation of Duo Song is approved, and it is acceptable in quality and form for publication on microfilm and electronically:

_____

_____

_____

_____

_____

Chair

University of California San Diego

2019

DEDICATION

This thesis is dedicated to my parents, who always support and encourage me to pursue my PhD degree.

TABLE OF CONTENTS

Signature Page . . . iii

Dedication . . . iv

Table of Contents . . . v

List of Figures . . . viii

List of Tables . . . x

Acknowledgements . . . xi

Vita . . . xiii

Abstract of the Dissertation . . . xiv

Chapter 1 Introduction . . . 1

Chapter 2 First Principle Methods and Applications . . . 5
2.1 Introduction to Kohn-Sham Equation . . . 5
2.2 Introduction to Hubbard-like Coulomb and Exchange (DFT+U) . . . 7
2.3 Introduction to Ab-initio Molecular Dynamics . . . 8
2.4 Introduction to Pseudopotentials . . . 9

Chapter 3 Interface Structure, Dynamics and Reactivity at the Hematite Solution/Interface: H-Bond Formation and Charge Transfer (with Fe^{2+} Solutes) . . . 13
3.1 Introduction . . . 13
3.2 Computational Methods and Computational Cells . . . 18
3.2.1 Computational Methods, Choice of DFT Level and Expansion Basis . . . 18
3.2.2 Computational Cells Structural Details . . . 21
3.2.3 Spin Configurations of Surface Slabs . . . 22
3.3 The (012) Protonation and Water Absorption of Cleaved Surfaces . . . 23
3.3.1 Hematite (012) Surface Protonation Models . . . 23
3.3.2 Water Absorption on Hematite (012) Cleaved Surface . . . 24
3.4 Structural Properties of Interface . . . 26
3.4.1 Hematite (001) Aqueous Interface . . . 26
3.4.2 Hematite (012) Aqueous Interface . . . 30
3.4.3 Fe(II) Absorption on Hematite (001) Aqueous Interface . . . 34
3.4.4 Fe(II) Absorption on Hematite (012) Aqueous Interface . . . 37
3.5 Electronic Structural Properties of Ion Absorption in Interface . . . 39
3.5.1 Projected Density of States Analysis . . . 39
3.5.2 The Mechanism of Electron Transfer . . . 43

Chapter 4 Symmetry Breaking in Density Functional Theory due to Dirac Exchange for a Hydrogen Molecule . . . 44
4.1 Introduction . . . 44
4.2 Proof in the Small α Regime . . . 49
4.2.1 The Restricted Hartree Model: Case $\alpha = 0$ . . . 49
4.2.2 Implicit Function Theorem Analysis for Small α . . . 51
4.2.3 Analysis of the Linearized Operators for $\alpha = 0$ . . . 53
4.2.4 Construction of Solutions near $\alpha = 0$ . . . 55
4.2.5 Construction of the Local Branch under the Symmetry Assumption . . . 58
4.3 Localization and Symmetry Breaking for Large α . . . 59
4.3.1 A Priori Energy Estimate . . . 59
4.3.2 Location Optimization . . . 62
4.4 Numerical Solution to Kohn-Sham SDFT (KS-SDFT) Equations for ψ_+ and ψ_- as a Function of α . . . 66
4.4.1 Overview of Numerical Method (FEM) . . . 67
4.4.2 Numerical Results of DFT/ FEM Calculations . . . 69
4.5 Discussion and Future Works . . . 76

Chapter 5 Impurity Solvers and Dynamic Mean Field Theory Self Consistancy . . . 78
5.1 Introduction to DMFT . . . 78
5.2 Defining the Problem . . . 80
5.3 The Exact Diagonalization Impurity Solver (ED) . . . 83
5.4 The Hirsch-Fye Impurity Solver . . . 92
5.5 Results and Discussion . . . 104

Chapter 6 Summary and future work . . . 110
6.1 Summary . . . 110
6.2 Future Work . . . 111
6.2.1 QM/MM simulation in the interface region . . . 111
6.2.2 Dynamic Mean Field theory . . . 112
6.2.3 Symmetry Breaking . . . 113

Appendix A . . . 115
A.1 Finite Element Set Up . . . 116
A.2 The Generalized Eigenvalue Problem: . . . 118
A.3 Solution to the generalized eigenvalue problem and the associate Coulomb problem . . . 119
A.3.1 Details of the FEniCS solver . . . 120
A.4 The Wavefunction and Orbital Energy update and iteration . . . 121
A.4.1 Some Preliminaries . . . 121
A.4.2 Update of the orbital energy: . . . 123
A.5 The Self Consistent Iteration . . . 126
A.6 Hessian analysis . . . 126

Appendix B 129
B.1 Background equations 130
B.2 Grouping products of exponentials 133
B.3 Calculation of the trace of products of layer propagators of fermion operators 138
B.4 Derivation of the noninteracting G^0 for the Anderson model 141

Bibliography 143

LIST OF FIGURES

Figure 3.1: Hematite (001) and (012) surfaces terminations used in our work 18
Figure 3.2: Water molecule absorbed on different hydration models for hematite (012) surface. (A) and (B) are side-views of Model 1, (C) and (D) are side-views of Model 2. 24
Figure 3.3: Structure of Hematite(001)–water interface 27
Figure 3.4: Radial distribution functions (RDFs) of O'-O for hematite (001) and (012) - water interfaces 29
Figure 3.5: Structure of Hematite(012)–water interface 30
Figure 3.6: Electron density profiles for hematite-water interfaces 31
Figure 3.7: Computed power spectrum of two types of OD groups on hematite (012) surface, water on interfacial region and bulk region 34
Figure 3.8: Radial distribution functions (RDFs) of Fe-O for hematite (001) and (012) - water interfaces 36
Figure 3.9: HOMOs of Fe(II) ions absorbed on hematite (001) and (012) surfaces in aqueous interfaces 38
Figure 3.10: Projected density of states of different atoms in the system which has Fe(II) ion absorbed on hematite (001) in its aqueous interface (Fermi level: 0 eV) 40
Figure 3.11: Projected density of states of different atoms in the system which has Fe(II) ion absorbed on hematite (012) in its aqueous interface (Fermi level: 0 eV) 42

Figure 4.1: A representation of the finite element grid used in calculation. Each triangle represents a tetrahedron in the real calculation. Note that the density of the mesh is significantly increased near the two atomic nuclei (see appendix for further discussion as to how this mesh is generated). 68
Figure 4.2: Bifurcation of LSDA for H_2 in the R dimension with $\alpha = 0.93$. The bifurcation point is at $R = 2.75$ au. 72
Figure 4.3: Several numerically constructed branches of the bifurcation of LSDA for H_2 in the α parameter with $R = 2.0$ au showing the relevant $\psi_\pm$ profiles. . 75
Figure 4.4: The first symmetry breaking bifurcation of LSDA for H_2 as a phase diagram in R and α. Below the line only delocalized states are present while above the line there are both delocalized and localized states. 75

Figure 5.1: Impurity in Lattice right grid in red. The remaining atoms (right side) create a dynamic means field 79
Figure 5.2: DMFT cycle for the Exact Diagonalization (ED) impurity solver. 85
Figure 5.3: DMFT cycle for the Hirsch-Fye QMC impurity solver 92
Figure 5.4: Energy for the Bethe lattice (bandwidth W=4) at $T = 0.1$ in the paramagnetic case 106

Figure A.1: Finite element tetrahedron defining FEM elements and nodes. The L tetrahedral elements are identified by e_l. The global node are indexes by (m). For each element e_l a there is global node at each corner. Generally a local nodes belonging to individual tetrahedra are also defined. see [18, 4, 13, 26].These are not shown and are managed transparently by the Dolfin software [96]. 116

LIST OF TABLES

Table 3.1: Energy difference between different magnetic states configurations for (012) surface 22
Table 3.2: Energy difference between different magnetic states configurations for (001) surface 23
Table 3.3: Interlayer spacing (Å) at the oxygen termination hydrated surface for (001) and (012) surface slabs 28
Table 3.4: Surface hydrogen bonds statistics on hematite (001) and (012) aqueous interfaces (Bond length: Å, Degree: ∘ 32

Table 4.1: Eigenvalues for the Hessian matrix, $\alpha = .93$ for various bond lengths 73

ACKNOWLEDGEMENTS

First and foremost, I would like to express my special appreciation and thanks to my advisor, Professor John H. Weare, for providing me all the opportunities to do the research in his group. This work would not be possible without his guidance and encouragement. He is always patient and supportive, giving me precious advice on my academic research, career and personal life. I could not have imagined having a better advisor and mentor for my Ph.D study.

My sincere thanks also goes to Dr. Eric J. Bylaska at Pacific Northwest National Laboratory for teaching and helping me a lot about the theories and technical skills required in this work. It was a great pleasure working with him in my trips to PNNL. I would also like to genuinely thank my collaborators Professor Jeremy Marzuola at University of North Carolina at Chapel Hill, Professor Jianfeng Lu at Duke University and Professor Michael Holst at University of California San Diego for their helpful discussions and insightful work. I am also extremely grateful to my colleagues and friends Dr. Ying Chen, Dr. Teerapong Pirojsirikul, Dr. Wasut Pornpatcharapong and Dr. Houdong Hu for inspiring me and sharing their experience on physics and chemistry. I would like to extend my deepest gratitude to my other committee members: Professor Michael Holst, Professor Douglas Magde, Professor James Andrew Mccammon and Professor Faik Akif Tezcan for their brilliant comments and support.

Last but not the least, I would especially thank my family: my parents Mr. Huiliang Song and Mrs. Yuehua Lin for giving birth to me and supporting me continuously throughout my life.

Chapter 3, in full, is a reprint of the material “Interface Structure, Dynamics and Reactivity at the Hematite Solution/Interface: H-Bond Formation and Charge Transfer (with Fe^{2+} Solutes)” by Duo Song, Ying Chen, Eric Bylaska and John Weare, in preparation. The dissertation author is the primary investigator and author.

Chapter 4 in full, is a reprint of the material "Symmetry Breaking in Density Functional

Theory due to Dirac Exchange for a Hydrogen Molecule" by Michael Holst, Houdong Hu, Jianfeng Lu, Jeremy L. Marzuola, Duo Song and John Weare, submitted to Journal of Nonlinear Science on March 8 2019, arXiv:1902.03497.

VITA

2010	B. S. in Materials Science and Engineering, University of Science and Technology of China
2012	M. S. in Chemistry, University of California, San Diego
2019	Ph. D. in Chemistry, University of California, San Diego

PUBLICATIONS

Song, D., Chen, Y., Bylaska, E., and Weare, J., "Interface Structure, Dynamics and Reactivity at the Hematite Solution/Interface: H-Bond Formation and Charge Transfer with Fe^{2+} Solutes", in preparation, 2019.

Holst, M., Hu, H., Lu, J., Marzuola, J., Song, D. and Weare, J., "Symmetry Breaking in Density Functional Theory due to Dirac Exchange for a Hydrogen Molecule", submitted to Journal of Nonlinear Science on March 8 2019, arXiv:1902.03497.

ABSTRACT OF THE DISSERTATION

Structure, Chemical Dynamics and Electron Localization in the Mineral and Surface Interface

by

Duo Song

Doctor of Philosophy in Chemistry

University of California San Diego, 2019

Professor John Weare, Chair

Reactions in the mineral surface/reservoir fluid interface control geochemical processes such as the dissolution and growth of minerals. In this dissertation we present properties of hematite bulk, AIMD simulation of structures and reactions (Fe2+ absorption) in the hematite–water interfaces region with intension of interpreting the structure of the reactive interface region, the dynamics of the water, solute molecules and atoms in this region and the electronic structure associated with hydrogen and covalent bond formations.

We also study symmetry breaking in the mean field solutions to the 2 electron hydrogen molecule within Kohn Sham (KS) local spin density function theory with Dirac exchange (the

XLDA model). This simplified model shows behavior related to that of the (KS) spin density functional theory (SDFT) predictions in condensed and molecular systems. The Kohn Sham solutions to the constrained SDFT variation problem undergo spontaneous symmetry breaking as the relative strength of the non-convex exchange term increases. This results in the change of the molecular ground state from a paramagnetic state to an antiferromagnetic ground states and a stationary symmetric delocalized 1st excited state. We further characterize the limiting behavior of the minimizer when the strength of the exchange term goes to infinity. The stability of the various solution classes is demonstrated by Hessian analysis. Finite element numerical results provide support for the formal conjectures.

In Chapter 1 experimental and theoretical backgrounds and progress are introduced. In Chapter 2 computational methods including first principle methods and AIMD are briefly introduced. In Chapter 3 simulations of surface and aqueous fluid interfaces of hematite (001) and (012) are carried out. Projected density of states for interfacial atoms, water adsorption process on surface, hydrogen bond analysis, electron density profiles and etc are investigated. In Chapter 4 symmetry breaking in density functional theory due to Dirac exchange for a Hydrogen molecule is studied. In Chapter 5 Dynamic Mean Field Theory method and applications are presented. In Chapter 6 summary and future work are discussed.

Chapter 1

Introduction

Many environmental processes such as waste containment (e.g., permanent CO2 sequestration, nuclear waste release to biosphere), soil and mineral formation, and oxidation/reduction reactions are controlled by transport in the fluid phase [8, 120] and chemical events at the mineral/solution interface [20, 22, 68, 102, 104, 140, 151]. To evaluate the impact of these processes on energy production and management strategies it is essential to have a high level of understanding of the responses of geological formations to interactions with reservoir fluids. The interpretation of chemical processes in these systems presents major challenges. For example, the solids involved may be extremely heterogeneous materials and be composed of transition metal oxides with highly correlated and complex electronic structure and the structure and composition of the interface and solution (e.g., solute ion associations and hydrolysis products) are likely to be poorly determined [8, 20, 68, 132]. In addition, natural systems may be exposed to extreme pressure and temperature conditions (P to several kBars and T to 500°C) and these processes typically occur on time scales much longer than can be observed in the laboratory. To answer these challenging modeling problems direct simulation using petascale and higher computer architectures is expected to play an increasingly larger role. However, despite impressive progress the time scales and chemical complexity of these

problems still challenge present day simulation approaches. The progress of mineral surface and fluid interface studies can be divided into three main areas. Each is described below.

1. Structure, chemical dynamics and electron localization in the mineral/ surface interface: The breaking of symmetry at the mineral surface and the disorder of the interface regions create a difficult modeling problem for condensed matter theories. It is electron transport/transfer processes between transition metal oxides (hematite α-Fe_2O_3) [73] and oxyhydroxides (e.g., goethite, α-FeOOH) and reduced metal ions (e.g., Fe2+(aq)/Fe3+(crys.) electron exchange) in the interface region [85, 123, 124, 151]. Specific targets are the calculation and optimization of surface interface reconstructions [32, 33] using various higher levels of electronic structure methods, identification of reactions paths in the interface region (e.g., Fe2+ absorption) and the initiation of studies of electron transport (oxidation/reduction) in the interface region [76, 123, 124, 151]. There are a considerable number of recent measurements in these systems which will provide a rich database [31, 32, 33, 56] for quantification of theoretical predictions and new insights into the surface structure of these complex materials. Well-developed software tools also contribute to the solution of these problems.

2. Structure and dynamic of aqueous solutes including those in extreme environments: The interpretation of chemical and transport properties in geological systems is difficult because the structure, solute composition (e.g., ion paired and hydrolysis species) and dynamics of solute species in aqueous solutions [8, 120, 132] are complicated and difficult to observe. This problem is more severe for system under extreme conditions of temperature and pressure. Theoretical paths provide an important support for the development of high resolution EXAFS spectroscopy as a tool to interpret the aqueous solutions as well as new information about reservoir fluid properties (e.g. hydrolysis, hydration shell composition and speciation in the Fe(II)(III), Al(III) and Mg(II) aqueous systems).

3. Development of new petascale and distributed computing (cloud) based computational tools required to treat the highly correlated nature, structural complexity and long time

scales encountered in geochemical problems: The two major bottlenecks in direct simulation of geochemical processes are the need to accurately represent the atomic level forces in the system and the very long time scales that may be encountered (e.g., in chemical reactions) in the application. Lack of symmetry further complicates the applications. The development of the theory, numerical methods and implementations are required to treat complex chemical processes in the interface region at the electronic structure level. These include scalable density functional (DFT) methods of solutions to electronic structure problems, highly scalable hybrid density functional methods (DFT+exact exchange) [113, 155], DFT+U [111] methods and the development of methods that more accurately account for the correlated nature of the electrons in metal oxide materials (DMFT [55, 81]). New simulation methods are explored to increase the time scale of dynamical simulations by replacing the usual sequential methods of molecular dynamics by parallel implementation of forward in time integrations [54, 91]. These methods have the potential to utilize information from less precise physical model simulations to accelerate the performance of complex models (e.g., accelerate the MD performance of high level 1st principle electronic structure methods). The development of sampling methods [7] support the efficient exploration of complex many-body potential landscapes. The target of these methods would be reactions in the mineral surface/fluid interface [7, 45] and the more complete understanding of speciation in solutions [8, 120, 132] required for interpretation of solute transport, ore formation, etc..

Iron oxides contain partially filled, very localized 3d atomic orbitals. While for these systems the usual application of density function methods leads to reasonable structural properties, the prediction of other properties such as band gaps are very poor. Even more important to the oxidation/reduction processes [73, 151] that we are interested in, electron localization and spin polarization prediction are qualitatively incorrect. The inclusion of exact exchange in the DFT calculations methods provide a more realistic description of electron correlation and are still efficient enough to allow dynamical simulation. To carry out these

types of calculation required the development of a fast and scalable exchange algorithm.

The most popular approximation to the electronic Schrödinger equations used for AIMD is local DFT based on computationally efficient approximations to the exact exchange-correlation functional (e.g. GGA). While DFT+GGA type calculations seem to predict structures quite well it is becoming clear that augmentation with some fraction of exact exchange (hybrid-DFT, e.g. PBE0) is needed for many systems. Examples of interest include charge localization in transition elements with tightly bound d electrons in oxide materials [41, 144] (e.g. Fe_2O_3, TiO_2), the underestimation of reaction barriers and band gaps in solids [98, 130, 131] and accurate predictions of spin structure of solids and nanoparticles [37]. The drawback of hybrid-DFT is that it adds a significant amount of expense to an already expensive AIMD simulation.

The object of this thesis is to describe our efforts to address the application and development of 1st principle based dynamical simulation methods to study: the complicated highly correlated electronic structure of minerals; the unusual bonding found in the mineral/fluid interface region; the structure of ions and hydrolysis products in solution; electron localization in the interface region and the development of the new methods to more efficiently reach the long time scale required to simulate the problems encountered in geochemical problems. The calculations of bulk, surface and interface have been done using the NWChem software which can be downloaded from `http://www.nwchem-sw.org/index.php/Download`. These application packages have been designed for implementation on highly parallel computers.

Chapter 2

First Principle Methods and Applications

2.1 Introduction to Kohn-Sham Equation

The calculation of the electronic structure of a highly correlated system is a problem of current interest in condensed matter physics [82]. Fortunately there is an approximate approach, the density functional theory of Hohenberg, Kohn and Sham [69, 80, 106], which provides estimates of many properties at a practical computational cost. Though not expected to provide more than qualitative accuracy for spin dependent properties essentially all AIMD methods implement this approach. To clarify the following discussion it will be useful to briefly outline some of the aspects of this theory that affect the accuracy of the simulations and its application to highly correlated systems.

Hohenberg and Kohn demonstrated that the total electronic energy of a many electron system may be written as a functional of the electron density [69, 80, 106]. That is,

$$E[n(\vec{r}),\vec{R}_\alpha] = \sum_i \langle \psi_i^{\mathrm{KS}} | -\frac{1}{2}\nabla^2 | \psi_i^{\mathrm{KS}} \rangle + \int V_{\mathrm{ext}}(\vec{r},\vec{R}_\alpha) n(\vec{r}) d\vec{r} + \frac{1}{2}\int\int \frac{n(\vec{r})n(\vec{r}')}{|\vec{r}-\vec{r}'|} d\vec{r}\, d\vec{r}' + E_{\mathrm{XC}}(n(\vec{r})) \tag{2.1}$$

In Eq. (2.1), $E[n(\vec{r}), \vec{R}_\alpha]$ is the total electronic energy and is a function of the electron density,

$$n(\vec{r}) = \sum_{i,\text{occupied}} |\psi_i^{\text{KS}}(\vec{r})|^2 \tag{2.2}$$

and the atomic positions $\vec{R}_\alpha$. $E_{\text{ex}}(n(\vec{r}))$ is the exchange-correlation energy defined in Hohenberg and Kohn [69, 106].The existence of the functional $E_{\text{ex}}(n(\vec{r}))$ is demonstrated by the Hohenberg Kohn theorem but the form as a function of density is still a topic of much research [9, 23]. In Eq. (2.1), ψ_i^{KS} are the Kohn Sham (KS) orbital wave functions [80] found from the constrained variation of the total energy as [106],

$$\Big[-\frac{1}{2}\nabla^2 + V_{\text{ext}}(\vec{r}, \vec{R}_\alpha) + \frac{1}{2}\int d\vec{r}\,' \frac{n(\vec{r}\,')}{|\vec{r} - \vec{r}\,'|} + V_{\text{XC}}(n(\vec{r})) \Big] \psi_i^{\text{KS}} = \epsilon_i \psi_i^{\text{KS}} \tag{2.3}$$

The orbital KS functions must be constrained to be orthonormal,

$$\langle \psi_i^{\text{KS}} | \psi_j^{\text{KS}} \rangle = \delta_{ij} \tag{2.4}$$

$V_{\text{exc}}(n(\vec{r}\,'))$ is the exchange correlation function defied by functional variation of Eq.(2.1). The many-body wave function for all electrons is formed from the simple product of the KS wave functions as,

$$\Psi = \prod_{i,\text{filled}} \psi_i^{\text{KS}}(\vec{r}_i) \tag{2.5}$$

2.2 Introduction to Hubbard-like Coulomb and Exchange (DFT+U)

Most exchange-correlation functionals in DFT framework are generated from expansions around homogeneous electron gas limit. But when the systems have localized electrons, DFT predicts electronic states that can be significantly away form the localized states.

Inspired by the Hubbard model, DFT+U can be used to model strongly correlated systems. A Hubbard term (on-site Coulomb and exchange) is added to the DFT functional for strongly correlated electrons for strongly correlated electrons (d, f, ... electrons) and a regular DFT functional is still used on other valence electrons.

The Hubbard term is expressed using Slater integrals and local occupation matrix

$$\begin{aligned} E_{\text{Hubbard}} &= \tfrac{1}{2}\sum_{I,\sigma}\sum_{m,n,x,y}\rho^{I,\sigma}_{mn}\rho^{I,-\sigma}_{xy}\langle\chi^I_m\chi^I_x|\,V_{ee}\,|\chi^I_n\chi^I_y\rangle \\ &+ \tfrac{1}{2}\sum_{I,\sigma}\sum_{m,n,x,y}\rho^{I,\sigma}_{mn}\rho^{I,\sigma}_{xy}\Big(\langle\chi^I_m\chi^I_x|\,V_{ee}\,|\chi^I_n\chi^I_y\rangle - \langle\chi^I_m\chi^I_n|\,V_{ee}\,|\chi^I_x\chi^I_y\rangle\Big) \end{aligned} \tag{2.6}$$

$$\rho^{I,\sigma}_{mn} = \sum_k f_k \langle\chi^I_m|\phi^\sigma_k\rangle\langle\phi^\sigma_k|\chi^I_n\rangle \tag{2.7}$$

However, due to some fragments of Coulomb interactions included in the Hartree and exchange-correlation terms in DFT functional, the double-counting problem exists. The double-counting term can be derived and subtracted from the total energy functional.

$$E_{\text{DFT+U}} = E_{\text{DFT}} + E_{\text{Hubbard}}[\{\rho^{I,\sigma}_{mm}\}] - E_{\text{DC}}[\{\rho^{I,\sigma}\}] \tag{2.8}$$

where

$$E_{\text{DC}} = \frac{1}{2}\bar{U}\sum_I N^I_\sigma N^I_{-\sigma} + \frac{1}{2}(\bar{U}-\bar{J})\sum_I\sum_\sigma N^I_\sigma(N^I_{-\sigma}-1) \tag{2.9}$$

N is the trace of local occupation matrix. $\bar{U}$ and $\bar{J}$ are the average Coulomb and exchange parameters. Different approaches are used to calculate those two numbers. Dudarev et al. [46] used those two average parameters to replace Slater integrals in equation, and DFT+U functionals have been simplified. In this approach, only $\bar{U}$ and $\bar{J}$ is meaningful.

$$E_{\mathrm{DFT+U}} = E_{\mathrm{DFT}} + \frac{1}{2}(\bar{U} - \bar{J}) \sum_{I,\sigma} \left(\sum_{j} \rho_{jj}^{I,\sigma} - \sum_{j,l} \rho_{jl}^{I,\sigma} \rho_{lj}^{I,\sigma} \right) \tag{2.10}$$

2.3 Introduction to Ab-initio Molecular Dynamics

The dynamics of the system in our work is calculated from the solution to the KS equations, Eq.(2.3). The atomic forces are given by the Hellmann-Feynmann theorem,

$$\vec{F}_{\alpha}(\vec{R}_{\alpha}) = -\langle \Psi | \frac{\partial E}{\partial \vec{R}_{\alpha}} | \Psi \rangle \tag{2.11}$$

Given the forces we can write Newton's equations of motions as

$$M_{\alpha} \ddot{\vec{R}}_{\alpha} = \vec{F}_{\alpha}. \tag{2.12}$$

Time integration of Eq. (2.12) provides the 1st principle dynamics of the system of particles (AIMD) by the KS equations, Eq. (2.3). Car and Parrinello (CP) [29] have introduced a modification of Eqs. (2.3) to (2.13) that leads to a more efficient algorithm. These equations are used in most of the dynamical calculations reported below. In this algorithm the dynamical variables are expanded to include the KS wavefunctions and fictitious dynamical equations. Lagrange multipliers, ϵ_{ij}, maintain orthogonality between the KS orbitals. The dynamical equations for this approach are modified to be [35],

$$\mu\ddot{\Psi}_i^{\mathrm{KS}} = \left[-\frac{1}{2}\nabla^2 + V_{\mathrm{ext}}(\vec{r},\vec{R}_\alpha) + \frac{1}{2}\int d\vec{r}\,' \frac{n(\vec{r}\,')}{|\vec{r}-\vec{r}\,'|} + V_{\mathrm{xc}}(n(\vec{r})) \right] \Psi_i^{\mathrm{KS}} - \sum_{i,\mathrm{filled}} \epsilon_{ij}\Psi_i^{\mathrm{KS}}. \tag{2.13}$$

In Eq. (2.13), $\ddot{\Psi}_i^{\mathrm{KS}}$ is the fictitious acceleration of the KS wavefunction. A corresponding fictitious kinetic energy K.E. of the wavefunction degree of freedom may also be computed. The magnitude of K.E. is controlled by the fictitious mass μ and must be kept small for realistic dynamics for the real position variables, $\vec{R}_\alpha(t)$. This propagation must be carried out with the orthonormality constraints, Eq. (2.4) held tight [29, 99, 115].

2.4 Introduction to Pseudopotentials

The variation/strength of the atom center electron potential, V_{ext}, must be reduced in order for KS wave functions to be expanded in a reasonable number of terms. In order to do this pseudo potentials have been developed [110]. These are widely used nevertheless it is typical to have to modify these functions to obtain the accuracy required for a particular calculation. A significant advance in the development of the pseudopotential method was made by Hamann, Schluter and Chiang (HSC) [62] with the introduction of norm conserving psuedopotentials. While there are differences between various approaches, all popular pseudopotential adopt the basic prescription of HSC. These methods have been highly developed in the condensed matter community and are well explained and reviewed (see for example the detailed review of Pickett [110] and the original papers cited therein). The basic idea of pseudopotential is that the core region of the atomic potential is replaced by a much slower varying function designed to specifically reproduce the behavior of the valance wave functions in regions outside the core (presumed to be the bonding region). The smoothed potential has a nodeless solution that can be expanded by a smaller plane-wave basis. It can be shown that with proper care,

replacing the atomic potential with a pseudopotential will produce the same solutions beyond the region of replacement, while also maintaining the normalization of the orbital function.

Pseudopotentials are derived from 1st principle single atom DFT calculations at the same level of approximation (GGA or hybrid exchange) as used in the full many-atom condensed system simulation. These potentials are precomputed before use in the condensed matter calculation so the simulation remains parameter free (no parameters adjusted in the simulation). On the other hand there are issues such as the contribution of the atomic valance structure to the bonding that must be decided before the development of the pseudopotential. These choices will determine the transferability of the pseudopotential from the atomic to the condensed environment. Such issues are carefully discussed in the Picket review. In the calculations reported in the next section the affects of various assumptions will be tested by comparison of calculations to bulk structural observations.

In the HSC approach given the selection of valance orbitals (corresponding to various l to be included in the active space) a pseudopotential for each total angular momentum is found from the direct inversion of the Schrödinger equation (with a selected DFT functional, see Hamann) [61]. This produces a non-local pseudopotential of the form, equation reference goes here

$$V^{\text{pseu}} = V_M^{\text{val}}(\mathbf{r}) + \hat{V}_{\text{ps}}(\mathbf{r},\mathbf{r}') = V_M^{\text{val}}(\mathbf{r}) + \sum_{l,m} Y_{lm}(\hat{\mathbf{r}})\, V_l(\mathbf{r})\delta(\mathbf{r}-\mathbf{r}')\, Y_{lm}^*(\hat{\mathbf{r}}') \tag{2.14}$$

where V_M^{val} is the Coulomb and exchange potential due to the (non active) valance electrons, $Y_{lm}(\hat{\mathbf{r}})$ is the spherical harmonic defined by the angular momentum, l, and magnetic quantum, m, numbers, $\hat{\mathbf{r}}'$ is a unit vector in the $\mathbf{r}'$ direction, and $V_l(\mathbf{r})$ is the radial potential found from the inversion of the DFT solution to the radial Schrödinger equation for the equivalent atomic problem (see HSC). The potential $\hat{V}_{\text{ps}}$ acts on function of $\mathbf{r}$) as,

$$V_{\rm ps}\hat{\psi}(\mathbf{r}) = \int \sum_{l,m} Y_{lm}(\hat{\mathbf{r}})\, V_l(\mathbf{r})\, \delta(\mathbf{r}-\mathbf{r}')\, Y^*_{lm}(\hat{\mathbf{r}}')\, \psi(\mathbf{r}')\, d\mathbf{r}' \tag{2.15}$$

The potential has a semi-local form, neither just local (radial) or fully separable [24]. In this semi-local form, the pseudopotential is computationally difficult to calculate with a plane-wave basis set, since the kernel integration is not separable in $\mathbf{r}$ and $\mathbf{r}'$ [24]. To produce a more efficient calculation while retaining as much of the atomic form as possible Kleinman and Bylander approximated the form by,

$$\hat{V}^{\rm KB}_{\rm ps}(\mathbf{r},\mathbf{r}') = V_{\rm local}(\mathbf{r}) + \sum_{l,m} P_{lm}(\mathbf{r})\, h_l P^*_{lm}(\mathbf{r}') \tag{2.16}$$

where the atom-centered projectors $P_{lm}(\mathbf{r})$ are of the form

$$P_{lm}(\mathbf{r}) = \Big[V_l(\mathbf{r}) - V_{\rm local}(\mathbf{r}) \Big] \tilde{\phi}_l(\mathbf{r})\, Y_{lm}(\hat{\mathbf{r}}) \tag{2.17}$$

and the coefficient h_l is

$$h_l = \Big\{ 4\pi \int_0^\infty \tilde{\phi}_l(\mathbf{r}) \Big[V_l(\mathbf{r}) - V_{\rm local}(\mathbf{r}) \Big] \tilde{\phi}_l(\mathbf{r})\, r^2 d\mathbf{r} \Big\}^{-1} \tag{2.18}$$

where $\tilde{\phi}_l(\mathbf{r})$ are the zero radial node pseudowavefunctions of the potentials, $V_l(\mathbf{r})$,calculated in the atomic environment. Note that $\hat{V}^{\rm KB}_{\rm ps}\,|\tilde{\phi}_l(\mathbf{r}Y_{lm}\rangle = V_l\,|\tilde{\phi}_l(\mathbf{r}Y_{lm}\rangle$, i.e., that the fully non-local KB form preserves the form of the potential in the atomic problem. The choice of the local potential $V_{\rm local}(\mathbf{r})$ is somewhat arbitrary, but for transition metals it is often chosen to be the $V_{l=0}(\mathbf{r})$ potential. A larger series expansion in pseudowavefunctions can be used to improve the fully local description of the semi-local form. This leads to the general form

$$\hat{V}_{\rm ps}(\mathbf{r},\mathbf{r}') = V_{\rm local}(\mathbf{r}) + \sum_{l,m}\sum_{n,n'} P_{nlm}(\mathbf{r})\, h^{n,n'}_l\, P^*_{n'lm}(\mathbf{r}') \tag{2.19}$$

There is a large body of literature describing pseudopotential methods and illustrating the accuracy and efficiency of this approach [110] For use in the structural the pseudopotentials are developed entirely from fitting atomic calculations and, therefore, should not be considered as part of the data fitting process. Nevertheless, there are questions about accuracy of the representation given by Eq.(2.16), e.g. how many $\tilde{\phi}_{nl}(\mathbf{r})$ are required in the sum in Eq. (2.19) to accurately represent the valance structure of the condensed system and how much of the unscreened atomic potential is assigned as the core region (roughly speaking the region removed). This is a function of the atomic structure of the particular element (e.g., separation of the highest filled lowest excited states, highest valence states etc.). The radius of the region of replacement of the external with the pseudopotential form determines to a large extent the smoothness of the pseudo potential (the larger the region the smoother the pseudopotential). However, if this region is too large the bond formation will be effected and the pseudopotential representation will produce incorrect bonding results.

$$E_{\text{psp}} = \sum_{\sigma=\uparrow,\downarrow} \sum_{i=1}^{n_{\text{elc}}^{\sigma}} \sum_{I=1}^{n_{\text{ion}}} \left(\langle \psi_i^{\sigma} | \, V_{\text{local}}^{I} \, | \psi_i^{\sigma} \rangle + \sum_{l=0}^{l_{\text{max}}^{I}} \sum_{m=-l}^{l} \sum_{n=1}^{n_{\text{max}}^{I}} \sum_{n'=1}^{n'^{I}_{\text{max}}} \langle \psi_i^{\sigma} | P_{nlm}^{I} \rangle \, h_l^{I,n,n'} \, \langle P_{n'lm}^{I} | \psi_i^{\sigma} \rangle \right) \tag{2.20}$$

Chapter 3

Interface Structure, Dynamics and Reactivity at the Hematite Solution/Interface: H-Bond Formation and Charge Transfer (with Fe^{2+} Solutes)

3.1 Introduction

As the reactive center of one of the most abundant minerals in the Earth's surface, the interfaces of α-Fe_2O_3 (hematite) [42] and their interaction with formation fluids provide the environment in which many important geochemical and geobiological reactions occur [72, 119, 133, 149, 151]. The interpretation of these processes at the atomic-level (in surfaces, layered water structures and ion adsorptions on the hematite-water interface) is essential and fundamental information for understanding the evolution of geochemical systems [21].

However, building such an interpretation is complicated by the high heterogeneity of natural materials, the structural and bonding complexity of Hematite bulk and surfaces,

the lack of understanding of bond formation in the interface, and the complex and highly dynamical nature of the interface fluids. Direct dynamical simulation of mineral interfaces (molecular dynamics) and their associated fluid regions provides a means to handle both the many body atomic interactions in these systems and the complex dynamical behavior of the interface region at least for well determined systems (simple interface compositions and cleanly terminated surfaces).

Conventional molecular dynamics (CMD) using relatively simple interatomic potentials (empirical potentials) fit to limited structural data to describe the interactions at the atomic level has been used to study the hematite-water interface. CMD probes both the dynamics and equilibrium structure of the system and has become a powerful tool for molecular and condensed matter modeling. [71, 75, 76] Direct CMD simulation supports the calculation of the dynamics of very large systems and relative long time scales. However, the reliability of CMD predictions is limited because of the uncertainties associated with the atomic level potential descriptions used in this method. Even for situations in which the chemistry is changing in rather straightforward ways (surface termination) the effects of subtle local electronic structure changes cannot be captured using empirical potentials parameterized from bulk structures. In addition, atomic interactions are particularly difficult to describe with simple potential interactions when bond breaking and formation events are important to the desired interpretation. There also are significant problems with the transferability of empirical potentials to treat a range of thermodynamic constraints (composition, X, T and P). These problems are especially difficult for mineral containing transition metal elements (transition oxides, e.g. hematite) because of the strongly correlated behavior of their tightly bound d and f electrons and the possibility of differences in bond formation for different spin ordering.

Because of the lack of the direct relation of empirical potentials to the underlying electronic properties of atomic systems, ab-initio molecular dynamics (AIMD), based on the use of direct 1st principle based electronic structure calculations to estimate interatomic forces

are increasingly being used to treat condensed matter systems [99, 29]. These methods are generalizable to large ranges of thermodynamic variables, spin ordered systems and bond breaking and formation events. However, the need for on-demand evaluations of interatomic forces from electronic structure calculations is computationally very demanding. The improving performance of DFT algorithms and availability of emerging higher performance computers [83] makes these calculations more manageable. However, system sizes and total system time evolution are very much smaller than possible with CMD methods.

The observation of the structure and dynamics of the liquid/surface interface region of even well terminated surfaces is still extremely difficult. However, recent surface X-ray scattering techniques designed to probe the structure and dynamics in the liquid-surface region have been developed [48, 93]. In this method calculated X-ray scattering intensities are directly compared with the data from X-ray reflectivity (crystal truncation rod diffraction (CTR)). Surface and interface models are constructed and empirical (X-ray) scattering theory and fitting techniques are used to create atomic structure models of the interface that best reproduces the observed scattering intensities. This CTR analysis results in a structural model of the interface region in which atomic positions are optimized to fit the scattering data without bond length constraints. In addition CTR is insensitive to weakly scattering atoms and therefore cannot locate proton positions, which in many cases are essential to the interpretation of the reactive chemistry of the interface. In a recent paper we have evaluated the effectiveness of supporting CTR measurements with high accuracy DFT –molecular dynamics (DFT-MD) calculations. These results support the use of DFT to interpret surface structural calculation. DFT also provides structural information that cannot be resolved by CTR observations either because of weak scattering or surface dynamics occurring on time scales that are not resolved in CTR (<minutes).

Various CTR studies have been reported including layers water structures on hematite (001) [30, 138, 143], Fe(II) ion adsorption on hematite (001) [32, 137, 138], water structures on

hematite (012) [31, 136], Fe(II) adsorption on hematite (012) [32, 137, 138]. These observations provide rich data for the evaluation of theoretical models of surface terminations and associated interface water layers. The (001) and (012) surfaces are the dominant growth surfaces in natural hematite crystals [40]. Results of AIMD simulation for the Hematite/solution interface for these terminations are presented in this section. Extensive CMD calculations for the Hematite (001) and (012) terminations with liquid layers have been presented by Fenter et [48] . These calculations have led to interesting insights. However, the difficulty of selection of a model at the atomic level is a limitation is illustrated by the calculations. AIMD based methods has been used in studying hematite surfaces atomic structure, adsorption (Cr(VI) complex and electronic structure [87, 121, 152, 153, 154]. Most of these calculations have been limited to developing structural models at zero temperature and pressure (PT) in a very limited phase space. In such calculation the optimization only provides one promising structure, which maybe highly dependent on initial structural guess. Ab-initio computational thermodynamics [94] have been reported which consider selected candidates for surface structure. In these calculations an attempt to estimate the free energy is made to provide stability as a functions of TP. However this is still a limited search over the selected structures.

In this section we present, AIMD simulation of structures and reactions (Fe^{2+} absorption) in the hematite–water interfaces region with the intension of interpreting the structure of the reactive interface region, the dynamics of the water and solute molecules and atoms along the reaction coordinate and the electronic structure associated with hydrogen and covalent bond formations. The estimated potentials and interatomic forces are calculated directly from the all electron Schrödinger equation using pseudopotential and DFT+U methods. These methods include an approximate treatment of electron exchange effects (U inclusion) that is important to the analysis of materials containing transition metals while still providing a manageable computational cost. These methods are discussed in Chapter 2. In some cases these calculations are supported by hybrid DFT calculations, which are expected to provide

a more reliable (but much more expensive) level accuracy in the estimation of the effects of electron exchange.

The improved description of unusual and unknown bonding environments strongly supports the use of electronic structure based simulations.The limitation of Ab-initio MD simulation is the execution time per dynamical step in the MD simulation for big systems. But with the development of supercomputers and parallel algorithms for Ab-initio methods, molecule modeling by ab-initio MD is rapidly becoming more tractable. In our calculation, the simulated systems include 300 atoms, 1000 electrons. Four ab-initio MD simulations have been taken, hydrated "oxygen-terminated" hematite –water interfaces for (001) and (012) surfaces (Fig. 3.1) respectively, and also one extra ferrous ion absorbed on those surfaces in aqueous solutions. Structures analysis of water layers on surfaces and ion adsorption on surface is based on trajectories from the four simulations. AIMD simulations of the simple electron transfer reaction

$$Fe^{2+}(\text{hydrated interface solute}) \Rightarrow Fe^{3+}(\text{surface absorbed ion}) + e^{-}(\text{localized or transported}) \tag{3.1}$$

This process has recently been investigated as related hematite mineral growth [**?**]Kerisit and Rosso, 2006; Yanina and Rosso, 2008). We report here simulations of the electronic structures of Fe(II) ion adsorption on hematite surfaces in aqueous solutions.

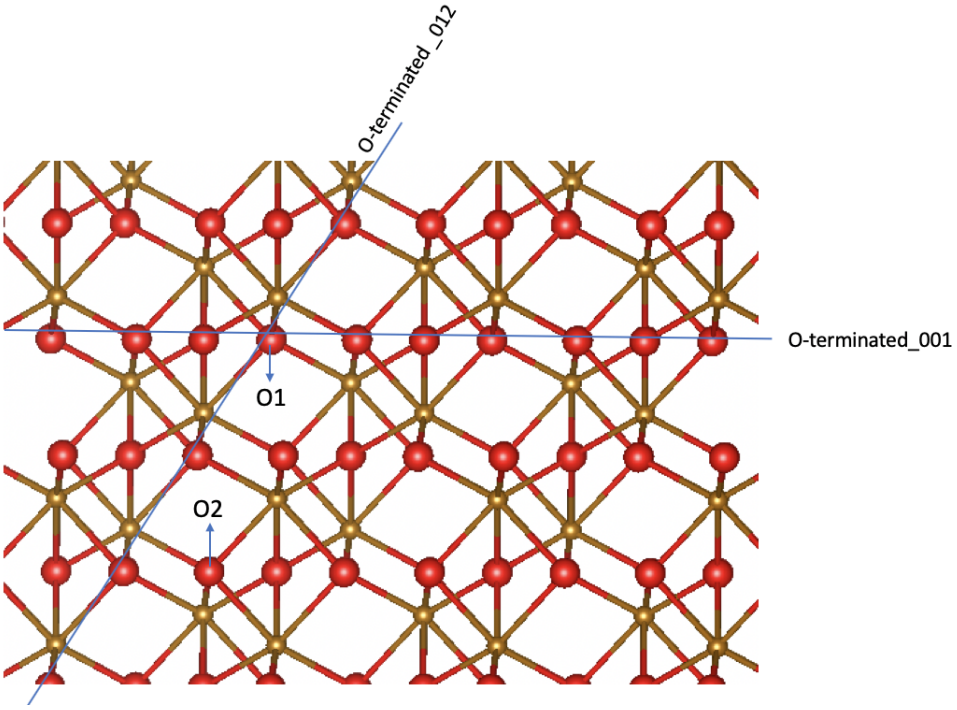


Figure 3.1: Hematite (001) and (012) surfaces terminations used in our work

3.2 Computational Methods and Computational Cells

3.2.1 Computational Methods, Choice of DFT Level and Expansion Basis

The materials investigates here pose a difficult electronic structure problem since their properties are heavily dependent on the properties of the strongly localized d electrons, complex hydration processes, disorder of the surface/solution interface, the interaction of the solution phase with the highly charged mineral surface, etc. Fortunately, the intractable problem of the calculation of the electronic structure for a many particle condensed atomic system is dramatically simplified by the density functional phenomenology [108]. In the most used of these methods, the exchange correlation potential [108] is replaced by a local (LDA) or semilocal approximation (DFT+GGA). However, it is well known that mean field methods such cannot accurately treat the highly correlated behavior of materials containing elements

with highly localized d and f valance electron electrons [55]. These materials include the geochemically important mineral Hematite considered here.

The complexity of the electronic structure description of these materials is a reflection of the large energy cost to doubly occupy a transition element atomic center (large correlation energy). In an effort to better provide more flexible DFT phenomenology that partially reduced known errors of local approximations. The most common of these methods reintroduces "exact exchange" (Hartree Fock exchange) in and ad hoc way and are generally called "hybrid" exchange methods [9]. The computational cost of the hybrid calculations is quite high for condensed matter systems. However, computations have shown (see below) that the electronic structure of transition require DFT methods beyond DFT+GGA. The more fundamental incorporation of such effects in a practical computational scheme is a topic of current condensed matter research.

Given a choice of DFT formalism, a basis set must be chosen to solve the coupled single particle problems. In this work the plane wave pseudopotential method is implemented utilizing the software contained in the NWChem software package [145]. Plane wave calculations using density functional theory (DFT) have been widely used to predict the structure properties the bulk and surface regions of condensed materials. Recent very large bench-mark calculations of surfaces of the 2nd row mineral corrundum (Al_2O_3) using local DFT have shown remarkable agreement with both structural and electronic properties for this class of materials composed of second and third row (s and p valance orbitals). However, it is well known that mean field methods such as DFT should not be expected to accurately treat the highly correlated behavior of the electrons that are characteristic of the d dominated bands of the geochemically important transition metal oxides and oxihydroxides. The computational complexity of these materials is a reflection of the large energy cost to doubly occupy a transition element atomic center (large correlation energy).

Nevertheless, calculations for the structural properties of these minerals have recently

been reported [83, 84] which show that mean field (local) DFT calculations provide a quite accurate description of bulk structure (≈ 2%, PBE96) and the structure of clean (bulk termination) surface models. On the other hand, the agreement of local DFT calculation with electronic structure properties for these strongly correlated systems is far from satisfactory. For example the direct DFT band gap for Hematite is given to be .2ev, whereas the observed value is 2ev. This level of error is typical of local DFT calculations of transition metal oxides and oxyhydroxides. The hybrid functional which combines exact exchange (Hartree Fock exchange) and DFT functional [25] is known to provide improved accuracy in many molecular systems. This functional gives overestimated the bad gap giving 5.8 ev. However, this method is extremely expensive in computation. For the big scale mineral water interface simulation in this work (1000 electrons, 300 atoms), DFT+U [46, 121, 122, 129, 148] includes the correlation effect approximately, also doesn't increase the computation work too much comparing to DFT. For hematite the results of band gap and local magnetic moment from DFT+U calculation are very close to the results from hybrid functional in accuracy. In DFT+U method, the d and f electron correlations are added by calculating Hubbard term approximately. Then a double counting term which describes those correlations in DFT needs to be deduced.

The system was propagated in time using Car-Parrinello Molecular dynamics (CPMD) [29, 99] scheme. In CPMD framework, two terms have been added separately in two motion equations due to the added U term. In this work, U and J are set to be 4 eV and 1 eV [122] respectively which has been widely accepted and proven to be the most appropriate constant values for Fe in hematite. PBE96 (GGA) exchange correlation functional is also employed. A Teter's style norm-conserving pseudopotential [141] with semi core was used to Fe atom in which 3s and 3p are included as core electrons and softened Hamann pseudopotentials [61] were used to oxygen and hydrogen atoms. Plane wave energy cutoff 50 Hartree for the wavefucntion and 100 Hartree for the density were used. Equation of motions in CPMD were integrated using Verlet algorithm, with a time step 0.12 fs and fictitious orbital mass

600.0 au. All hydrogen atoms have been replaced by deuterium to facilitate the integration. The canonical ensemble was chose for this simulation, Nose- Hoover thermostat was used to control the temperature for ions (300 K) and electrons (1200 K). CPMD simulations have been performed 15 ps for each system, 1 ps equilibration was performed after which trajectory has been collected. All the calculations are performed with NWChem package.

3.2.2 Computational Cells Structural Details

The 30-atom hexagonal representation of the hematite unit cell has been studied in previous work. Here we use lattice constant $a = b = 5.04$Å, $c = 13.86$Å. To create surface (001) surface slab, we expand the cell in a and b direction which made a (2×2) surface ($a = b = 10.08$Å). Previous studies have shown the uppermost hematite (001) surface termination is "O-termination". Our "O-termination" (001) surface slab contains 8 Fe layers which can be represented by O3-Fe-Fe-O3-Fe-Fe-O3-Fe-Fe-O3-Fe-Fe-O3 [30]. The hydration of O-termination (001) surface has also been investigated [44]. Each surface oxygen which is doubly bonded to Fe atoms has been hydrated to form a hydroxyl group. These hydrogxyl groups are taken to be located in oxygen vacancies created by the cleavage. We expanded the cell in c direction ($c = 24.27$Å) between two surfaces in the slab, and added 54 water molecules whose density was $1.0 g/cm^3$. The total simulated cell is electrically neutral with 242 atoms which include 32 Fe, 102 Oxygen and 108 H and 976 valance electrons.To create (012) surface slab, we use Euler transformation to get the new cell which has lattice parameters as $a' = 5.006$Å, $b' = 5.448$Å, $c' = 7.399$Å, $\alpha = 83.4°, \beta = \gamma = 90°$. To better simulate the dynamics on the surface, we expand the cell in a' and b' directions which made a 2×2 surface. ($a' = 10.012$Å, $b' = 10.896$Å). Surface diffraction of hematite (012) surface show this surface differs from an ideal stoichiometric termination due to the vacancies of the near surface bulk Fe sites. Ab-initio themodynamics study predicts this type of termination is the most stable. We include 4 Fe layers in our slab, which can be represented by O2-X-O2-Fe2-O2-Fe2-O2-O2-Fe2-O2-

Fe2-O2-X-O2 in c axis. In this surface model, there are two types of surface oxygen, O1 and O2. Similar to Yin's work [153], each surface oxygen has been hydrated which leads a singly bonded hydroxyl (Fe-O-H) and a triply coordinated hydroxyl (O3-H). Between the two surfaces of the slab in the cell, we add 54 water molecules ($c = 25.0$Å), and the density of water is set to $1.0 g/cm^3$. The total simulated cell is electrically neutral with 1104 valance electrons and 290 atoms which include 32 Fe, 118 Oxygen and 140 Hydrogen.

3.2.3 Spin Configurations of Surface Slabs

Hematite is antiferromagenetic in room temperature and pressure, each Fe^{3+} ion in hematite is a high-spin d^5 center which we can be found from experimental local magnetic moment. To investigate the ground magnetic states for the surface slabs we create, different magnetic states were considered and their energies are computed. For (012) surface, the energies for system in three antiferrmagnetic states (AF $+-+-$, AF $++--$, AF $+--+$) and one ferromagnetic state (FM $++++$) have been calculated. AF $+--+$ is found to be most stable state. For (001) surface, four antiferrmagnetic states (AF $++--++--$, AF $++----++$, AF $+--++--+$, AF $+-+-+-+-$) and one ferromagnetic state(FM $++++++++$) are taken into account. AF $++--++--$ is the ground magnetic state. The energies differences are shown in the table 3.1 and the table 3.2. The ground magnetic states for both (001) and (012) surfaces are consistent with magnetic ordering in bulk hematite which shows AF $+--+$ both along [001] and [111] with opposing magnetic moments places on Fe-Fe centers separated by short length. This agreement is expected since bonding conditions and chemical environments for Fe atoms in the surface slab haven't been changed too much comparing to bulk hematite [122].

Table 3.1: Energy difference between different magnetic states configurations for (012) surface

spin configuration	$+--+$	$+-+-$	$++--$	$++++$
ΔE(meV/Fe atom)	0	35.4	37.9	102.2

Table 3.2: Energy difference between different magnetic states configurations for (001) surface

spin configuration	$++--++--$	$++----++$	$+--++--+$	$+-+-+-+-$	$++++++++$
ΔE(meV/Fe atom)	0	90.6	114.0	143.1	336.0

3.3 The (012) Protonation and Water Absorption of Cleaved Surfaces

3.3.1 Hematite (012) Surface Protonation Models

The protonation (termination) of the bonds on the surfaces that become unsaturated on cleavage is an important part of surface chemical environment which can affect both the local electronic structure and the structure of the absorbed water layers structure. In O-O-Fe-O-Fe-O-O-Fe-R cleavage of hematite (012) surface, there are two possible hydrated models which lead to a neutral surface, (OH)-(OH)-Fe-O-Fe-O-O-Fe-R [153] and (OH2)-O-Fe-O-Fe-O-O-R. In both models, there are two types of oxygen sites including singly Fe-coordinated Oxygen and triply Fe-coordinated Oxygen. Triply Fe-coordinated Oxygen (O2) is more into the slab than singly Fe-coordinated Oxygen (O1)which is on the top of surface. (Fig. 3.2(A)) Oxygen atoms are quadruply bonded to Fe atoms in bulk.

Following Ab-initio Thermodynamis approach, to determine the best protonation model, we optimized the structures of these two (2×2) hydrated surface models using DFT+U method. The Hydrated model (OH)-(OH)-Fe-O-Fe-O-O-Fe-R (model 1 in Fig. 3.2(A) and 3.2(B)) is found to be 11.7meV/Å^2 lower in surface energy than the other model. In this hydrated model, O1and O2 are both hydrated forming two OH groups. After structural optimization, O2H group bridges to O1H group forming a hydrogen bond (2.73Å, 154.6°) (Fig. 3.2(A) , H-bond 1) This Hydrogen bond reduces the bond valence of O2 which might be over-saturated. From another aspect, it also contributes bond valence to O1 oxygen considering possible

under-saturation situation of O1 which is only singly Fe-coordinated. Hence, this Hydrogen bond stabilizes the surface configuration effectively.

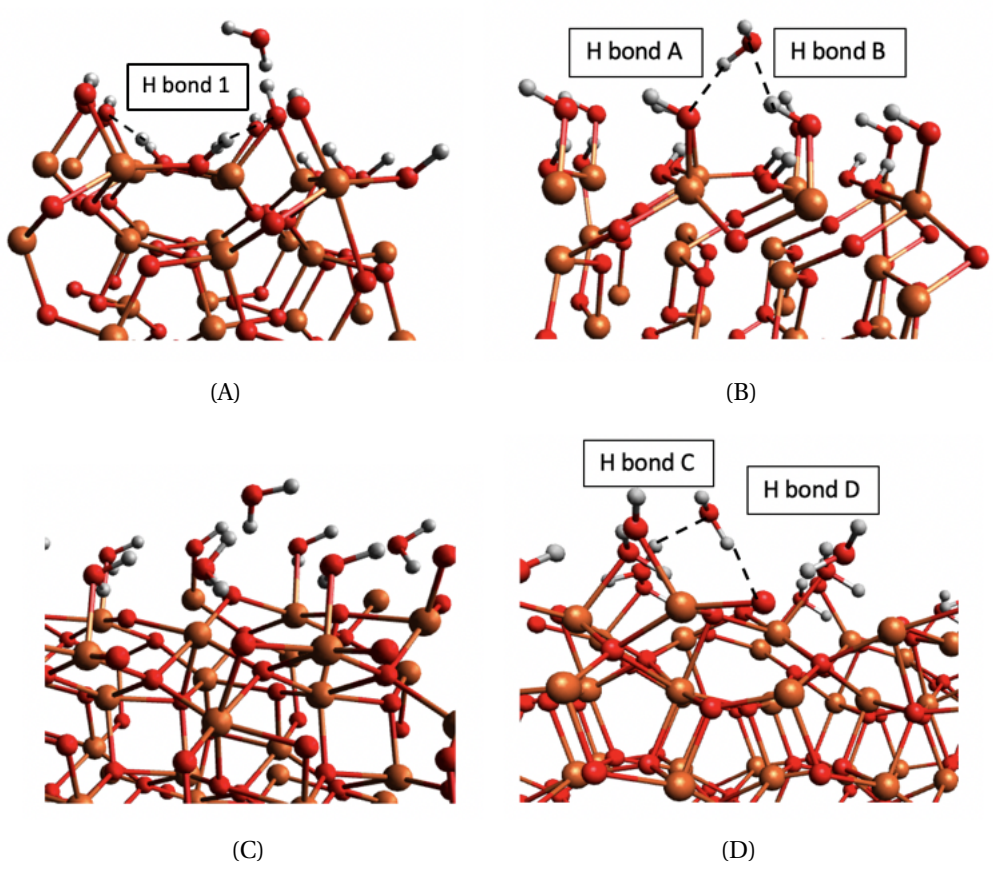


Figure 3.2: Water molecule absorbed on different hydration models for hematite (012) surface. (A) and (B) are side-views of Model 1, (C) and (D) are side-views of Model 2.

3.3.2 Water Absorption on Hematite (012) Cleaved Surface

Caused by cleavage and protonation, atoms on surface region are normally oversaturated or undersaturated. This is an important reason water molecules absorbed on surface. Hydrogen bonds which bridge water molecules to surface layers and Hydrogen bonds between surface atoms can stabilize the surface region. They also play significant roles in determining the water structure on surface. Recently major advances have been made in the observation of water layer structures on the surface region using synchrotron generated X ray diffraction.

Ghose [56] employed crystal truncation rod (CTR) techniques to study three dimensional structural of water layers on goethite (100) surface. Tanwar [136] also used this techniques to investigate water adsorption on hematite (012) surface. These works proposed many structural models which can help us understanding the interfacial structure.

In computational side, single or several water molecules adsorptions process can be investigated by structural optimization tool employing Ab-initio (DFT or DFT+U) methods. Kubicki [83]studied water layers structure on goethite (100) surface. Lo [94] concluded the surface water can stabilize surface structure by hydrogen bonding when studying water adsorption on hematite (012) surface.

As starting point for adsorption optimizations of the interface structure on hematite, we studied the single water adsorption process on the protonated hematite (012) surface by placing one water molecule in contact with the (2×2) surface of the optimized models (model 1 and model 2 respectively in Fig. 3.2). The adsorption energy for one water molecule on both protonated models can be calculated as:

$$E_{\text{adsorption}} = E_{\text{water}} + E_{\text{surface}} - E_{\text{water-surface}} \tag{3.2}$$

The water adsorption energy for model 1 is 6.70 kcal/mol which is slightly greater than the adsorption energy 5.53 kcal/mol for model 2. In model 1, the absorbed water forms a hydrogen bond with an O1 atom as a donor (2.71Å, 160.4°, H-bond A in Fig. 3.2(B)) and a Hydrogen bond with another O1 atom as an acceptor (2.70Å, 168.9°, H-bond B in Fig. 3.2(B)). In model 2, the O2 might be under-saturated. The absorbed water forms a hydrogen bond with an O2 atom as a donor. (2.90Å, 166.0°, H-bond D in Fig. 3.2(C)) It also forms a hydrogen bond with an O1 as an acceptor. (2.75Å, 146.4°, H-bond C Fig. 3.2(C)) The side views of water adsorption, hydrated models and hydrogen bonds are shown in Fig. 3.2.

Combining the result from surface protonation section, for those two hydrated charge neutral surface models, model 1 has been shown better energetically, it also has slightly greater

water adsorption energy when one water molecule absorbed on the (2×2) surface. However, the energy gap between model 1 and model 2 is small, so the co-existence of model 1 and model 2 is possible. In Catalano's experimental work to this surface [31], a closer water layer which is regarded forming hydrogen bonds with (O2) atoms has been observed which agrees more with model 2. In our model 1, (O2H) is oversaturated and forms Hydrogen-bonds with O1 as a donor (Fig. 3.2(A)), it doesn't have any capability to attract extra water molecules. While in Model 2, O2 atoms are undersaturated, and it is possible to attract water molecules which can form a closer water layer.

3.4 Structural Properties of Interface

3.4.1 Hematite (001) Aqueous Interface

In previous experimental studies, hydrated hematite (001) surface contains several different domains. CTR data has been analyzed using different domains models. Tanwar [137] proposed both single domain and double domain models in which double domain models improves in fitting. Several other studies also prove the relative proportion of distinct domains depends on the preparation conditions. However, the uppermost hematite (001) surface is believed to be O-termination domain. Considering the size limit of our simulation cell, we use single O-termination domain in our work. This hydrated O-termination domain has a structure model as O3-Fe-Fe-R. The upper surface OH functional group layer has been doubly bonded to surface Fe atoms. These OH functional groups formed hydrogen bonds with water molecules, (can act both as acceptor and donor) which produced absorbed water layer on the hematite (001) surface. The structure of hematite (001) aqueous interface is shown in Fig. 3.3. The oxygen atoms in the first water layer is labeled as Oi.

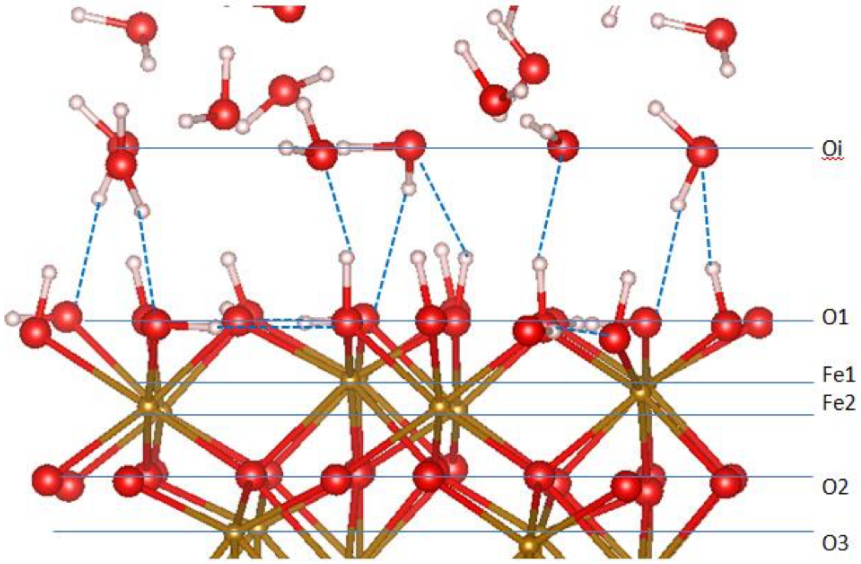


Figure 3.3: Structure of Hematite(001)–water interface

From the X-ray scattering experiments data, the electron density profile has been calculated. Here, from the geometry we generate from CPMD simulation, we also calculate and average the electron density for every frame of the trajectory. Boarding has been applied by using Gaussian distribution in the direction perpendicular to the surface. Each atom type has different Gaussian variance to reflect the atom size. The normal Gaussian distribution has been multiplied by the atomic number. We then compare our electron density profile with experiments.

In the table 3.3, we list out the interlayer spacing from the calculations with the comparison with previous experiments and calculations study. In classical molecular dynamics, results are very sensitive to the choices of models (model 1 and model 2 show difference). Our ab-initio molecular dynamics result is in very good agreement with experiments. Also agreed with the experiments, only one distinct absorbed water layer has been observed in this picture. The occupancy of water defines as the number of water per (1×1) surface. Our calculation shows the occupancy of the water layer is 2.4, this is in the range of experimental result which is 2.7 ± 0.3 and 3.0 ± 1.0. However the height of the first layer water from the surface oxygen in

this work is 2.5Å, this is a little smaller than classical MD results, but have a big difference from the experiments result. Result from Ab-initio MD confirms that this difference is not from the potential used in classical MD. (in Catalano's analysis, this error might caused by the potential used in classical MD simulation).

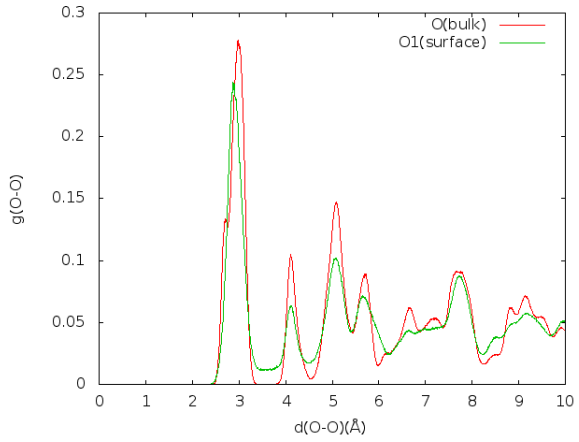
Table 3.3: Interlayer spacing (Å) at the oxygen termination hydrated surface for (001) and (012) surface slabs

001 surface slab	Oi-O1	O1-Fe1	Fe1-Fe2	Fe2-O2	O2-Fe3	Fe3-Fe4	Fe4-O3	O3-Fe5
our work	2.51	0.98	0.34	1.04	0.93	0.58	0.90	0.92
Exp a	N/A	1.04	0.32	0.95	0.86	0.57	0.89	0.84
Exp b	1.96 ± 0.6	1.13	0.50	0.90	0.85	0.47	0.90	0.90
MD model 1	2.7	0.7	0.6	0.9	0.7	0.7	0.8	0.8
MD model 2	2.8	0.9	0.3	1.0	0.9	0.5	0.9	0.9
012 surface slab	Oii-Oi	Oi-O1	Oi'-O1	O1-O2	O2-Fe1	Fe1-O3	O3-Fe2	Fe2-O4
our work	1.74	2.15	N/A	1.53	0.26	0.94	0.98	0.30
Exp a	2.0	2.60	0.9	1.40	0.37	0.93	0.65	0.35

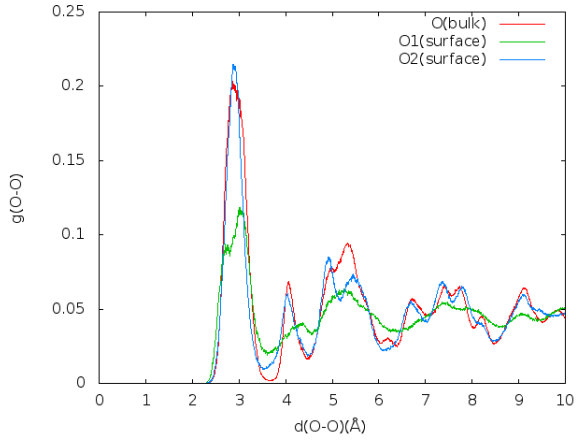
The first layer water absorbed to hydrated surface by forming Hydrogen bond with surface hydroxide group. From picture, hydroxide group can either stand or lay on the surface. The first layer waters can attach with H atoms in standing hydroxide which forms H-bond as acceptor (0.630 per water molecule) or attached with O atoms in lying hydroxide group which forms H-bond as donor (0.352 per water molecule). The absorbed water can also form H-bond with other water molecules including water molecules also in the absorbed layer. Every absorbed water molecule forms 1.722 H-bonds as acceptor which is higher than average bulk water. Lying hydroxides are also H-bonded with standing hydroxides acting as donor. While each surface oxygen atom only forms 0.445 H-bonds as acceptor in total. This number is obviously smaller than oxygen atom in bulk water. The reason is lone pair electrons of surface oxygen can interact with empty d orbital of Fe atoms (half filled for Fe^{3+}). This leads a dramatic decrease of lone pair electrons that can interact with H empty s orbital which forms Hydrogen bond.

The oxygen-oxygen distance is also with great interests. The average H-bond length

between absorbed water layer and surface oxygen is 2.83 which is very close to H-bond length in bulk water. Similar to H-bond length, in Fig. 3.4(A) from O-O Radial distribution function (RDF) in which surface oxygen are set as the center, the first peak occurs at 2.85Å. This O-O separation distance agrees with the H-bond length in bulk water which is typically 2.8Å. [64]. Experiments studies are shown much shorter O-O distance, 2.3Å [**?**]Tanwar 2009) and 1.9Å [**?**]Trainor 2004) which are not physically plausible. The reason might be the incorrect model assumption working with X-ray scattering data.



(A) RDF of O'-O on hematite (001)-water interface (O' shown in legend)



(B) RDF of O'-O on hematite (012)-water interface (O' shown in legend)

Figure 3.4: Radial distribution functions (RDFs) of O'-O for hematite (001) and (012) - water interfaces

3.4.2 Hematite (012) Aqueous Interface

Fig. 3.5 shows the structure of hematite (012) aqueous interface. We found two separate peaks which represents two absorbed layers in the electron density height distribution. Hematite (012) has two layers while (001) only has one layer, this is consistent with Catalano's work. Some clues can be found in H-bond analysis for this difference in the number of water layers absorbed. Comparing to (001), Oi (from first layer water) above (012) surface has stronger ability forming a hydrogen bond with water molecules out of the first absorbed layer, (1.188:1.019 per O atom) especially as acceptor (0.645:0.435 per O atom).

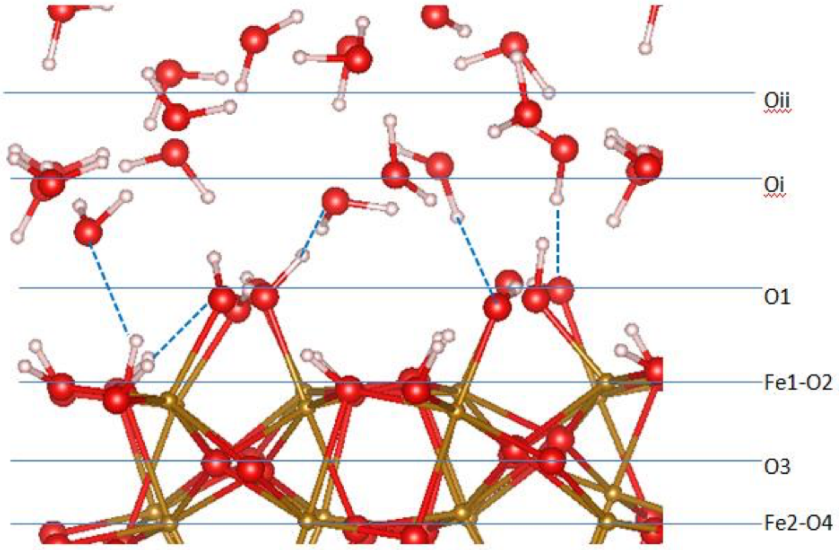
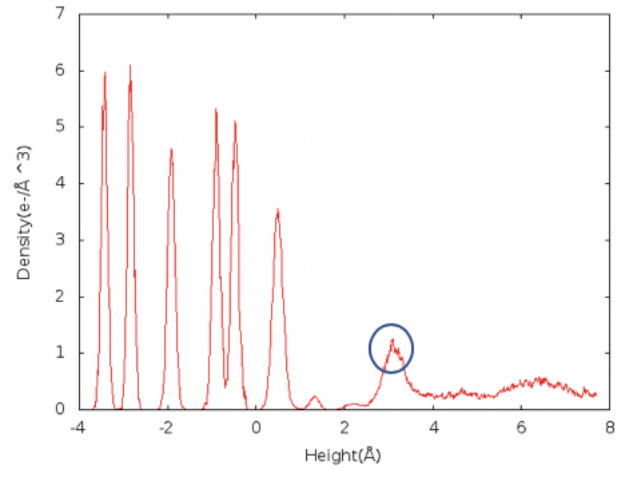
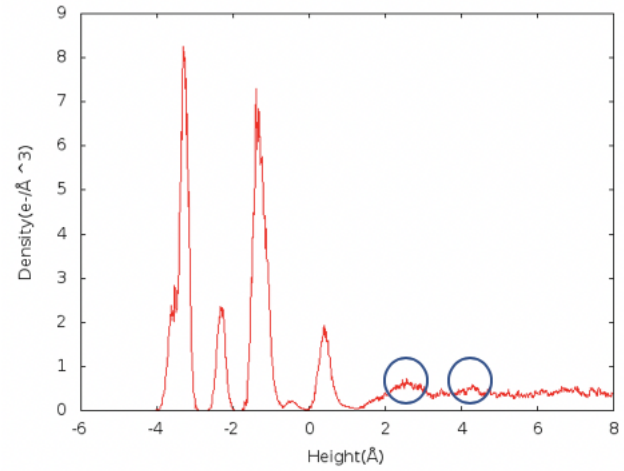


Figure 3.5: Structure of Hematite(012)–water interface



(A) Hematite (001) – water interface



(B) Hematite (012) – water interface

Figure 3.6: Electron density profiles for hematite-water interfaces

There are two types of surface oxygen O1 and O2. Our H-bond analysis shows there are H-bonding between O1 and O2 in which O2 acts as donor. Our simulation shows O2 has little ability forming H-bond with water as donor (0.026 per O2 atom), also it can't form any H-bond with water molecules as acceptor. The possible reason is O2 atom is triply bonded to surface iron atoms, the lone pair electrons from O2 all interacts with empty Fe d orbital, so O2 can't H-bonded to any water molecule as acceptor. This is inconsistent with recent study by Catalano [31]. Our simulations are for perfect O-terminated hydrated (012) surface, in the

real system, if that O2 is dehydrated or less bonded to Fe atoms, it is possible that it can attract water molecule forming H-bonds. Similar to hydroxide group on (001) surface, hydroxide group containing O1 can stand or lay on the surface. They form H-bonds with first layer water and also other hydroxide groups. Due to singly Fe-bonded, oxygen is far from saturated, it forms 1.609 H-bonds as acceptor.

Seen from table 3.4, the hydrogen bonds between hydroxyl groups on the 012 surface (O1-H—O1) are strong bonds whose average bond length is 2.70Å. Contrastively, O1-H—O1 hydrogen bonds on (001) surface are obvious weaker than Hydrogen bonds in bulk water whose average bond length is 2.90Å. This again can be illustrated by the difference of the saturation of the oxygen atoms on two surfaces in our hydrated models.

Table 3.4: Surface hydrogen bonds statistics on hematite (001) and (012) aqueous interfaces (Bond length: Å, Degree: ∘

001 interface	ave. bond length	var. bond length	most prob. bond length	ave. degree	var. degree	most prob. degree	No. of H-bonds per O1/O2 atom	No. of H-Bonds per Oi atom
O1-H—Oi	2.85	0.18	2.79	157.0	10.9	161.0	0.422	0.630
Oi-H—O1	2.81	0.17	2.79	157.0	11.0	163.5	0.236	0.352
O1-H—O1	2.90	0.14	2.83	147.1	9.0	138.6	0.209	N/A
Oi-H—Oi	2.81	0.17	2.82	157.1	10.8	161.5	N/A	0.657
Oi-H—Oii	2.81	0.17	2.80	157.5	10.8	161.1	N/A	0.584
Oii-H—Oi	2.81	0.18	2.79	156.8	11.1	160.0	N/A	0.435
012 interface								
O1-H—Oi	2.84	0.18	2.75	158.0	10.9	163.9	0.317	0.321
Oi-H—O1	2.81	0.17	2.71	159.0	10.4	162.6	0.472	0.477
O2-H—Oi	2.96	0.16	3.14	151.7	11.3	135.2	0.026	0.026
Oi-H—O2	N/A	N/A	N/A	N/A	N/A	N/A	0.0	0.0
O1-H—O1	2.70	0.15	2.65	154.4	10.3	155.3	0.473	N/A
O2-H—O1	2.80	0.19	2.76	152.3	9.14	150.8	0.664	N/A
Oi-H—Oi	2.83	0.17	2.78	157.6	10.9	165.5	N/A	0.456
Oi-H—Oii	2.83	0.16	2.74	158.1	10.7	164.0	N/A	0.543
Oii-H—Oi	2.83	0.18	2.79	159.2	10.8	167.0	N/A	0.645
bulk water								
N/A	2.83	0.16	N/A	160.6	9.42	N/A	N/A	N/A

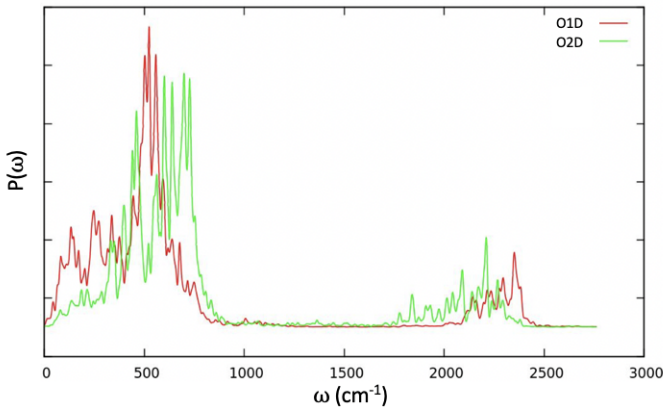
Power spectrum has also been employed to study the properties of surface water and

OH group in hematite (012)-water interface region. Power spectrum could be calculated by taking fourier transform of the velocity autocorrelation functions. [**?**, 78, 142]

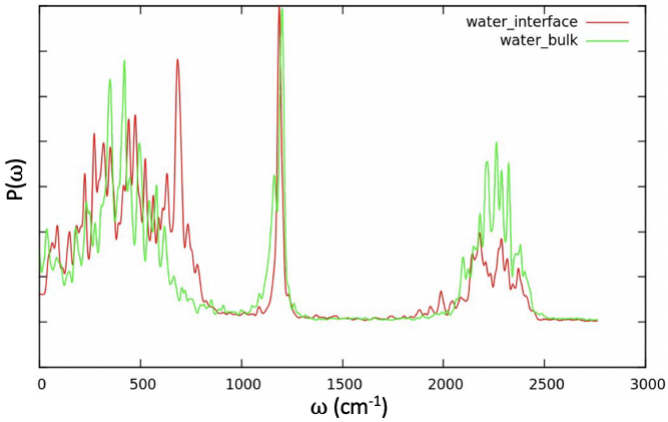
$$P(\omega) = m \int < \dot{r}(\tau)\dot{r}(t+\tau) >_{\tau} e^{-i\omega t} dt \tag{3.3}$$

$< \dot{r}(\tau)\dot{r}(t+\tau) >$ denotes the velocity autocorrelation of the velocity $\dot{r}$. Hydrogen atoms postions from those OD groups (all hydrogen atoms have been replaced by deuterium) and water molecules in the trajectory of hematite(012)-water interface are used to calculate power spectrum. The results are shown in Fig. 3.7(A) and 3.7(B).

The peaks located in the range from 0-800 (cm^{-1}) for both Fig. 3.7(A) and Fig. 3.7(B) are corresopnding to the intermolcular librational and translational motion which are hard to interpert. In Fig 3.7(B), there are peaks around 1185 (cm^{-1}) which are not shown in Fig 3.7(A). That peak is due to the bending motion of water molecules, so that's not observed in OD groups spectrum. The value 1185 (cm^{-1}) agrees with the experimental value 1209 (cm^{-1}) in liquid water. The peaks in the range from 1800-2500 (cm^{-1}) are the contribution of OD streching motion modes. In Fig. 3.7(A), O1D has a blueshift comparing to O2D, this shows O2D forms a relatively stronger hydrogen bond with O1 while O1D likely has a weakening or sometimes no Hydrogen bonds in the interfacial region. In Fig 3.7(B), in higher frequency region, there is one peak 2180 (cm^{-1}) which is closer to experimental bulk ice frequency 2190 (cm^{-1}) and another peak 2287 (cm^{-1}) which is closer to experimental bulk liquid frequency 2260 (cm^{-1}) This indicates water molecules in interfacial region have both liquid-like water and ice-like vibrational properties.



(A) O1D and O2D groups on surface



(B) Water molecules on interfacial region and bulk region

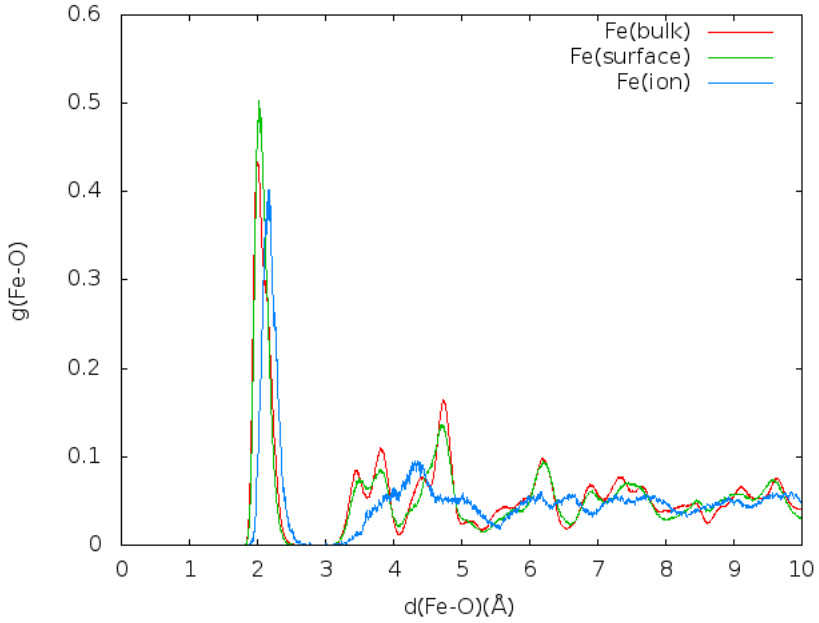
Figure 3.7: Computed power spectrum of two types of OD groups on hematite (012) surface, water on interfacial region and bulk region

3.4.3 Fe(II) Absorption on Hematite (001) Aqueous Interface

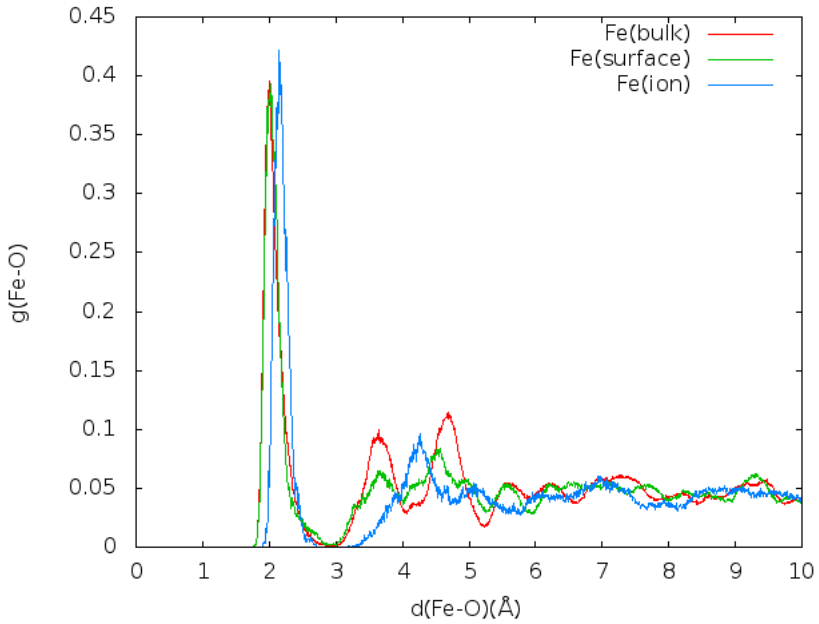
Fe ion is put randomly in the aqueous near surface at the beginning of our simulation. After equilibrium, Fe ion absorbed on the (001) surface becomes six-coordinated. It is triply bonded to the surface hydroxyl groups and also bonded to three water molecules. The absorbed Fe ion corresponds to Fe site in crystal while the Oxygen atoms of three bonded water molecules take the O sites in crystal. Proton transfer on the surface has been observed in the adsorption process. One of the hydroxyl bonded to the absorbed Fe ion loses its proton

which has been attracted by another hydroxyl group that is not bonded to the absorbed Fe ion. This dehydration is an indication of the crystal growth which happens on (001) surface. The absorbed Fe ion can saturate the surface hydroxyl group which promotes the dehydration of the hydroxyl group. The surface oxygen atoms have been doubly bonded to the Fe layers below in c direction, if absorbed Fe layer is full, each surface oxygen atoms will form two Fe-O bonds with the Fe ions in absorbed layer. (Only one absorbed ion in the simulation, so only one Fe-O bond is formed.) Our simulation agrees with the model "Fe adsorption on the O-layer termination" proposed by [138].

The differences between different Iron states are shown in Iron-Oxygen RDF (Fig. 3.8(A)). Fe ion which absorbed on the oxygen-terminated hematite (001) surface has a Fe-O bond length 2.17Å, this is in good agreement to Fe(II)-O bond length in experiments (2.14Å - 2.18Å needed to find the references), while Fe atom on surface and Fe atom inside the slab have Fe-O bond length 2.02Å and 2.00Å respectively, which agrees with average bond length in bulk hematite 2.03Å [11, 100]. This structure difference confirms that in our simulation time scale, the absorbed Fe ion is Fe(II). In the density of states analysis later, we can clearly see that in this study, the absorbed Fe ion keeps Fe(II) an oxidation state in our simulation.



(A) RDF of Fe-O on hematite (001)-water interface



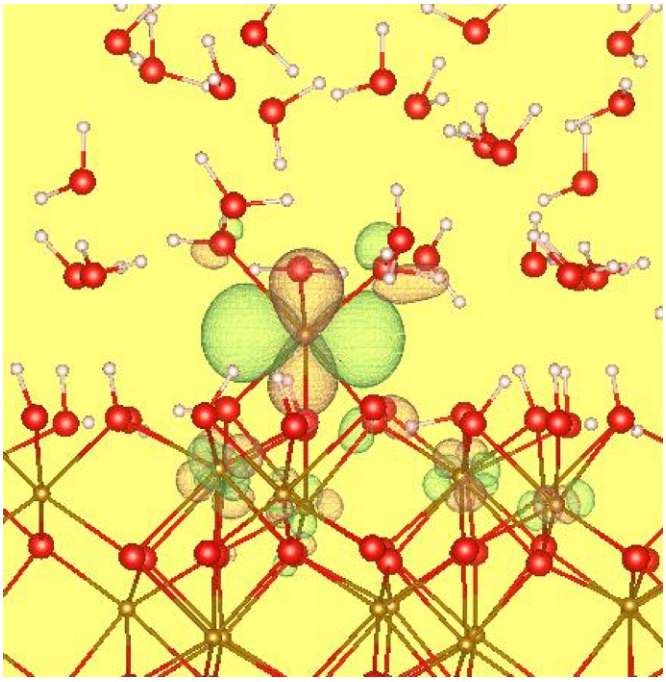
(B) RDF of Fe-O on hematite (012)-water interface

Figure 3.8: Radial distribution functions (RDFs) of Fe-O for hematite (001) and (012) - water interfaces

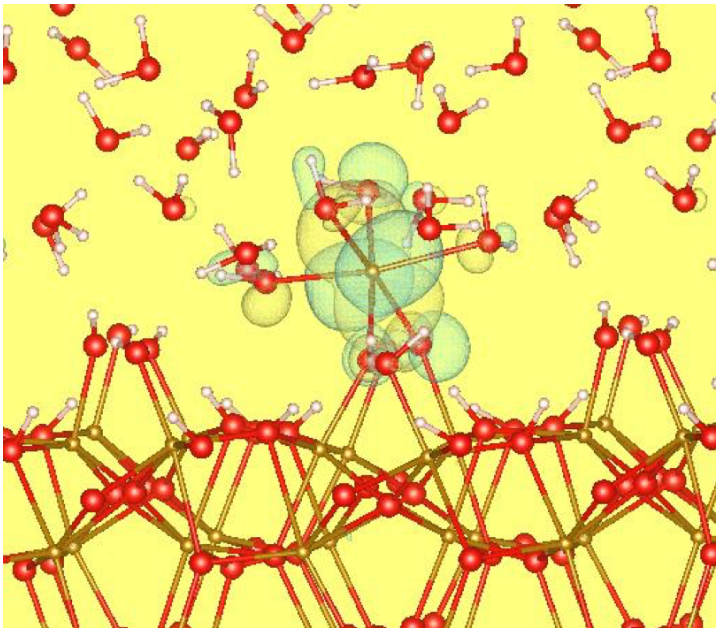
3.4.4 Fe(II) Absorption on Hematite (012) Aqueous Interface

After randomly put the Fe(II) ion near (012) surface, Fe(II) doubly bonded to O1 atom on surface after equilibrium. Since O2 atoms are saturated by three Fe-O bonds and H atom, at the starting stage of the adsorption, Fe ions bond to O1 atoms on surface. Absorbed Fe ion is six-coordinated including two bonds with hydroxyl group on surface and four bonds with water. This differs from (001) surface adsorption in which Fe ion has three bonds with surface oxygen atom. Shown in the Fig. 3.9(B), the O1 atom distribution is sparse on (012) surface while surface Oxygen atoms are more dense on (001) surface. On (012) surface, O1 has two nearest O1 neighbors, the distances are around 3.0Å. O1 atom and its two nearest neighbors are nearly in a line. Geometrically, Fe ion can't form three bonds with O1 atoms without extensive relaxation on surface. Contrastively, on (001) surface, surface oxygen atom O1 has 6 nearest O1 neighbors with a distance near 3.0Å while those six oxygen atoms form hexagon centered in O1. In this O1 distribution, it is possible for Fe ion absorbed three O1 atoms in a triangle.

Similar to adsorption on (001) surface, average Fe-O average bond length on (012) surface is 2.19Å while Fe atom on surface and Fe atom inside the slab have Fe-O bond length 2.01Å and 1.99Å respectively. In our simulation time scale, the absorbed Fe ion is still Fe(II) while other Fe atoms are all Fe (III).



(A) 001 surface



(B) 012 surface

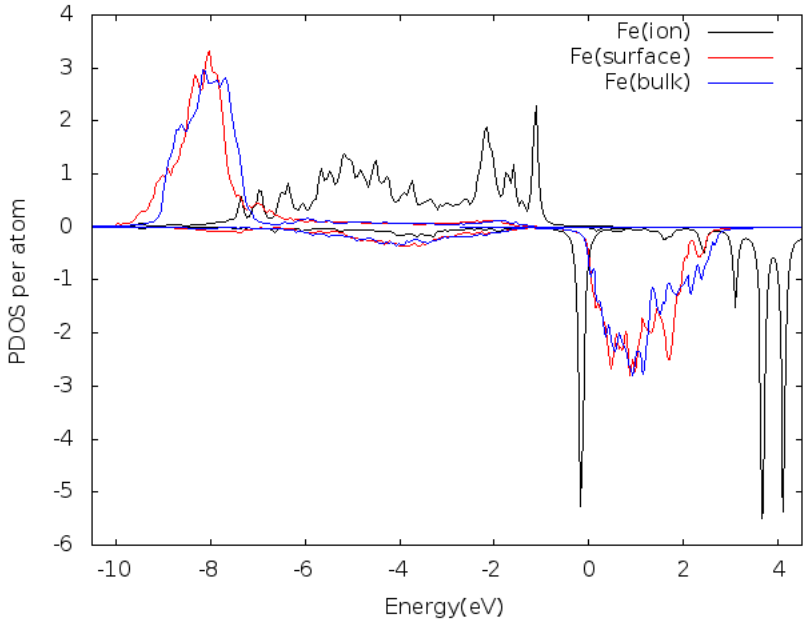
Figure 3.9: HOMOs of Fe(II) ions absorbed on hematite (001) and (012) surfaces in aqueous interfaces

3.5 Electronic Structural Properties of Ion Absorption in Interface

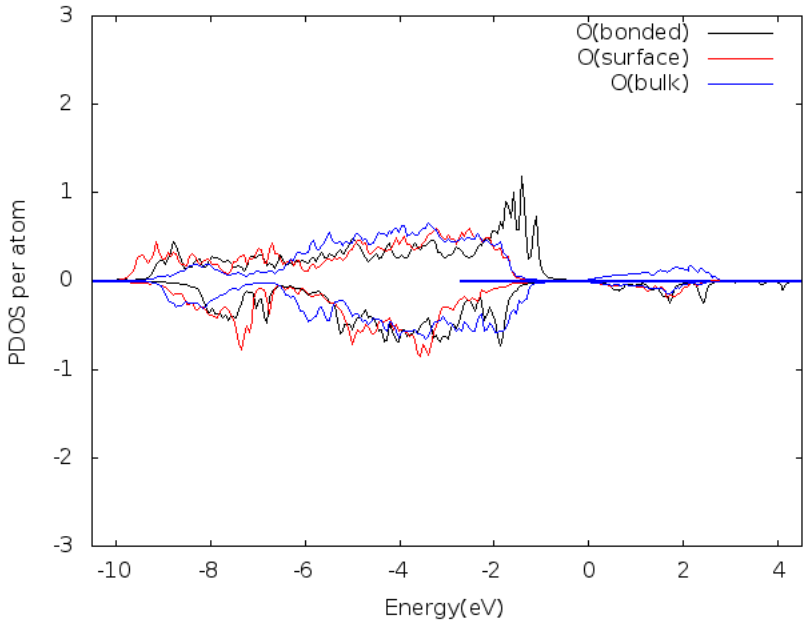
3.5.1 Projected Density of States Analysis

Our simulations show that when Fe^{2+} ion absorbed on hematite (001) and hematite (012) surface, the extra electron will adhere to the ion. It has been clearly shown in the HOMOs pictures (Fig. 3.9) of the system. The shape of HOMO indicates the HOMO is mainly t2g electron on the Fe ion. In the Fe ion projected dos pictures (black lines in Fig. 3.10(A)), the spin down curve has an occupied steep peak. This is the contribution of the extra electron (we set the ion net spin up, so this extra electron has to be spin down). Surface iron and bulk iron have very similar pdos curves since they are both Fe(III) and their bonding conditions are nearly same in the hydrated oxygen terminated hematite surface.

Interestingly, Fe(II) and Fe(III) show very different pdos properties in DFT+U framework. In high spin Fe(III) (bulk Fe and surface Fe), d bands in majority spin have been filled and bands in minority spin are unfilled. By using DFT+U model in the simulation, the spin up and spin down bands have been separated by energy because of the added U term. Bands in majority spin have been moved down and bands in minority spin have been moved up. As a result, DFT+U method predicts a greater band gap than DFT method which agrees better with experiments for Iron oxide materials containing Fe(III). Comparing to Fe(III), the t2g of majority spin of absorbed Fe(II) has been shifted right by a wide margin. The reason is the existence of the t2g electron in minority spin which introduces the column repulsion between spin up and spin down d electrons on the same site. As a result, O-p and Fe-d bands have more overlaps which would lead a more intensive Fe d-Op hybridization.



(A) PDOS on different Fe atoms in the system

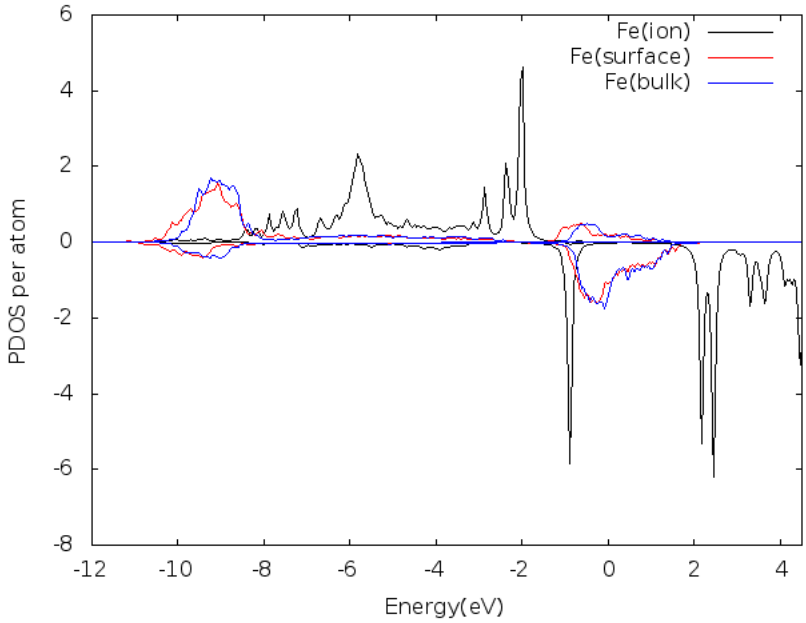


(B) PDOS on different O atoms in the system

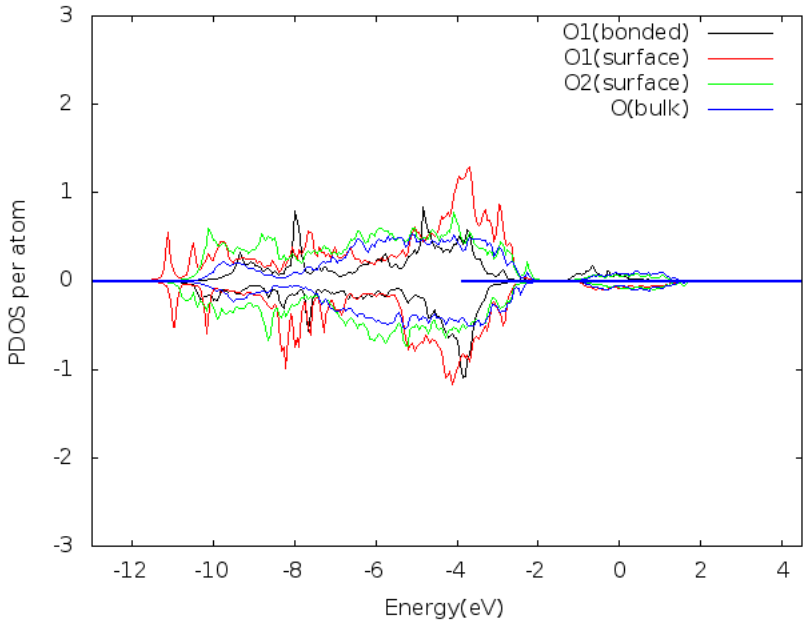
Figure 3.10: Projected density of states of different atoms in the system which has Fe(II) ion absorbed on hematite (001) in its aqueous interface (Fermi level: 0 eV)

Sometimes, terminations of the crystal change the chemical environments for surface

atoms. This can be displayed in the pdos distribution. Surface oxygen atoms on (001) (Fig. 3.10(B)) surfaces is analogical to bulk oxygen atom in the pdos distribution. Type 2 (O2) surface oxygen atoms on (012) (Fig. 3.11(B)) surface are similar to bulk oxygen, while type1 (O1) atoms differ from bulk oxygen atoms for they have more electron states at the top of conduction bands. This may indicate O1 atoms have more free lone pair electrons which mean they have stronger abilities interacting with H ion near surface to form H-bond as acceptors. Our H-bond analysis confirms this conclusion, as acceptor, each O1 atom forms 1.609 H-bonds which is much more than O2 atom (0.0) as well as oxygen atom (0.445) on (001) surface.



(A) PDOS on different Fe atoms in the system



(B) PDOS on different O atoms in the system

Figure 3.11: Projected density of states of different atoms in the system which has Fe(II) ion absorbed on hematite (012) in its aqueous interface (Fermi level: 0 eV)

3.5.2 The Mechanism of Electron Transfer

The mechanism of electron transfer from absorbed Fe(II) to hematite bulk is of great interest. The injected electron have three possibilities, first, it can be trapped in Fe(II)defects near the surface. Second, it migrates to the bulk. Third, it will result in reduction of Fe(III)to Fe(II) at the edge. In our ab-initio Molecular Dynamics, the simulated system is without any defect, and the real electron transfer process would take much longer time than our simulation time scale 10 ps. So our simulation may only show the initial stage of the electron transfer. In our simulation, the extra electron mostly localized on the Iron ion absorbed. But we can still find difference between absorptions happen in (001)and (012)surfaces. In the (001) HOMOs picture (Fig. 3.9), it clearly show there are some fractions of the HOMO electron density migrate to the structural Fe(III), while in (012) surface HOMO, no structural Fe atoms have any electron density of the extra electron. In density of states picture, we found in (001) surface, the energy difference between peak in minority spin of absorbed Fe ion (represented the extra electron) and the top of surface oxygen bands is around 0.5 eV, while for (012) surface, this difference is near 1.5 eV. This will result in (001) surface, the localized orbital for the extra electron would interact more with the surface oxygen bands comparing to (012) surface. This difference implies it's easier for extra electron injection happens in (001) surface comparing to (012) surface. This is consistent with the recent study which shows electron injection occur on (001) surface while dissolutions of Fe(III) happen on (012).

Chapter 3, in full, is a reprint of the material "Interface Structure, Dynamics and Reactivity at the Hematite Solution/Interface: H-Bond Formation and Charge Transfer (with Fe^{2+} Solutes)" by Duo Song, Ying Chen, Eric Bylaska and John Weare, in preparation. The dissertation author is the primary investigator and author.

Chapter 4

Symmetry Breaking in Density Functional Theory due to Dirac Exchange for a Hydrogen Molecule

4.1 Introduction

In this section, we report studies of the properties of density functional theory (DFT) energy minimizers within the context of the hydrogen molecule, (H_2). The (DFT) minimizers discussed are related to those of the Kohn-Sham spin density functional method. The exchange correlation function [108] is simplified by including only Dirac spin density exchange without correlation [108] . We will show that for fixed electron mass, the structure of the minimizing Kohn-Sham solutions change character with the variation of a parameter related to the relative strength of the exchange-correlation component of the functional. Similar studies varying the molecular bond length were undertaken using robust finite element methods for Hartree-Fock and SLDA functionals in [70] and for Hartree-Fock using a maximum overlap method in [6]. The better understanding of such problems is connected to challenges for further

developing density functional theory (see e.g., [38, 39]) and directly in the application of density functional theory (DFT) to highly correlated condensed materials [43] [122] [109] and in spin ordered molecular systems. In addition, uniqueness and symmetry breaking in other quantum mechanical models have recently been studied widely in for instance the works [52, 53] for polaron models, [59] for Hartree-Fock models of atoms, and many others. A similar strategy to that undertaken here in one of our limits was explored for the periodic Thomas–Fermi–Dirac–von Weizsäcker model in [116, 117].

We consider a neutral hydrogen molecule (H_2) with nuclei placed $2R$ apart. The external potential is given by (after a possible coordinate change)

$$V_R(x) = -\frac{1}{\left|x_i - Re_1\right|} - \frac{1}{\left|x_i + Re_1\right|}, \tag{4.1}$$

where e_1 is the $(1,0,0)$ vector in $\mathbb{R}^3$ and x_1 and x_2 denote the positions of the two electrons and we use atomic units. The two-electron Schrödinger operator is given by

$$H_2 = -\frac{1}{2}\Delta_{x_1} - \frac{1}{2}\Delta_{x_2} + V_R(x_1) + V_R(x_2) + \frac{1}{\left|x_1 - x_2\right|}. \tag{4.2}$$

In this work, we will consider the spin-polarized density functional theory with the exchange energy taken to be Dirac exchange and without correlation energy. In the literature, the spin free version of this model is sometimes referred as the XLDA model. We are interested in the spin paired ground state of the system with spin up ψ_+ and spin down ψ_- spatial wave functions. We would like to study the impact of the exchange term on the electronic structure. Therefore, we introduce a strength parameter α for the exchange-correlation energy. The DFT

energy functional is hence given by

$$\mathscr{E}_\alpha(\psi_+,\psi_-) = \frac{1}{2}\int \left|\nabla\psi_+\right|^2 \mathrm{d}x + \frac{1}{2}\int \left|\nabla\psi_-\right|^2 \mathrm{d}x + \int V_R(x)\rho(x)\,\mathrm{d}x \\ + \frac{1}{2}\iint \frac{\rho(x)\rho(y)}{\left|x-y\right|}\,\mathrm{d}x\,\mathrm{d}y - \alpha\int \left(\left|\psi_+\right|^{8/3} + \left|\psi_-\right|^{8/3}\right)\mathrm{d}x, \quad (4.3)$$

where the electron density of the system is given by

$$\rho(x) = \left|\psi_+(x)\right|^2 + \left|\psi_-(x)\right|^2. \quad (4.4)$$

Note in particular in (4.3) the Dirac exchange term is spin-polarized: let $\rho_\pm = \left|\psi_\pm\right|^2$, the exchange term is given by

$$-\alpha\int \left(\rho_+^{4/3} + \rho_-^{4/3}\right)\mathrm{d}x \quad (4.5)$$

as exchange effect originated from Pauli's exclusion principle only occurs between electrons with same spin polarization.[108] [105]

The H_2 molecule has reflection symmetry. We are interested in the symmetry (delocalization) (or lack of symmetry, localization) of ψ_+ and ψ_-. We call the minimizer with the symmetry constraint, $\psi_+ = \psi_- = \psi_R$, a restricted minimizer to the energy functional, denoted as ψ_R. Thus

$$\begin{aligned} \psi_R &= \arg\min \mathscr{E}_\alpha(\psi,\psi) \\ \text{s.t.} \quad &\int \left|\psi\right|^2 = 1. \end{aligned} \quad (4.6)$$

The unrestricted minimization on the other hand considers all possible ψ_+ and ψ_- with the normalization constraints. To distinguish, we denote the minimizers as $\psi_\pm$.

$$\begin{aligned} (\psi_+,\psi_-) &= \arg\min E_\alpha(\psi_+,\psi_-) \\ \text{s.t.} \quad &\int \left|\psi_+\right|^2 = \int \left|\psi_-\right|^2 = 1. \end{aligned} \quad (4.7)$$

Our goal in this work is to understand the symmetry breaking, i.e., the question whether $\psi_+ = \psi_- = \psi_R$. The following result gives the existence of minimizers to both (4.6) and (4.7).

Proposition 4.1.1. *For all $\alpha \geq 0$, there exist solutions $(\phi_+, \phi_-) \in H^1 \times H^1$ with $\int |\phi_\pm|^2 \, \mathrm{d}x = 1$ such that*

$$\mathcal{E}_\alpha(\phi_+, \phi_-) = \min_{\psi_\pm \in H^1; \int |\psi_\pm|^2 dx = 1} \mathcal{E}_\alpha(\psi_+, \psi_-).$$

For a proof of this proposition, we refer the reader to the Concentration Compactness tools employed in [3, Theorem 1] or specifically for LDA models the recent work of [58], where a general existence theory is addressed for LDA models of this type with neutral or positive charge.

For the energy functional (4.3), we have two parameters R and α in the functional. We expect the following behavior of the minimizers for different ranges of parameters:

1. For $\alpha = 0$ and any $R > 0$, the minimizer have the symmetry $\psi_+ = \psi_- = \psi_R$.

2. Fix $R \geq 0$, when we increase α from 0: The minimizer is initially symmetric (hence it is continuous at $\alpha = 0$), the symmetry is broken for larger α ($\psi_+ \neq \psi_-$). The critical parameter α for the transition from symmetric to asymmetric minimizer depends on R.

3. Fix $\alpha > 0$, for R sufficiently large, the minimizer is asymmetric.

Therefore, this suggests a two-dimensional phase diagram where the axes are R and α with a phase transition from symmetric to asymmetric minimizers. In the current manuscript, we will fix R and vary the parameter α in our analysis. However, we will demonstrate the (α, R) phase diagram numerically. Some technical difficulties arise in the the analysis when varying R, which we comment on in Section 4.5 and plan to address in future work. We make our statements precise in the following theorems.

Theorem 1. *Fix $R > 0$, denote ψ_R the minimizer of (4.6) and $\psi_\pm$ the minimizer of (4.7), we have $\psi_\pm = \psi_R$ for $\alpha \ll 1$, and $\psi_+ \neq \psi_-$ for $\alpha \gg 1$.*

In other words, as we increase α, the symmetry $\psi_+ = \psi_-$ is broken. In fact, we can give a more precise characterization of the minimizer $\psi_\pm$ as $\alpha \to \infty$.

Theorem 2. *Fix $R > 0$, as $\alpha \to \infty$, the rescaled and translated minimizer of* (4.7)

$$\alpha^{-\frac{3}{2}} \psi_\pm(\alpha^{-1}(x \mp Re_1))$$

converges to ϕ in H^1, where ϕ is the unique positive, radial solution to the equation

$$-\frac{1}{2}\Delta\phi - \frac{4}{3}|\phi|^{\frac{2}{3}}\phi + E\phi = 0, \text{ with } \int |\phi|^2 dx = 1. \tag{4.8}$$

This can also be seen as the constrained minimizer of the Lagrangian

$$\mathscr{E}_s(\phi) = \frac{1}{2}\int \left|\nabla\phi\right|^2 \mathrm{d}x - \int \left|\phi\right|^{8/3} \mathrm{d}x, \tag{4.9}$$

with mass $\int \left|\phi\right|^2 \mathrm{d}x = 1$. In other words, as $\alpha \to \infty$, each electron becomes concentrated over a different nucleus.

Our results in the small α setting rely heavily on the results of Lieb, Lions and others relating to the concentration compactness phenomenon for constructing minimizers of constrained Lagrangians at $\alpha = 0$, then an application of the Implicit Function Theorem for α small. Our result for large α on the other hand follows from essentially comparing the variational problem to a scale-invariant semi-linear problem, which in turn relies strongly on the orbital stability of solitons for the unperturbed Dirac nonlinearity in 3 dimensions, $|u|^{\frac{2}{3}}u$.

The proof for the small α regime is presented in Section 4.2, while the large α regime is treated in Section 4.3. We present the analysis in detail for fixed $R > 0$ and varying α throughout the proof. Without of loss of generality, for our analysis we will assume $R = 1$ and denote $V = V_R$. Detailed numerical studies of the (α, R) phase diagram and in particular the transition between small and large α for fixed R are discussed in Section 4.4. Concluding

remarks and a discussion of the analysis in case of varying R is included in Section 4.5. The numerical methods are presented in Appendix **??** using a finite element package developed by the group of the first author and developed in the thesis of the second author to study variational problems in electronic structure.

4.2 Proof in the Small α Regime

4.2.1 The Restricted Hartree Model: Case $\alpha = 0$

When $\alpha = 0$, the energy functional we consider becomes

$$\mathscr{E}_0(\psi_+, \psi_-) = \frac{1}{2}\int \left|\nabla\psi_+\right|^2 \mathrm{d}x + \frac{1}{2}\int \left|\nabla\psi_-\right|^2 \mathrm{d}x + \int V(x)\rho(x)\,\mathrm{d}x + \frac{1}{2}\iint \frac{\rho(x)\rho(y)}{\left|x-y\right|}\,\mathrm{d}x\,\mathrm{d}y. \quad (4.10)$$

Without the exchange-correlation energy, the minimizer is always symmetric. Indeed, fixing any density ρ with $\int \rho = 2$, we have

$$\mathscr{E}_{\mathrm{LDA},0}(\sqrt{\rho}/\sqrt{2}, \sqrt{\rho}/\sqrt{2}) = \inf\{E_{\mathrm{LDA},0}(\psi_+, \psi_-) \mid \left|\psi_+\right|^2 + \left|\psi_-\right|^2 = \rho\}. \quad (4.11)$$

Define $\rho_+ = \left|\psi_+\right|^2$ and $\rho_- = \left|\psi_-\right|^2$, the above follows from the convexity

$$2\int \left|\nabla\sqrt{(\rho_+ + \rho_-)/2}\right|^2 \mathrm{d}x \le \int \left|\nabla\sqrt{\rho_+}\right|^2 \mathrm{d}x + \int \left|\nabla\sqrt{\rho_-}\right|^2 \mathrm{d}x, \quad (4.12)$$

and the equality holds if and only if $\rho_+ = \rho_-$ (see [89, Page 177, Theorem 7.8]). Thus, we may denote the common orbital function as $\phi = \psi_+ = \psi_-$, which minimizes the functional

$$\mathscr{E}_0(\phi) = \int \left|\nabla\phi\right|^2 \mathrm{d}x + 2\int V(x)\left|\phi\right|^2 \mathrm{d}x + 2\iint \frac{\left|\phi(x)\right|^2\left|\phi(y)\right|^2}{\left|x-y\right|}\,\mathrm{d}x\,\mathrm{d}y. \quad (4.13)$$

Note that this functional has the same form as the restricted Hartree model treated in [92,

Theorem II.2], which guarantees the existence of a minimizer. Moreover, the minimizer is non-negative without loss of generality and satisfies the Euler-Lagrange equation

$$-\frac{1}{2}\Delta\phi + E_0\phi + V\phi + 2\left(v_c * |\phi|^2\right)\phi = 0 \tag{4.14}$$

where $v_c(x) = |x|^{-1}$ denotes the Coulomb kernel and $E_0 \geq 0$ is the Lagrangian multiplier. We now show that E_0 must be strictly positive. Suppose $E_0 = 0$, define $W := V + 2v_c * |\phi|^2$, we have

$$-\frac{1}{2}\Delta\phi + W\phi = 0. \tag{4.15}$$

Using Newton's theorem, the spherical average of W, denoted by $\overline{W}$ is non-positive outside the ball B_R (since the ball contains all the nuclei charge). Thus, we get trivially that the positive part of $\overline{W}_+ = \max\{\overline{W}, 0\} \in L^{3/2}(B_R^c)$. This implies that $\phi \notin L^2(B_R^c)$ by [88, Lemma 7.18], which is clearly a contradiction, since $\int |\phi|^2 = 1$. Therefore, $E_0 > 0$. This implies that the nuclear potential is properly binding in a similar sense to that explored in [126].

For a purpose that will be clear later, we also consider the variational problem (4.13) with more general mass constraints and denote the minimum as I_M:

$$\begin{aligned} I_M &:= \inf\left\{\mathscr{E}_0(\phi) \mid \int |\phi|^2 = M/2\right\} \\ &= \inf\left\{\mathscr{E}_0(\phi) \mid \int |\phi|^2 \leq M/2\right\} \\ &= \inf\left\{\mathscr{E}_0(\sqrt{\rho}/\sqrt{2}) \mid \int \rho \leq M\right\}, \end{aligned} \tag{4.16}$$

where the second equality follows from the fact that I_M is monotonically decreasing as we can always put some excessive charge far away from the nuclei with negligible contribution to the energy. Furthermore, I_M is strictly convex for $M \in [0, M_c)$ for some $M_c \geq 2$, which follows the standard convexity argument applies to $\mathscr{E}_0(\sqrt{\rho}/\sqrt{2})$ as in the proof of parts (iii) and (iv) of [92, Corollary II.1] (see also the proof of convexity of the energy of the related Thomas-Fermi-von

Weizsäcker theory in [10]). We also have the relation

$$\frac{\partial I_M}{\partial M}\Big|_{M=2} = -E_0 < 0, \tag{4.17}$$

since E_0 is the Lagrange multiplier corresponding to the constraint $\int |\phi|^2 = M$. This in turn guarantees that $M_c > Z$, as in Part (i) of [92, Corollary II.1]. Therefore, denote $E_0(M)$ the corresponding Lagrange multiplier for I_M, we arrive at

$$-\frac{\partial E_0(M)}{\partial M}\Big|_{M=2} = \frac{\partial^2 I_M}{\partial M^2}\Big|_{M=2} > 0. \tag{4.18}$$

Following the analysis of [90, Theorem 3.1] using elliptic estimates, one observes that if $\phi \in H^1$ a solution to (4.14), then $\phi \in H^2$.

4.2.2 Implicit Function Theorem Analysis for Small α

We consider (4.3) for α small. First of all, by restricting to the class of solutions symmetric with respect to reflection in x, we know there exists a delocalized solution obeying the correct symmetry properties. For $\alpha = 0$, (4.3) is a convex functional and there exists a *unique* delocalized solution $\phi = \psi_+ = \psi_-$ such that $\|\phi\|_{L^2} = 1$. The following result extends the uniqueness to small α.

Proposition 4.2.1. *For $0 \le \alpha \le \alpha_0$ sufficiently small, there exists a unique, delocalized minimizer to* (4.3) *with $\|\phi\|_{L^2} = 1$. The dependence upon α is C^1.*

The remainder of this section is devoted to the proof of Proposition 4.2.1. The idea is to construct a symmetric solution branch stemming from the unique solution at $\alpha = 0$ that comes from the convexity of the energy functional in that limit. While the positive α perturbation is non-convex, the Euler-Lagrange equations can be solved using a Lyapunov-Schmidt reduction. In fact, we will see that we can construct an implicit function theorem argument using the

convexity at $\alpha = 0$ and in doing so, that locally only the symmetric branch will be possible. First, we will allow the branch to vary with respect to mass, then we will fix the Lagrange multipliers E_+ and E_- (in most cases we will observe $E_+ = E_-$ as a function of α to guarantee the mass 1 electron branch.

The Euler-Lagrange equations for $\mathcal{E}_{LDA,\alpha}$ give us a function on $(H^2)^2 \times \mathbb{R}^2$ defined as

$$F(\psi_+, \psi_-; \alpha, E) = \begin{pmatrix} -\frac{1}{2}\Delta\psi_+ + E_+\psi_+ + V\psi_+ + \left(v_c * \left(|\psi_+|^2 + |\psi_-|^2\right)\right)\psi_+ - \frac{4}{3}\alpha|\psi_+|^{\frac{2}{3}}\psi_+ \\ -\frac{1}{2}\Delta\psi_- + E_-\psi_- + V\psi_- + \left(v_c * \left(|\psi_+|^2 + |\psi_-|^2\right)\right)\psi_- - \frac{4}{3}\alpha|\psi_-|^{\frac{2}{3}}\psi_- \end{pmatrix} = 0. \tag{4.19}$$

To apply the Lyapunov-Schmidt reduction, we need to address the kernel of the Jacobian with respect to $\psi_\pm$ for the Euler-Lagrange equations. This is given by the operator

$$DF_\psi(\psi_+, \psi_-; \alpha, E_+, E_-)\begin{pmatrix} f_+ \\ f_- \end{pmatrix} = \begin{pmatrix} L_+ f_+ + 2\psi_+ v_c * (\psi_- \bar{f}_-) \\ 2\psi_- v_c * (\psi_+ \bar{f}_+) + L_- f_- \end{pmatrix} \tag{4.20}$$

for

$$L_+(\psi_\pm; \alpha, E_+) f_+ = \left(-\frac{1}{2}\Delta + E_+ + V + v_c * \left(|\psi_+|^2 + |\psi_-|^2\right) - \frac{20}{9}\alpha|\psi_+|^{\frac{2}{3}}\right) f_+ + 2\psi_+ v_c * (\psi_+ \bar{f}_+)$$

and similarly

$$L_-(\psi_\pm; \alpha, E_-) f_- = \left(-\frac{1}{2}\Delta + E_- + V + v_c * \left(|\psi_+|^2 + |\psi_-|^2\right) - \frac{20}{9}\alpha|\psi_-|^{\frac{2}{3}}\right) f_- + 2\psi_- v_c * (\psi_- \bar{f}_-).$$

For $\phi = \psi_+ = \psi_-$, the unique solution at $\alpha = 0$ with resulting Lagrange multiplier E_0

stemming from the convexity of $E_{LDA,0}$, we have

$$DF_{\psi}(\phi,\phi;0,E_0,E_0)\begin{pmatrix} f_+ \\ f_- \end{pmatrix} = \begin{pmatrix} L_{\phi,E_0}f_+ + 2\phi v_c * (\phi \bar{f}_-) \\ 2\phi v_c * (\phi \bar{f}_+) + L_{\phi,E_0}f_- \end{pmatrix}$$

for

$$L_{\phi,E_0}f = \left(-\frac{1}{2}\Delta + E_0 + V + 2v_c * |\phi|^2\right)f + 2\phi v_c * (\phi \bar{f}).$$

In the class of symmetric solutions, we actually have a reduced set of equations and can instead solve a scalar problem with parameters.

4.2.3 Analysis of the Linearized Operators for $\alpha = 0$

We prove here that at $\alpha = 0$, $\psi_+ = \psi_- = \phi$, $E = E_0$, then the linearized operator has a kernel, but it can only lead to solutions where ψ_+ and ψ_- take on different masses. This is a key step in applying the implicit function theorem in α locally. To see this, we linearize (4.14) to get the operator

$$\widetilde{L}_{\phi,E_0}f = \left(-\frac{1}{2}\Delta + E_0 + V + 2v_c * |\phi|^2\right)f + 4\phi v_c * (\phi \bar{f}). \tag{4.21}$$

We observe that the operator $\widetilde{L}_{\phi,E_0}$ can be written in the form

$$\widetilde{L}_{\phi,E_0} = -\frac{1}{2}\Delta + E_0 + V + V_{\phi} + W_{\phi},$$

where

$$V_{\phi}f = E_0 f + Vf + 2v_c * |\phi|^2 f$$

is a self-adjoint local operator with $1/|x|$ decay and

$$W_\phi = 4\phi v_c * (\phi \bar{f})$$

is a self-adjoint non-local operator with exponential decay. In both cases, we will see that these are bounded, relatively compact perturbations of the Laplacian, and hence argue that the continuous spectrum of L_{ϕ,E_0} is on the set $[E_0,\infty)$. Then, we will use a linear argument based around the convexity of solutions to the problem at $\alpha = 0$ to show that the kernel of L_{ϕ,E_0} is trivial. This will allow us to construct a family of solutions using the implicit function theorem.

Since $V + V_\phi + W_\phi$ is a relatively compact perturbation, we observe that the continuous spectrum of L_{ϕ,E_0} is the interval $[E_0,\infty)$ by applying Weyl's Theorem, see [114, 89] for instance, or [86] where the functional analysis of Hartree-style equations is discussed in some detail.

Lemma 4.2.2. *The operator $\widetilde{L}_{\phi,E_0}$ has only trivial kernel.*

Proof. Let us assume to the contrary there exists $f \in H^2$ such that

$$\widetilde{L}_{\phi,E_0} f = 0.$$

Then, we observe that

$$0 = \left\langle (-\tfrac{1}{2}\Delta + E_0 + V + V_\phi) f, f \right\rangle + \left\langle W_\phi f, f \right\rangle.$$

However, given the structure of W_ρ, it turns out that

$$\langle W_\phi f, f\rangle > 0 \text{ for } f \neq 0.$$

This is easiest to see this is by looking at the inner product in Fourier space.

Taking the orthogonal decomposition $f = \alpha\phi + \phi^\perp$ and using that ϕ is the unique

kernel of the operator $L_- = -\frac{1}{2}\Delta + E_0 + V + V_\phi$ and hence if $\phi^\perp \neq 0$, we observe that we have a contradiction immediately from the coercivity of L_-. However, if $\phi^\perp = 0$, then $\alpha \neq 0$ and we still observe positivity from the term $\langle W_\phi f, f\rangle$.

□

Remark 4.2.1. This is a similar strategy to that of standard semi-linear problems, however in such a case the perturbation of the L_- operator is negative in total and hence the spectral theory of the linearized operator must be understood in much greater detail. Here, the perturbation is actually positive, so the arguments are greatly simplified. It is also essential that we have a potential here, which has broken the translation invariance.

4.2.4 Construction of Solutions near $\alpha = 0$

Claim 4.2.3. *Since $E_{LDA,0}$ is a convex functional, the Jacobian $DF_\psi(\phi,\phi;0,E_0)$ has kernel given by* $\mathrm{span}\{(\phi,-\phi)\}$ *and as a result, a unique C^1 path in (α,E) can be constructed through symmetric functions in $H^2\times H^2$ using the implicit function theorem with fixed constraint $\|\psi_\pm\|_{L^2}=1$.*

Proof. We must study the invertibility of DF at $\alpha = 0$. In the restricted space, $\psi_+ = \psi_-$, the invertibility is established in Lemma 4.2.2 through the invertibility of $\widetilde{L}$. The remainder of the argument follows from a fairly standard application of the implicit function theorem. Indeed, we observe that if $DF\vec{f} = 0$, then $\tilde{L}(f_1+f_2)=0$ for $\vec{f}=(f_1,f_2)$. Hence, either f_1+f_2 is a non-trivial kernel function of $\tilde{L}$ or $f = f_1 = -f_2$ and f_1 is a non-trivial kernel function for a modified operator

$$\mathscr{L}_{\phi,E_0} f = \left(-\frac{1}{2}\Delta + E_0 + V + 2\nu_c * |\phi|^2\right) f,$$

which through the equation satisfies $\mathscr{L}\phi = 0$. Since $\phi > 0$, it is the ground state and simple, which establishes the result on the spectrum.

We note that the nature of the kernel is not so surprising at $\alpha = 0$, as a major symmetry of $E_{LDA,0}$ would be to simply use a rotation of (ψ_+,ψ_-), which is an invariant of the Lagrangian.

However, given that at $\alpha = 0$, we have $\psi_+ = \psi_- = \phi$, this symmetry generates no new solutions except the one we have found in the kernel. Using the convexity, we have uniqueness of the symmetric solution ϕ as a minimizer having fixed mass $\|\phi\|_{L^2}^2 = 1$.

The remaining proof relies on varying E using the standard Lyapunov-Schmidt construction of $\phi(E,\alpha)$ solving the Euler-Lagrange equation,

$$(\psi_+, \psi_-) = (\phi, \phi) + c_0(\phi, -\phi) + (\eta_+, -\eta_-),$$

for $\alpha \sim c_0^2$, $\int(\eta_+ + \eta_-)\phi dx = 0$ and $\|\eta\| \sim c_0^2$, see [77, Proposition 1] for a general discussion of the method. We observe that

$$\|\eta(c_0, E_\pm - E_0, \alpha)\|_{H^2} \lesssim c_0^2, \;\; |E_\pm - E_0| \lesssim c_0^2.$$

Indeed, expanding about (ϕ,ϕ) in this fashion we have

$$F(\phi,\phi;0,E_0) + DF(\phi,\phi;0,E_\pm)\begin{pmatrix}\eta_+\\ \eta_-\end{pmatrix} + \mathcal{O}\left(|\eta|^2 + c_0^2 + \alpha + (E_\pm - E_0)\phi\right) = \begin{pmatrix}0\\ 0\end{pmatrix}. \tag{4.22}$$

We note here that the linearization is $DF(\phi,\phi;0,E_\pm)$ and not $DF(\phi,\phi;0,E_0)$. Using the properties of DF, ϕ and E_0, we then observe that we can first solve for $(\eta_+,\eta_-) = (\eta_+,\eta_-)(c_0,E_\pm,\alpha)$ in

$$\begin{pmatrix}\eta_+\\ \eta_-\end{pmatrix} = (P^\perp DF(\phi,\phi;0,E_\pm)P^\perp)^{-1}P^\perp\mathcal{O}\left(|\eta|^2 + c_0^2 + \alpha + (E_\pm - E_0)\phi\right) \tag{4.23}$$

with $P^\perp\vec{f} = \vec{f} - \left\langle \vec{f}, (\phi,-\phi)^{\mathrm{T}}\right\rangle(\phi,-\phi)^{\mathrm{T}}$ applying the standard Implicit Function Theorem. This

implies that (4.22) is given by

$$\begin{aligned}\left(-\frac{1}{2}\Delta + E_\pm + V\right)\eta_\pm = (E_\pm - E_0)\phi + c_0(E_\pm - E_0)\phi - \alpha|\phi(1\pm c_0) + \eta_\pm|^{\frac{2}{3}}(\phi(1\pm c_0) + \eta_\pm) \\ + \nu_c * \left[2c_0^2\phi^2 + 2(1+c_0)\phi\eta_+ + 2(1-c_0)\phi\eta_- + \eta_+^2 + \eta_-^2\right]\phi \\ \pm c_0\nu_c * \left[2c_0^2\phi^2 + 2(1+c_0)\phi\eta_+ + 2(1-c_0)\phi\eta_- + \eta_+^2 + \eta_-^2\right]\phi \\ + \nu_c * \left[2\phi^2 + 2c_0^2\phi^2 + 2(1+c_0)\phi\eta_+ + 2(1-c_0)\phi\eta_- + \eta_+^2 + \eta_-^2\right]\eta_\pm.\end{aligned}$$

As we are taking $|E_\pm - E_0|$ small, $P^\perp DF(\phi,\phi;0,E_\pm)P^\perp$ is invertible since $P^\perp DF(\phi,\phi;0,E_0)P^\perp$ is invertible. We observe that by the Implicit Function Theorem we have

$$\|\vec{\eta}\|_{H^2} \leq C\big(c_0^2 + \alpha + (E_+ - E_0) + (E_- - E_0)\big).$$

Projecting (4.22) onto $(\phi,-\phi)$, we have[1]

$$(E_+ - E_0) - (E_- - E_0) + c_0[(E_+ - E_0) + (E_- - E_0)] + \mathcal{O}\left(\|\vec{\eta}\|_{L^2}^2 + c_0^3 + \alpha\big(c_0 + \|\vec{\eta}\|_{L^2}^{\frac{2}{3}}\big)\right) = 0,$$

which allows us to use the Implicit Function Theorem once again to solve for E_+ given E_- and write for instance

$$(E_+ - E_0) = (E_+ - E_0)(c_0, \alpha, E_- - E_0),$$

with

$$|E_+ - E_0| \leq C\big(c_0^3 + \alpha c_0 + \alpha^{\frac{5}{3}} + |E_- - E_0|\big).$$

[1] Here, we use the following bound pointed out to the authors by N. Visciglia: Let $\alpha > 0$ be given. Then for every $a, b \in \mathbb{C}$ we have the following inequality:

$$\big|(a+b)|a+b|^\alpha - a|a|^\alpha - b|b|^\alpha\big| \lesssim (|a||b|^\alpha + |b||a|^\alpha). \tag{4.24}$$

Now, using the two constraint equations for the mass, we have

$$\int (2c_0\phi + c_0^2\phi^2 + 2(1+c_0)\phi\eta_+ + \eta_+^2)dx = 0 \tag{4.25}$$

and

$$\int (-2c_0\phi + c_0^2\phi^2 + 2(1-c_0)\phi\eta_- + \eta_-^2)dx = 0. \tag{4.26}$$

Using the linear combination (4.25) + (4.26) and the orthogonality of (η_+, η_-) to $(\phi, -\phi)$, we first observe that

$$|E_- - E_0| \leq C(\alpha + c_0^2),$$

which implies for the linear combination (4.25) − (4.26), we can observe that

$$c_0^2 \leq C\alpha.$$

Once the overall dependence upon α has been determined, we realize that on the branch described above in (4.25) and (4.26), everything is indeed lower order to the $\mathcal{O}(c_0)$ term. Thus, $c_0 = 0$ lest we not move off the mass 1 branch.

Remark 4.2.2. From the sign changes (4.25) and (4.26), we expect that with no mass constraint the branch construction stemming from the kernel of DF to leading order leads to $E_+ = -E_-$. If we were allowed to make such a symmetric reduction, the arguments above can be simplified.

4.2.5 Construction of the Local Branch under the Symmetry Assumption

Using that the linearization preserves symmetric solutions, let us limit ourselves to solutions of the simplified Euler-Lagrange equation for $\phi(E, \alpha)$ given by

$$-\frac{1}{2}\Delta\phi + E\phi - V\phi + 2\int \frac{|\phi|^2(y)}{|x-y|}dy\phi - \alpha|\phi|^{\frac{2}{3}}\phi = 0.$$

The mass of ϕ is

$$M(E,\alpha) = \int |\phi|^2 dx.$$

By construction, $M(E_0, 0) = 1$. To find mass 1 states, using that $\phi = \phi(E,\alpha)$, we wish to find $E(\alpha)$ solving

$$M(E,\alpha) := \int |\phi(E(\alpha),\alpha)|^2 dx - 1 = 0.$$

Hence, we wish to apply the Implicit Function Theorem once more, which guarantees the solvability of $E(\alpha)$ provided

$$\frac{\partial M}{\partial E}|_{E=E_0,\alpha=0} \neq 0.$$

However, at $\alpha = 0$ this follows directly from (4.18). Using the Implicit Function Theorem for a small range of α, there is an $E = E(\alpha)$ satisfying the mass equation.

□

4.3 Localization and Symmetry Breaking for Large α

4.3.1 A Priori Energy Estimate

We consider a variational problem with only the kinetic and exchange terms:

$$\min_{\varphi:\int|\varphi|^2=1} F(\varphi) = \frac{1}{2}\int \left|\nabla\varphi\right|^2 - \int \left|\varphi\right|^{8/3}. \tag{4.27}$$

It is now classical in the theory of nonlinear Schrödinger equations that the minimizer of (4.27) exists and is radial and unique up to a translation, see for instance [134]. Denote φ the minimizer of (4.27) centered at zero, it satisfies

$$-\frac{1}{2}\Delta\varphi - \frac{4}{3}\left|\varphi\right|^{2/3}\varphi + E\varphi = 0 \tag{4.28}$$

with E being a strictly positive Lagrange multiplier. Moreover, φ decays exponentially as $|x| \to \infty$.

We consider dilation operators $\{D_t\}$ that preserve the L^2 norm

$$(D_t f)(x) = t^{3/2} f(tx). \tag{4.29}$$

Let x_+ and x_- minimize

$$\min\Big(\big\|\nabla\psi_\pm - \nabla(D_\alpha\varphi)(\cdot - x_\pm)\big\|_{L^2}^2 + E\big\|\psi_\pm - (D_\alpha\varphi)(\cdot - x_\pm)\big\|_{L^2}^2\Big). \tag{4.30}$$

We write the remainder as

$$\psi_\pm = \big(D_\alpha(\varphi + w_\pm)\big)(\cdot - x_\pm). \tag{4.31}$$

Correspondingly, we have $\varphi = D_\alpha^{-1}\tau_{x_\pm}^{-1}(\psi_\pm) - w_\pm$, to simplify notation, we denote

$$\widetilde{\psi}_\pm = D_\alpha^{-1}\tau_{x_\pm}^{-1}\psi_\pm = \alpha^{-3/2}\psi_\pm\Big(\frac{x + x_\pm}{\alpha}\Big). \tag{4.32}$$

As $\{\psi_\pm\}$ minimize E_α, we have

$$\begin{aligned} 0 &\le E_\alpha\big((D_\alpha\varphi)(\cdot - x_+), (D_\alpha\varphi)(\cdot - x_-)\big) - E_\alpha(\psi_+, \psi_-) \\ &= \alpha^2\big(2F(\varphi) - F(\widetilde{\psi}_+) - F(\widetilde{\psi}_-)\big) + \int V(\rho_\varphi - \rho_\psi) \\ &\qquad + \frac{1}{2}\iint \frac{\rho_\varphi(x)\rho_\varphi(y)}{|x-y|}\,\mathrm{d}x\,\mathrm{d}y - \frac{1}{2}\iint \frac{\rho_\psi(x)\rho_\psi(y)}{|x-y|}\,\mathrm{d}x\,\mathrm{d}y, \end{aligned} \tag{4.33}$$

where

$$\rho_\varphi(x) = \big|(D_\alpha\varphi)(x - x_+)\big|^2 + \big|(D_\alpha\varphi)(x - x_-)\big|^2.$$

Note that $\frac{1}{2}\iint \frac{\rho_\psi(x)\rho_\psi(y)}{|x-y|}\,\mathrm{d}x\,\mathrm{d}y \geq 0$, rearranging the terms, we obtain

$$F(\widetilde{\psi}_+) + F(\widetilde{\psi}_-) - 2F(\varphi) \leq \frac{1}{\alpha^2}\left(\int V\rho_\varphi + \frac{1}{2}\iint \frac{\rho_\varphi(x)\rho_\varphi(y)}{|x-y|}\,\mathrm{d}x\,\mathrm{d}y\right) - \frac{1}{\alpha^2}\int V\rho_\psi\,\mathrm{d}x. \tag{4.34}$$

By the scaling of $D_\alpha\varphi$, we have

$$\int V\rho_\varphi + \frac{1}{2}\iint \frac{\rho_\varphi(x)\rho_\varphi(y)}{|x-y|}\,\mathrm{d}x\,\mathrm{d}y \leq C\alpha. \tag{4.35}$$

To control the last term on the right hand side, recall that by Hardy's uncertainty principle, we have for any $X \in \mathbb{R}^3$ and $f \in H^1$

$$\int \frac{1}{|x-X|}|f(x)|^2\,\mathrm{d}x \leq 4\|f\|\|\nabla f\|. \tag{4.36}$$

Therefore, since $\|\psi_\pm\| = 1$, we have

$$-\int V\rho_\psi\,\mathrm{d}x = \int \frac{1}{|x-e_1|}\left(|\psi_+|^2 + |\psi_-|^2\right)\mathrm{d}x + \int \frac{1}{|x+e_1|}\left(|\psi_+|^2 + |\psi_-|^2\right)\mathrm{d}x \leq C\left(\|\nabla\psi_-\| + \|\nabla\psi_+\|\right). \tag{4.37}$$

Thus, we arrive at

$$\begin{aligned} F(\widetilde{\psi}_+) + F(\widetilde{\psi}_-) - 2F(\varphi) &\leq \frac{C}{\alpha} + \frac{C}{\alpha^2}\left(\|\nabla\psi_+\| + \|\nabla\psi_-\|\right) \\ &\leq \frac{C}{\alpha} + \frac{C}{\alpha^2}\left(\|\nabla D_\alpha(\varphi + w_+)\| + \|\nabla D_\alpha(\varphi + w_-)\|\right) \\ &\leq \frac{C}{\alpha} + \frac{C}{\alpha}\left(\|\nabla w_+\| + \|\nabla w_-\|\right) \\ &\leq \frac{C}{\alpha} + \frac{C}{\alpha}\left(\|\nabla w_+\|^2 + \|\nabla w_-\|^2\right). \end{aligned} \tag{4.38}$$

Using the result in [150] for the semilinear functional (4.27), the left hand side of (4.38)

is bounded from below as

$$F(\widetilde{\psi}_+) + F(\widetilde{\psi}_-) - 2F(\varphi) \geq g(\|w_+\|_{H^1}) + g(\|w_-\|_{H^1}), \tag{4.39}$$

where

$$g(t) = ct^2(1 - at^\theta - bt^4) \quad \text{with} \quad a, b, c, \theta > 0. \tag{4.40}$$

Combining (4.38) and (4.39), we conclude that

$$\lim_{\alpha\to\infty} \|w_\pm\|_{H^1} = \lim_{\alpha\to\infty} \|\widetilde{\psi}_\pm - \varphi\|_{H^1} = 0. \tag{4.41}$$

In other words, up to translation and dilation, the minimizer of (4.7) is close to the minimizer of the semilinear problem (4.27) for α large.

4.3.2 Location Optimization

We further determine the translation vectors $x_\pm$. We claim that as $\alpha \to \infty$, the translation vectors $x_\pm \to \pm e_1$ (up to swapping x_+ and x_-, recall that swapping ψ_+ and ψ_- does not change the energy). The key observation is that the kinetic and exchange energy terms are invariant with respect to translation, and hence $x_\pm$ are determined by the potential and Coulomb repulsion terms, which are higher order terms when α is large.

For this, we consider shifted minimizers

$$\widehat{\psi}_+ = \psi_+(\cdot + e_1 + x_+) \quad \text{and} \quad \widehat{\psi}_- = \psi_-(\cdot - e_1 + x_-). \tag{4.42}$$

By (4.31), we have

$$\widehat{\psi}_\pm = (D_\alpha \varphi)(\cdot \pm e_1) + (D_\alpha w_\pm)(\cdot \pm e_1). \tag{4.43}$$

Due to minimality, we have

$$\begin{aligned} 0 &\le E_\alpha(\widehat{\psi}_+, \widehat{\psi}_-) - E_\alpha(\psi_+, \psi_-) \\ &= \int V(\rho_{\widehat{\psi}} - \rho_\psi) + \frac{1}{2}\iint \frac{\rho_{\widehat{\psi}}(x)\rho_{\widehat{\psi}}(y)}{|x-y|}\,\mathrm{d}x\,\mathrm{d}y - \frac{1}{2}\iint \frac{\rho_\psi(x)\rho_\psi(y)}{|x-y|}\,\mathrm{d}x\,\mathrm{d}y. \end{aligned} \tag{4.44}$$

Recall ρ_φ and similarly define $\rho_{\widehat{\varphi}}$ as

$$\begin{aligned} \rho_\varphi(x) &= \left|(D_\alpha\varphi)(x-x_+)\right|^2 + \left|(D_\alpha\varphi)(x-x_-)\right|^2; \\ \rho_{\widehat{\varphi}}(x) &= \left|(D_\alpha\varphi)(x+e_1)\right|^2 + \left|(D_\alpha\varphi)(x-e_1)\right|^2. \end{aligned}$$

Denoting

$$\delta_{\mathrm{VC}}(\rho_1, \rho_2) = \int V(\rho_1 - \rho_2) + \frac{1}{2}\iint \frac{\rho_1(x)\rho_1(y)}{|x-y|}\,\mathrm{d}x\,\mathrm{d}y - \frac{1}{2}\iint \frac{\rho_2(x)\rho_2(y)}{|x-y|}\,\mathrm{d}x\,\mathrm{d}y, \tag{4.45}$$

we rewrite (4.44) as

$$\delta_{\mathrm{VC}}(\rho_{\widehat{\psi}}, \rho_\psi) = \delta_{\mathrm{VC}}(\rho_{\widehat{\psi}}, \rho_{\widehat{\varphi}}) + \delta_{\mathrm{VC}}(\rho_{\widehat{\varphi}}, \rho_\varphi) + \delta_{\mathrm{VC}}(\rho_\varphi, \rho_\psi) \ge 0. \tag{4.46}$$

Let us estimate $\delta_{\mathrm{VC}}(\rho_\varphi, \rho_\psi)$ first. For the potential term, using (4.36) for $f = \left|\rho_\varphi - \rho_\psi\right|^{1/2}$,

$$\int \left|V(\rho_\varphi - \rho_\psi)\right| \le C\left\|\left|\rho_\varphi - \rho_\psi\right|^{1/2}\right\|_{L^2}\left\|\nabla\left|\rho_\varphi - \rho_\psi\right|^{1/2}\right\|_{L^2} \le C\left\|\nabla\left|\rho_\varphi - \rho_\psi\right|^{1/2}\right\|_{L^2}. \tag{4.47}$$

For the difference in Coulomb energy

$$\begin{aligned}\left|\frac{1}{2}\iint\frac{\rho_\varphi(x)\rho_\varphi(y)}{|x-y|}\,\mathrm{d}x\,\mathrm{d}y-\frac{1}{2}\iint\frac{\rho_\psi(x)\rho_\psi(y)}{|x-y|}\,\mathrm{d}x\,\mathrm{d}y\right|&\\ \leq\iint\frac{\left|\rho_\varphi-\rho_\psi\right|(x)\rho_\varphi(y)}{|x-y|}\,\mathrm{d}x\,\mathrm{d}y+\frac{1}{2}\iint\frac{(\rho_\varphi-\rho_\psi)(x)(\rho_\varphi-\rho_\psi)(y)}{|x-y|}\,\mathrm{d}x\,\mathrm{d}y&\\ \leq C\left\|\rho_\varphi-\rho_\psi\right\|_{L^{3/2}}\left\|\rho_\varphi\right\|_{L^1}+C\left\|\rho_\varphi-\rho_\psi\right\|_{L^{6/5}}^2,&\end{aligned}\tag{4.48}$$

where the last line uses the Hardy-Littlewood-Sobolev inequality. Observe that using interpolation and Gargliardo-Nirenberg-Sobolev inequality, we have

$$\|f\|_{L^{6/5}}\leq\|f\|_{L^1}^{3/4}\|f\|_{L^3}^{1/4}\leq C\|f\|_{L^1}^{3/4}\left\|\nabla\sqrt{f}\right\|_{L^2}^{1/2},\tag{4.49}$$

$$\|f\|_{L^{3/2}}\leq\|f\|_{L^1}^{1/2}\|f\|_{L^3}^{1/2}\leq C\|f\|_{L^1}^{1/2}\left\|\nabla\sqrt{f}\right\|_{L^2}.\tag{4.50}$$

Combined with the above three inequalities, we get

$$\left|\frac{1}{2}\iint\frac{\rho_\varphi(x)\rho_\varphi(y)}{|x-y|}\,\mathrm{d}x\,\mathrm{d}y-\frac{1}{2}\iint\frac{\rho_\psi(x)\rho_\psi(y)}{|x-y|}\,\mathrm{d}x\,\mathrm{d}y\right|\leq C\left\|\nabla\left|\rho_\varphi-\rho_\psi\right|^{1/2}\right\|_{L^2}.\tag{4.51}$$

To estimate the right hand side of (4.47) and (4.51), by definition

$$\begin{aligned}\left\|\nabla\left|\rho_\varphi-\rho_\psi\right|^{1/2}\right\|_{L^2}&\leq\left\|\nabla\left(2|D_\alpha\varphi||D_\alpha w_+|+2|D_\alpha\varphi||D_\alpha w_-|+|D_\alpha w_+|^2+|D_\alpha w_-|^2\right)^{1/2}\right\|_{L^2}\\ &\leq C\Big(\left\|\nabla\left(|D_\alpha\varphi||D_\alpha w_+|\right)^{1/2}\right\|_{L^2}+\left\|\nabla\left(|D_\alpha\varphi||D_\alpha w_-|\right)^{1/2}\right\|_{L^2}\\ &\qquad+\left\|\nabla|D_\alpha w_+|\right\|_{L^2}+\left\|\nabla|D_\alpha w_-|\right\|_{L^2}\Big)\\ &\leq C\alpha\left(\|w_+\|_{H^1}+\|w_-\|_{H^1}\right),\end{aligned}\tag{4.52}$$

where we have used the convexity of $\left|\nabla\sqrt{\rho}\right|^2$ and the Cauchy-Schwartz inequality. Note that the α pre-factor on the right hand side is natural from the scaling, since the characteristic

length scale of ρ_φ is order $1/\alpha$ due to the construction by dilation. Therefore, to sum up,

$$\left|\delta_{\mathrm{VC}}(\rho_\varphi,\rho_\psi)\right| \le C\alpha\big(\|w_+\|_{H^1}+\|w_-\|_{H^1}\big). \tag{4.53}$$

It is easy to check that the same upper bound also holds for $\delta_{\mathrm{VC}}(\rho_{\widehat{\varphi}},\rho_{\widehat{\psi}})$. Thus,

$$\delta_{\mathrm{VC}}(\rho_{\widehat{\varphi}},\rho_\varphi) \ge -C\alpha\big(\|w_+\|_{H^1}+\|w_-\|_{H^1}\big). \tag{4.54}$$

We now turn the above estimate of the Coulomb energy difference into an estimate of the translation vectors $x_\pm$. For this, we calculate more explicitly $\delta_{\mathrm{VC}}(\rho_{\widehat{\varphi}},\rho_\varphi)$ (recall that φ is the unique radial minimizer to the semilinear functional (4.27)). We have

$$\begin{aligned}\delta_{\mathrm{VC}}(\rho_\varphi,\rho_{\widehat{\varphi}}) = \int V(\rho_\varphi-\rho_{\widehat{\varphi}}) &+ \iint \frac{\left|D_\alpha\varphi\right|^2(x-x_+)\left|D_\alpha\varphi\right|^2(y-x_-)}{|x-y|}\,\mathrm{d}x\,\mathrm{d}y \\ &- \iint \frac{\left|D_\alpha\varphi\right|^2(x-x_+)\left|D_\alpha\varphi\right|^2(y-x_-)}{|x-y|}\,\mathrm{d}x\,\mathrm{d}y.\end{aligned} \tag{4.55}$$

As φ decays exponentially, we have

$$\iint \frac{\left|D_\alpha\varphi\right|^2(x-x_+)\left|D_\alpha\varphi\right|^2(y-x_-)}{|x-y|}\,\mathrm{d}x\,\mathrm{d}y \lesssim \frac{1}{\alpha}, \tag{4.56}$$

and therefore

$$\int V(\rho_\varphi-\rho_{\widehat{\varphi}}) + \iint \frac{\left|D_\alpha\varphi\right|^2(x-x_+)\left|D_\alpha\varphi\right|^2(y-x_-)}{|x-y|}\,\mathrm{d}x\,\mathrm{d}y \le C\alpha\big(\|w_+\|_{H^1}+\|w_-\|_{H^1}\big)+\mathcal{O}(\alpha^{-1}). \tag{4.57}$$

This implies

$$\lim_{\alpha\to\infty}\frac{1}{\alpha}\int V(\rho_\varphi-\rho_{\widehat{\varphi}})$$
$$=\lim_{\alpha\to\infty}-\frac{1}{\alpha}\int\Big(\frac{1}{|x-e_1|}+\frac{1}{|x+e_1|}\Big)\big(|D_\alpha\varphi|^2(x-x_+)-|D_\alpha\varphi|^2(x-e_1)\big)\,\mathrm{d}x$$
$$+\lim_{\alpha\to\infty}-\frac{1}{\alpha}\int\Big(\frac{1}{|x-e_1|}+\frac{1}{|x+e_1|}\Big)\big(|D_\alpha\varphi|^2(x-x_-)-|D_\alpha\varphi|^2(x+e_1)\big)\,\mathrm{d}x=0, \quad (4.58)$$

since the second term on the left hand side of (4.57) is non-negative. Note that the two limits in the middle of the above equation are both non-negative. We have

$$\lim_{\alpha\to\infty}-\frac{1}{\alpha}\int\Big(\frac{1}{|x-e_1|}+\frac{1}{|x+e_1|}\Big)\big(|D_\alpha\varphi|^2(x-x_+)-|D_\alpha\varphi|^2(x-e_1)\big)\,\mathrm{d}x=0. \quad (4.59)$$

This implies that $\min\{|x_+-e_1|,|x_++e_1|\}$ converges to zero, and similarly for x_-. Thus, as $\alpha\to\infty$, $x_\pm$ approaches $\{e_1,-e_1\}$. They cannot converge to the same point, as otherwise the Coulomb interaction is obviously higher. Therefore, we arrive at the conclusion.

4.4 Numerical Solution to Kohn-Sham SDFT (KS-SDFT) Equations for ψ_+ and ψ_- as a Function of α

The variation of the energy functional given in Eq. (4.3) with normalization constraints, leads to Euler-Lagrange equations defining the spin up, ψ_+, and the spin down, ψ_-, KS-SDFT orbital solutions as a function of exchange strength α. In this section we outline the finite element methods (FEM) [13, 18] we used to produce numerical solutions to these equations and determine their stability. These solutions, characterized by the symmetry of the orbital functions and their localization within the molecular framework, were used to explore the transitions between the regions of stability identified by the theorems in Sections 4.2 and 4.3.

In the process of generating these numerical solutions additional stable solution to the Euler Lagrange equations are identified and their stationary character validated via Hessian analysis (see appendix). These may have important consequences for the application of Kohn-Sham methods but were not analyzed above.

An important feature of the FEM approach we used is that the expansions of ψ_- and ψ_+ in the FEM basis [95] are not constrained by any preconceived notion as to the nature of the solution as is implicit in the atomic orbital expansion basis of quantum chemistry software [107, 135, 51]. This is particularly important in our application because of the forms of the KS solutions to Eq.(4.3) as a function of α (e.g. for large α) are unknown. The details of the numerical problem and the FEM method we developed for its solution are described in more detail in the Appendix. A novel feature of the numerical method we have used is that its time to solution scales linearly with the size of the basis [70].

4.4.1 Overview of Numerical Method (FEM)

Our numerical implementations are based on application of the Python FEniCS finite element (FEM) package [95] [70], which is a collection of free software with an extensive list of features for automated, efficient finite element solution methods for differential equations. The source codes implementing the linear scaling finite element solver described below can be found at `https://fenicsproject.org/`. More details specific to our calculation are given in the Appendix.

The FEM calculation domain used here is a fixed square box of dimension $50 \times 50 \times 50$ atomic units which easily contains the H_2 molecule (size ≈ 2 atomic units). Because the bound state molecular orbitals decay exponentially away from the positions of the nucleus, we apply zero boundary conditions at the domain edges for the wave functions. The Coulomb potentials are calculated from Poisson's equation using free space boundary conditions.The singularities of the attractive nuclear potentials, Eq. (4.1) are removed by adding a small positive constant

in the denominator [70].

To accommodate the more rapid variation of the ψ functions near the atomic nucleus the finite element grid is adapted within the domain, see Figure 4.1. This is an essential feature of atomic and molecular electronic structure calculations [26, 79, 27] that do not introduce pseudopotentials [36].

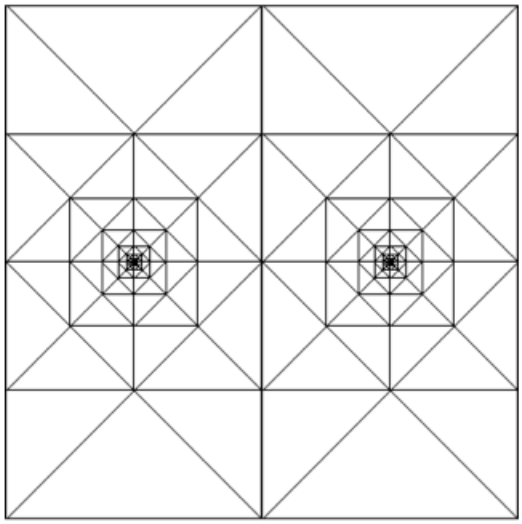


Figure 4.1: A representation of the finite element grid used in calculation. Each triangle represents a tetrahedron in the real calculation. Note that the density of the mesh is significantly increased near the two atomic nuclei (see appendix for further discussion as to how this mesh is generated).

In the FEM calculation each molecular orbital (ψ_+ or ψ_-) is written as an expansion in a finite element basis, η_i, with local support centered on the grid points in Figure 4.1[95], giving,

$$\psi_\pm = \sum_{i=1}^{M} c_{\pm,i}\eta_i. \tag{4.60}$$

There are M basis functions, where M is the total number of points in the grid and η_i the finite element basis functions (piecewise linear elements with local support) (see Appendix and [26] for more detail). The variation of the functional Eq. (4.3) expanded in the basis as in Eq. (4.60)

leads to generalized eigenvalue problems which must be solved self-consistently. These may be written as,

$$(-\frac{1}{2}\Delta - \epsilon_i)\psi_\pm = V(\rho)\psi_\pm. \tag{4.61}$$

where total electron density is $\rho = (\psi_-^2 + \psi_+^2)$. The eigenvalue problem is solved using an iterative process in which for step k the $\psi_\pm$ on right hand side of Eq. (4.61) and the orbital energies, $\epsilon_\pm^k$, at step k are assigned the the values and functionality from the $k-1$ step (see Appendix and [70]).

Eq. (4.61) is solved using the FEniCS software package (see Appendix and [70] for more detail). This package implements a conjugate gradient solver (generalized minimal residual method, GMRES [127]) after preconditioning with an algebraic multigrid preconditioner (AMG, BoomerAMG from the Hypre Library [2, 19, 147, 139, 57]). The application of the AMG solver leads to the linear in basis set time to solution feature of the numerical method.

An initial guess for the molecular orbitals (MOs) for the FEM solutions is necessary to start the iteration. Here we used H atom Slater Type Orbitals (STO-3G) generated from the NWChem data base [146] to form molecular orbitals for all α. Given two STO-3G functions centered on the atom center and designated as ϕ_1 and ϕ_2. The initial MOs for symmetric solution are $(\phi_1 + \phi_2)/2$ while the initial states when localized solutions are expected as ϕ_1 and ϕ_2 respectively, see [65, 51]. When α is very small, even the initial MOs are localized states ϕ_1 and ϕ_2, the final solution becomes delocalized state. For very large α the final solution may not be well approximated by this initial condition. However, we have not had problems with convergence of the method described in the appendix.

4.4.2 Numerical Results of DFT/ FEM Calculations

The solution to the optimization problem posed by Eq. (4.3) are function of the internuclear distance, R, and the strength of the Dirac exchange, α. Consistent with the Pauli

principle (requirement of Fermion wave function being antisymmetric) we assign individual electrons either to a spin up ψ_+ or spin down ψ_- spin eigenvector (the spin orbitals functions are products of a spacial function and a spin up or down eigenvector). With the further approximation of Dirac exchange and integration over the spin degrees of freedom this leads to the Kohn-Sham (KS) local spin density functional form expressed in Eq. (4.3)[108].

Formal results identifying features of the minimizers of Eq. (4.3) are given above. This is a two electron problem. In this formalism the forms of the spacial parts of the orbital wave functions are completely independent and the symmetry of the total density is not constrained. However, for most of the stationary solutions that we have found the total electron density has the symmetry of the H_2 molecule. We have shown this to be true for the lowest energy solution of Eq. (4.3) in both the large α and small α limits that we have proven to exist above. On the other hand, as we will illustrate in the following, the symmetry of the spacial parts of the individual spin orbitals may be broken in a way that still preserves the symmetry of the molecule for the total density. This break in symmetry occurs with a bifurcation and leads to electron localization. In applications of DFT to large molecules or condensed materials this localization is interpreted in term of the observed spin states of lattices (or molecules) (e.g. antiferromagnetic states in condensed materials [43, 122, 109]) . Thus the prediction of this spin ordering present in these states is an important objective of the application of DFT methods to molecular and condensed matter systems. The accuracies of the total energies are within 0.02 au for H_2 molecule in our calculations.

Bifurcation in the R Dimension

The optimized total energy as the H_2 molecular bond is lengthened for at fixed $\alpha = 0.93$ (from Eq. (4.3) and α similar to the value used in the application of SLDA to molecular and condensed matter problems) is shown in Figure 4.2. Remarkably for given α and sufficiently

small R the solutions for orbital wave functions ψ_+ and ψ_- converge to the same function even under full variation with no symmetry restriction. This is consistent with the fixed R, small α analysis in Section 4.2. This solution is the same as the so called *restricted* solution generated by enforcing double filling (spin up and spin down electrons states) of a single spacial orbital to form the two electron wave function. That is the *restricted* DFT (RDFT) solution in which ψ_+ and ψ_- are the same function is the lowest energy solution to the optimization problem posed in Eq. (4.3) even when each orbital function is varied independently without constraint. Similar behavior is observed in the Hartree or Hartree-Fock model of electronic structure for the two electron system. These solutions are important because the restricted DFT solutions are widely used in quantum chemistry applications [135, 51] and it is important to be aware of their region of stability.

As the H_2 bond length is extended as illustrated in Figure 4.2 ($R >\approx 2.75$au) the solution bifurcates creating two two electron product (singlet determinant [135, 108]) solutions. In the lowest energy state (lower branch, green line) one symmetry broken electron orbital (say the spin up state) is localized around one site and the other orbital function state (spin down) is localized around the 2^{nd} (see green density distribution bottom right Figure 4.2). The product wave function (total density) for this branch leads to a spin localized density distribution (*spin up and spin down electrons localized on different atomic sites with total spin zero*). This spin distribution is consistent with an antiferromagnetic state for the H_2 molecule. Since spin ordered condensed systems are common targets for DFT prediction, this is an important dimension for variation in designing DFT representations of spin ordered systems [43, 122, 109].

The upper energy branch in Figure 4.2 is a continuation of the restricted solution in which the spin up and spin down orbitals have the same spacial dependence (no localization, blue density distribution bottom right Figure 4.2). We note that this solution continues as a stationary solution even for large R.

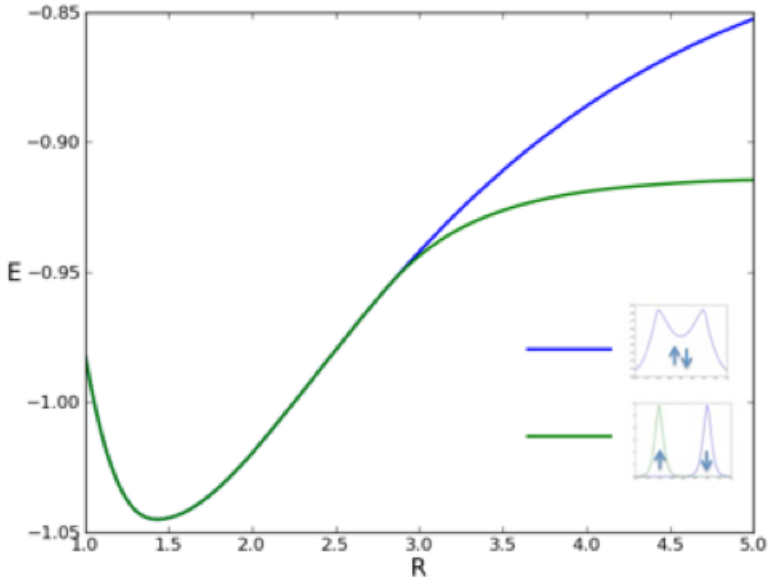


Figure 4.2: Bifurcation of LSDA for H_2 in the R dimension with $\alpha = 0.93$. The bifurcation point is at $R = 2.75$ au.

Note that the symmetry of total electron density is preserved in both the upper and lower states as in insert in Figure (4.2).

Hessian of Bifurcated Solutions for R Variation

As discussed after the bifurcation illustrated in Figure 4.2 there are two solutions for $R > 2.75$ au. These (one spin localized/antiferomagnetic (green line) and one restricted (no localized spin) blue line) solutions are analogous to solution of spin ordered condensed systems and are widely interpreted in terms of the observed spin ordering of stable and unstable phases[122, 43, 109]. Since these solutions are remarkable stable in calculations, they can be difficult to identify on the basis of currently used optimization methods [122]. Typically several solutions may appear as stable in uncontrolled calculations. (For a brief overview of how spin is controlled in condensed matter calculations see reference [36].)

The stability/metastability of the solutions along the 2 branches In Figure (4.2) can

be determined from the Hessian associated with the optimization problem Eq. (4.3) (see Appendix). At the bifurcation point, the gradient is zero. Numerical estimates of the eigenvalues of the Hessian the optimization problem Eq. (4.3) (also calculated via the FEM see appendix) show there is one negative eigenvalue for the RDFT solution beyond the bifurcation point. The combination of the zero gradient and the presence of the single negative eigenvalue shows that this is a metastable point in the energy surface. This is result may be important to DFT applications in which it is known that it is often difficult to find the true spin ordered minimum energy past the bifurcation point. This problem may be caused by the metastability of the delocalized state. We collect this information in a table for fixed $\alpha = .93$ (value consistent with the α typically used in DFT applications) varying the bond length in Table 4.1.

Table 4.1: Eigenvalues for the Hessian matrix, $\alpha = .93$ for various bond lengths

Bond Length	Solution	Result	Details
2.0 a.u.	delocalized solution	Local Minimizer	all evs on the constraint manifold > 0.
3.5+ a.u.	delocalized solution	Saddle Point	1 ev on the constraint manifold < 0.
3.5+ a.u.	localized solution	Local Minimizer	all evs on the constraint manifold > 0.

Bifurcation in the α Dimension

Figure 4.3 shows the symmetry breaking bifurcation points for LSDA solutions of Eq. (refeq:LDA) with strength of the exchange contribution, α, for fixed bond lengths $R =$ 2.0 au. As mentioned above adjustment of parameters such as α in the density functional formalism may improve DFT model performance for spin ordered systems [112, 122]. For a fixed bond length and in the small α domain, there are two identical degenerate spacial solutions (for spin up and spin down) degenerate solutions for the global minimum energy. These solutions (herein called the delocalized solutions) have peaks at the two atom centers, spread over the whole molecule and have the symmetry of the molecule. In this region, if a numerical solutions are initiated with broken symmetry the ψ_+ and ψ_- solutions evolve

to have the same spacial dependance, $\psi_+ = \psi_-$. These solution are equivalent to the single orbital solution of of the restricted or doubly filled DFT product function. See the analysis in Section 4.2 for the demonstration of this result, but the underlying reason is that the Coulomb repulsion is somewhat insensitive to the localization of the total density and the kinetic energy dominates over the exchange potential contribution in Eq. (4.3). Beyond the bifurcation point (as illustrated in Figure (3) , the broken symmetry solutions with excess spin on each atom (localized solutions) appears and the product solution is the global minimizer. The the total density still still has the symmetry of the molecule. The restricted solutions with higher energy still exists along the upper branch of the bifurcation curve. These solution have not been discussed above. Hessian analysis shows that delocalized solution is a metastable solution with Hessian eigenvalues demonstrating their metastable property similar to the bifurcation in R, Figure 2, namely there is one negative eigenvalue for the RDFT solutions above the lowest energy curve (blue curve, Figure 2) beyond the bifurcation point.

As α is further increased (at constant R) a variety of new bifurcations appear. The exchange potential contributes much more than the Coulomb potential so the solution tends to be localized instead of delocalized. The localized solution (blue line Figure 3) remains the minimizer. The symmetric delocalized solution (dark green and light green Figure 4.3) is the highest energy. However for very high α the maximum density moves to the middle of the bond. For $\alpha > 6$ Figure 4.3 the high energy delocalized solutions break symmetry and forms two lower energy two electron solutions on centered on the atom centers (red line Figure 4.3). We note that the antiferromagnetic solution (blue line) is the global solution for all large α. This is an important result since this is the solution generally associated with magnetic behavior in real materials.

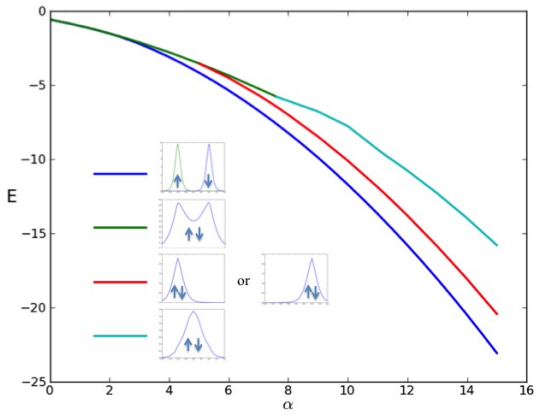


Figure 4.3: Several numerically constructed branches of the bifurcation of LSDA for H_2 in the α parameter with $R = 2.0$ au showing the relevant $\psi_{\pm}$ profiles.

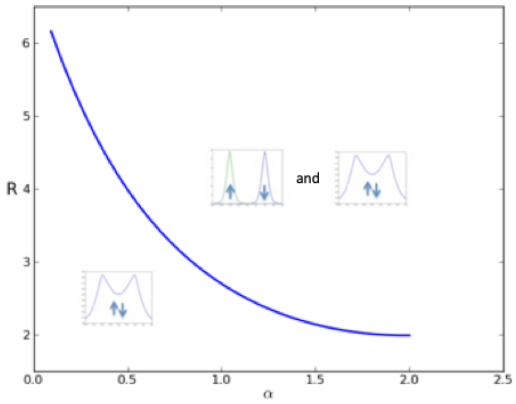


Figure 4.4: The first symmetry breaking bifurcation of LSDA for H_2 as a phase diagram in R and α. Below the line only delocalized states are present while above the line there are both delocalized and localized states.

Onset of Ferromagnetic Behavior as Bond Length is Increased

Since the bond length corresponding to beginning of antiferromagnetic behavior (spin localization) occur after the first bifurcation and it is common to adjust the strength of the Dirac exchange to improve agreement of mode, we show the variation of the first bifurcation point for different α in Figure 4.4. Note that for very small α the bond length for bifurcation becomes very long.

4.5 Discussion and Future Works

A similar analysis to the large α case gives that the ground state Euler-Lagrange equation for large R can be transformed to an equation of the form

$$-\Delta\phi_{\pm} + R^2E(R) - RV_1\phi_{\pm} + \frac{2}{R}\int \frac{|\phi_+|^2 + |\phi_-|^2}{|x-y|}\phi_{\pm}(x) + R\alpha|\phi_{\pm}|^{\frac{2}{3}}\phi_{\pm} = 0, \tag{4.62}$$

taking $\phi_{\pm} = R^{\frac{3}{2}}\psi_{\pm}$. This correlates to a new problem with no Coulomb repulsion, large but unit distance apart nuclear masses $Z = R$, and a very strong exchange-correlation nonlinearity $R\alpha$. Thus, the main issue is to study the nature of the stable curve for a large nuclear mass with strong exchange-correlation nonlinearity and observe what the nature of the Lagrange multiplier $R^2E(R)$ should be as $R \to \infty$. The intuition is that this scales the problem to be localized since moving along the stable branch of states from low electron mass (small Lagrange multiplier) for the potential V_1 to large electron mass (large Lagrange multiplier) eventually concentrates onto localized states over each well. As the nonlinearity is growing in strength with the nuclear potential, this bifurcation onto localized modes will still happen at relatively low mass since after a scaling the model Lagrangian is

$$\frac{1}{2}\int |\nabla\phi|^2 dx + R\left(\int V_1|\phi|^2 dx - \alpha\int |\phi|^{\frac{8}{3}} dx\right), \ \ \|\phi\|_{L^2} = 1, \tag{4.63}$$

meaning the behavior for large R should correlate to the mass 1 stability profile of the simplified (6.2).

Choosing $\phi_{\pm} = R^{\frac{3}{2}}\psi_{\pm}(Rx)$, the resulting modified Lagrangian has critical points given by

$$-\epsilon^2\Delta\phi_{\pm} + \phi_{\pm} - V_1\phi_{\pm} + \int \frac{|\phi_+|^2 + |\phi_-|^2}{|x-y|}\phi_{\pm}(x) + \alpha|\phi_{\pm}|^{\frac{2}{3}}\phi_{\pm} = 0, \tag{4.64}$$

which looks like a singular-perturbation Ginzburg-Landau style. As a result, this motivates the

following question for a (strange) Hydrogen model: Is the minimizer of

$$E_H(u) = \frac{1}{2}\int |\nabla u|^2 \, \mathrm{d}x - \int \frac{Z}{|x|}|u|^2(x)\,\mathrm{d}x + \frac{1}{2}\iint \frac{|u|^2(x)|u|^2(y)}{|x-y|}\,\mathrm{d}x\,\mathrm{d}y - \int |u|^{8/3} dx \qquad (4.65)$$

such that $\|u\|_{L^2} = 1$ orbitally stable. This has been answered in some sense when $Z = 0$ in [125] when the mass is that of the absolute minimizer. Understanding what occurs for the natural electronic mass 1 requires further investigation of this model and will be a topic of future work.

Chapter 4 in full, is a reprint of the material "Symmetry Breaking in Density Functional Theory due to Dirac Exchange for a Hydrogen Molecule" by Michael Holst, Houdong Hu, Jianfeng Lu, Jeremy L. Marzuola, Duo Song and John Weare, submitted to Journal of Nonlinear Science on March 8 2019, arXiv:1902.03497.

Chapter 5

Impurity Solvers and Dynamic Mean Field Theory Self Consistancy

5.1 Introduction to DMFT

The solution to the many electron problem in highly correlated condensed materials is computationally intractable because of the requirement to accurately describe the strong electron correlations in the many electron wave functions created by the high energy cost of placing two electrons on the same lattice site. The strategy of the Dynamic Mean Field Theory (DMFT) approach is to divide this problem into two parts. First the calculation of the smoothly varying behavior of the wave function with a mean field method (e.g., DFT or diagonalization of the independent particle part of a lattice Hamiltonian). And second to treat the quickly varying highly correlated behavior of paired electrons on single lattice site with a many body approach which can in principle be taken to "exact" accuracy (see Fig. 5.1) [66]. It is assumed that the site electron (an "Anderson impurity" selected from the lattice) experiences an average field of the lattice (the Weiss Field) see Fig. 5.1. These two calculations are merged by the ansatz that the local Green's function (self energy) of a single site of the lattice, $G_{d\uparrow d\uparrow}$ defined

below, is the same as the Green's function (self energy) for an appropriately defined Anderson impurity model (AIM) (e.g., described by a d atomic orbital) embedded in the mean field (not the mean field solution of the lattice electrons, see below) of the external lattice. In the limit of infinite connectivity (e.g.,consider a tight binding Hamiltonian with an infinite number of nearest neighbors) it can be shown that the DMFT calculation gives the exact solution.

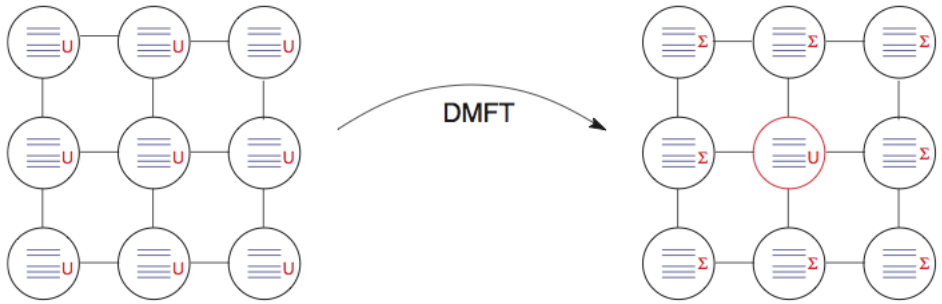


Figure 5.1: Impurity in Lattice right grid in red. The remaining atoms (right side) create a dynamic means field

The computationally demanding part of the DMFT calculation is the cost of the high level solution to the AIM problem. In the following we develop two numerical methods for this problem: a Quantum Monte Carlo scheme, the Hirsch Fye (HF) impurity solver: and an exact diagonalization scheme, the ED impurity solver. In both these models the highly correlated electron-electron interaction on the *lattice electronic structure model* is defined (see more below) in terms of a single orbital, ψ_i located on each lattice site, (i.e., a "Hubbard Model"). These orbitals are assumed to be very localized (think of 3d atomic orbitals). The electron-electron interaction energy is modeled in terms of *a single site interaction* with a Hubbard U parameter. In both methods the structure of the AIM Hamiltonian is determined in a self consistent cycle by adjusting the AIM model parameters until the local Greens functions of the lattice and the impurity are equal, for a given U. The self constancy cycles used to achieve consistency between the lattice Greens functions and the impurity Greens functions are illustrated in Figures 5.2 and 5.3 and discussed in separate sections.

5.2 Defining the Problem

The lattice electrons are governed by the full lattice Hamiltonian H_{Lattice}, defined within a Hubbard model as

$$H_{\text{Lattice}} = -\sum_{i,j,\sigma} t_{ij} c^{\dagger}_{i\sigma} c_{j\sigma} + \sum_{i} U n_{i\uparrow} n_{i\downarrow} \tag{5.1}$$

In this Hamiltonian the c_i and $c^{\dagger}_i$ are annihilation and creation operators corresponding to the creation or annihilation of an *local orbital* site function, ψ_i on lattice site i. $n_{i\uparrow}$ is the number operator for up spins on site i. t_{ij} is the usual hopping parameter. n_s is the number of sites in the lattice. The parameter U models the strong Coulomb interaction cost for double occupancy.

It is often convenient to use a representation in which the independent particle model part of the the Hamiltonian in Eq. (5.1) is diagonalized. That is we define annilhilation and creation operators c_k and $c^{\dagger}_k$ such that,

$$\sum_{i,j,\sigma}^{n_s} t_{ij} c^{\dagger}_{i\sigma} c_{j\sigma} = \sum_{k,\sigma}^{n_s} \epsilon_k c^{\dagger}_{k\sigma} c_{k\sigma} \tag{5.2}$$

where the c_k and $c^{\dagger}_k$ create and annihilate lattice waves and ϵ_k is a lattice wave energy. (This representation will be used in the definition of the impurity problem below.)

Since we will be working with systems with variable particle numbers, we use grand ensembles. For this purpose it is convenient to define grand Hamiltonians (for all the H in this discussion) as

$$H_G = H - \mu N. \tag{5.3}$$

(We will suppress the subscript G in the following equations. That is $H = H_G$ in the following.) For for the Hubbard model, Eq. (5.1), N in Eq. (5.3) is the total (spin up + spin down)

number operator corresponding to the site centered basis (or the complete band filled basis). However, for the impurity problem μ will be the impurity population chemical potential and $N = n_d = (n_{d\uparrow} + n_{d\downarrow})$ for the impurity site d.

The single particle temperature Green's function [](Fetter and Walecka,p 228) is defined for some set of annihilation and creation operators a_α and $a^\dagger_\alpha$ as,

$$G^\sigma_{\alpha\beta}(\tau,\tau') = \mathrm{Tr}\Big[\rho_G\ T_\tau[a_{\alpha,\sigma}(\tau)a^\dagger_{\beta,\sigma}(\tau')]\Big], \tag{5.4}$$

where the grand ensemble is given by,

$$\rho_G = \frac{e^{-\beta H}}{\mathrm{Tr}\ e^{-\beta H}} = \frac{e^{-\beta H}}{Z}. \tag{5.5}$$

Here $\beta = \frac{1}{kT}$ and Z is the partition function in the grand ensemble $Z = \mathrm{Tr}\, e^{-\beta H}$. $c_i(\tau)$ and $c^\dagger_i(\tau)$ are annihilation and creation operators (defined at this point for an arbitrary single particle Hamiltonian) and T_τ is the time ordering operator [](FW P228). The operators $a_\alpha(\tau)$ and $a^\dagger_\beta(\tau)$ are defined in the imaginary time Heisenberg representation as, (τ *may be called the imaginary time variable*)

$$a_\alpha(\tau) = e^{H\tau} a_\alpha\ e^{-H\tau} \tag{5.6}$$

and

$$a^\dagger_\beta(\tau) = e^{H\tau} a^\dagger_\beta e^{-H\tau} \tag{5.7}$$

The self consistent DMFT cycles illustrated in Figures 5.2 and 5.3 define Anderson impurity models (AIM) consistent with the two methods we discuss below and the lattice model for the problem, Eq. (5.1) . The Hamiltonian for the AIM model in the grand canonical ensemble is given by (this H_{AIM} will be slightly different in the ED model, see below),

$$H_{\mathrm{AIM}} = H'_{\mathrm{AIM}} - \mu N = H_0 + H_{\mathrm{int}} - \mu(n_{d\uparrow} + n_{d\downarrow}), \tag{5.8}$$

where

$$H_0 = \epsilon_d \sum_{\sigma} d^{\dagger}_{\sigma} d_{\sigma} + \sum_{k,\sigma}^{n_s} \epsilon_k c^{\dagger}_{k\sigma} c_{k\sigma} + \sum_{k,\sigma}^{n_s} (V_k c^{\dagger}_{k\sigma} d_{\sigma} + \mathrm{H.c.}) \tag{5.9}$$

and

$$H_{\mathrm{int}} = U n_{d\uparrow} n_{d\downarrow}. \tag{5.10}$$

The operators $c_k / c^{\dagger}_k$ annihilate/create, electrons in lattice waves and are defined by the H_{Lattice}, as in Eqs. (5.1) and (5.2). The d_{σ} and $d^{\dagger}_{\sigma}$ operators create and annihilate orbital occupation on the d impurity site in the AIM and in H_{Lattice} . All lattice sites have the same single localized d orbital as in Eq.(5.1). However one site (as in Fig. (5.1)) is selected as the "impurity site" with site energy ϵ_d (see Figure (1)). (ϵ_d is included in Eq. (5.9) to show the relation to the usual Anderson impurity model and will be set to zero (the lattice site energy) in the calculations below.) The $V_{k,d}$s represent the interaction of the lattice wave k with the d selected "impurity" orbital and are determined in the self consistent iteration as discussed below. In Eq.(5.10) The nonlinear H_{int} interaction represents the on site interaction created by double occupancy. Because of the strong interaction of the lattice sites with the impurity orbitals and the high energy cost of double occupancy, the electronic structure problem defined by Eq. (5.8-5.10) must be solved with very high level numerical method. Lieb has shown that for the one dimensional single band Hubbard model at half-filling $\mu = \frac{U}{2}$. In the following we will emphasis this choice of μ. The impurity Hamiltonian may be partitioned as,

$$H_{\mathrm{AIM}} = \underbrace{(\epsilon_d - \mu) \sum_{\sigma} d^{\dagger}_{\sigma} d_{\sigma} + \sum_{k,\sigma}^{n_s} \epsilon_k c^{\dagger}_{k\sigma} c_{k\sigma} + \sum_{k,\sigma}^{n_s} (V_k c^{\dagger}_{k\sigma} d_{\sigma} + \mathrm{H.c.})}_{H^0_{\mathrm{AIM}} = H_0} + \underbrace{U n_{d\uparrow} n_{d\downarrow}}_{H^i_{\mathrm{AIM}} = H_{\mathrm{int}}} \tag{5.11}$$

It is shown in Appendix H that the Green's function for the independent particle part of this Hamiltonian, $G^0_{dd}(i\omega)$ is given by

$$G^0_{dd}(i\omega) = \left(i\omega - \epsilon_d + \mu - \sum_k^{n_s} \frac{V_k^2}{i\omega - \epsilon_k}\right)^{-1} \tag{5.12}$$

In DMFT the impurity is one of the d centers. Therefore $\epsilon_d = 0$ as for all the sites in H_{Lattice}. The effective potential on the impurity $\sum_k^{n_s} \frac{V_k^2}{i\omega - \epsilon_k}$ is sometimes called the hybridization or Weiss potential.

5.3 The Exact Diagonalization Impurity Solver (ED)

In the DMFT/ED method the the local Green's function for of an Anderson impurity model $G^{\text{AIM}}_{dd}(i\omega)$ Eq. (5.4) is self consistently made equal to the local Green's function, $G_{dd}(i\omega)$, for the lattice Hubbard model. In ED the treatment of the band (bath) interactions in the Anderson impurity in ED is slightly different from the (more general) standard impurity model given in Eq. (**??**) in that the number of band states interacting with the d impurity is limited to a small number of states. Thus allowing an exact diagonalization of the impurity Hamiltonian, but significantly limiting the number of band states (the representation of the lattice band) that can be included. The band energies ϵ_k and V_k for these few states are optimized by a self consistent step (see Fig. (5.2))[28]. In ED with the eigenvalue problem with the Hubbard electro-electron interaction directly solved for the ground state by diagonalization in the full independent particle basis of the Hamiltonian, the zero temperature Green's function calculated by Lanzcos method. This algorithm is described in the following.

The ED Hamiltonian is given by ,

$$H_{\text{AIM}} = U n_{d\uparrow} n_{d\downarrow} - \mu(n_{d\uparrow} + n_{d\downarrow}) + \sum_{i,\sigma}^{n_{\text{ed}}} \epsilon_i c^\dagger_{i\sigma} c_{i\sigma} + \sum_{i,\sigma}^{n_{\text{ed}}} (V_i c^\dagger_{i\sigma} d_\sigma + \text{H.c.}). \tag{5.13}$$

In this H the interactions of the lattice band with the impurity are approximated by the V_i, and the $\epsilon_{i,\sigma}$ terms. Because of the very large size of a complete basis for the H in Eq. (**??**) the number of these terms is quite small (<20). At half-filling $\mu = \frac{U}{2}$ the Lattice Hamiltonian, Eq. (5.1) in grand canonical ensemble is now given by

$$\begin{aligned} H_{\text{Lattice}} &= -\sum_{<ij>,\sigma}^{n_s} (t_{ij}^{n_s} c_{i\sigma}^{\dagger} c_{j\sigma} + \text{H.c.}) + U\sum_{i}^{n_s} n_{i\uparrow} n_{i\downarrow} - \mu\sum_{i}^{n_s}(n_{i\uparrow} + n_{i\downarrow}) \\ &= -\sum_{<ij>,\sigma}^{n_s} (\frac{1}{\sqrt{2z}} c_{i\sigma}^{\dagger} c_{j\sigma} + \text{H.c.}) + U\sum_{i}^{n_s} n_{i\uparrow} n_{i\downarrow} - \mu\sum_{i}^{n_s}(n_{i\uparrow} + n_{i\downarrow}). \end{aligned} \tag{5.14}$$

The impurity Hamiltonian is,

$$H_{\text{AIM}} = U\Big(n_{d\uparrow} n_{d\downarrow} - \frac{n_{d\uparrow} + n_{d\downarrow}}{2}\Big) + \sum_{i,\sigma}^{n_{\text{ed}}} \epsilon_i c_{i\sigma}^{\dagger} c_{i\sigma} + \sum_{i,\sigma}^{n_{\text{ed}}} (V_i c_{i\sigma}^{\dagger} d_{\sigma} + \text{H.c.}). \tag{5.15}$$

In the following the Green's function of the impurity at zero temperature is computed by exact diagonalization of H_{AIM} and Lanczos Green's function algorithm.

The iteration that enforces equality between the d site lattice Green's function and the d site impurity is illustrated in Fig. (5.2).

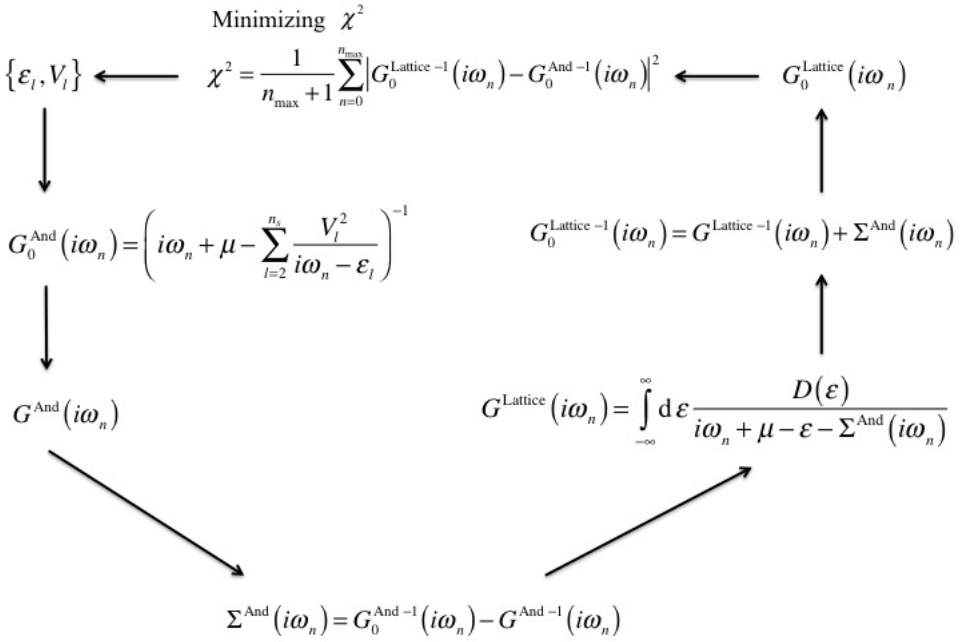


Figure 5.2: DMFT cycle for the Exact Diagonalization (ED) impurity solver.

We start by obtaining the zero temperature Green's function (for the ED Hamiltonian, Eq. (**??**)) from the finite-temperature Green's function, Eq. (5.4) as,

$$G_{ij}(\omega) = \frac{1}{\sum_\mu e^{-\beta E_\mu}} \sum_{\mu,\nu} \frac{\langle \nu | c_i | \mu \rangle \langle \mu | c_j^\dagger | \nu \rangle}{\omega + E_\nu - E_\mu + i\eta} \left(e^{-\beta E_\mu} + e^{-\beta E_\nu} \right). \tag{5.16}$$

where we have expanded in a complete set of kets for the appropriate Hamiltonian, $H|\mu\rangle = E_\mu |\mu\rangle$. Regroup the terms

$$G_{ij}(\omega) = \frac{1}{Z} \sum_{\mu,\nu} \frac{\langle \mu | c_j^\dagger | \nu \rangle \langle \nu | c_i | \mu \rangle}{\omega + E_\nu - E_\mu + i\eta} e^{-\beta E_\mu} + \frac{1}{Z} \sum_{\mu,\nu} \frac{\langle \nu | c_i | \mu \rangle \langle \mu | c_j^\dagger | \nu \rangle}{\omega + E_\nu - E_\mu + i\eta} e^{-\beta E_\nu} \tag{5.17}$$

where $Z = \sum_\mu e^{-\beta E_\mu}$.

Take $\beta \to \infty$ after shift of $E \to (E - E_0)$

$$G_{ij}(\omega) = \sum_{\nu} \left(\frac{\langle 0| c_j^\dagger |\nu\rangle \langle \nu| c_i |0\rangle}{\omega + E_\nu + i\eta} + \frac{\langle 0| c_i |\nu\rangle \langle \nu| c_j^\dagger |0\rangle}{\omega - E_\nu + i\eta} \right). \tag{5.18}$$

Replace eigenvalues E_ν with Hamiltonian $\hat{H}$. The first term becomes

$$\begin{aligned} \sum_{\nu} \frac{\langle 0| c_j^\dagger |\nu\rangle \langle \nu| c_i |0\rangle}{\omega + E_\nu + i\eta} &= \sum_{\nu} \langle 0| c_j^\dagger (\hat{H} + \omega + i\eta)^{-1} |\nu\rangle \langle \nu| c_i |0\rangle \\ &= \langle 0| c_j^\dagger (\hat{H} + \omega + i\eta)^{-1} \sum_{\nu} |\nu\rangle \langle \nu| c_i |0\rangle = \langle 0| c_j^\dagger \frac{1}{\omega + \hat{H} + i\eta} c_i |0\rangle . \end{aligned} \tag{5.19}$$

The second term can be written in the similar way

$$\sum_{\nu} \frac{\langle 0| c_i |\nu\rangle \langle \nu| c_j^\dagger |0\rangle}{\omega - E_\nu + i\eta} = \langle 0| c_i \frac{1}{\omega - \hat{H} + i\eta} c_j^\dagger |0\rangle . \tag{5.20}$$

The diagonal terms are expressed as

$$G(\omega) = \langle 0| c^\dagger \frac{1}{\omega + \hat{H} + i\eta} c |0\rangle + \langle 0| c \frac{1}{\omega - \hat{H} + i\eta} c^\dagger |0\rangle . \tag{5.21}$$

Let's consider the first term. Choose the initial vector as

$$|\psi_0\rangle = \frac{c^\dagger |0\rangle}{\sqrt{\langle 0| c c^\dagger |0\rangle}} \tag{5.22}$$

and build Lanczos basis

$$|\psi_{k+1}\rangle = \hat{H} |\psi_k\rangle - a_k |\psi_k\rangle - b_k^2 |\psi_{k-1}\rangle \tag{5.23}$$

where

$$a_k = \frac{\langle \psi_k | \hat{H} | \psi_k \rangle}{\langle \psi_k | \psi_k \rangle}, \tag{5.24}$$

and

$$b_k^2 = \frac{\langle \psi_k | \psi_k \rangle}{\langle \psi_{k-1} | \psi_{k-1} \rangle} \tag{5.25}$$

with $b_0^2 \equiv 0$ and $|\psi_{-1}\rangle \equiv 0$.

To understand this choice let's consider the identity

$$\sum_n (z - \hat{H})_{mn} (z - \hat{H})^{-1}_{np} = \delta_{mp}. \tag{5.26}$$

which becomes system of linear equations with $p = 0$

$$\sum_n (z - \hat{H})_{mn} (z - \hat{H})^{-1}_{n0} = \sum_n (z - \hat{H})_{mn} x_n = \delta_{m0}. \tag{5.27}$$

The first component of vector $\vec{x}$ is

$$x_0 = (z - \hat{H})^{-1}_{00} = \langle \psi_0 | \frac{1}{z - \hat{H}} | \psi_0 \rangle . \tag{5.28}$$

Cramer's rule is used to calculate x_0

$$x_0 = \frac{\| B \|_0}{z - \hat{H}} \tag{5.29}$$

where

$$z-\hat{H}=\begin{pmatrix} z-a_0 & -b1 & 0 & 0 & \cdots \\ -b_1 & z-a_1 & -b_2 & 0 & \cdots \\ 0 & -b_2 & z-a_3 & -b_3 & \cdots \\ \vdots & \vdots & \vdots & \vdots & \vdots \end{pmatrix} \tag{5.30}$$

and

$$B_0=\begin{pmatrix} 1 & -b1 & 0 & 0 & \cdots \\ 0 & z-a_1 & -b_2 & 0 & \cdots \\ 0 & -b_2 & z-a_3 & -b_3 & \cdots \\ \vdots & \vdots & \vdots & \vdots & \vdots \end{pmatrix}. \tag{5.31}$$

Introducing D_i as matrices with excluded $1\cdots$ i-rows and columns from $(z-\hat{H})$ we get

$$\left\| z-\hat{H} \right\| = (z-a_0)\left\| D_1 \right\| - b_1^2 \left\| D_2 \right\| \tag{5.32}$$

and

$$\left\| B_0 \right\| = \left\| D_1 \right\|. \tag{5.33}$$

Hence x_0 is evaluated as

$$x_0 = \frac{1}{z-a_0-b_1^2\dfrac{\left\| D_2 \right\|}{\left\| D_1 \right\|}}. \tag{5.34}$$

The ratio determinants in denominator in the previous equation is calculated in the similar way

$$\frac{\|D_2\|}{\|D_1\|} = \frac{1}{z - a_1 - b_2^2 \dfrac{\|D_3\|}{\|D_2\|}}. \tag{5.35}$$

Therefore

$$\langle\psi_0| \frac{1}{z - \hat{H}} |\psi_0\rangle = \cfrac{1}{z - a_0^> - \cfrac{b_1^{>2}}{z - a_1^> - \cfrac{b_2^{>2}}{z - a_2^> - \cdots}}} \tag{5.36}$$

and

$$\langle\psi_0| \frac{1}{z + \hat{H}} |\psi_0\rangle = \cfrac{1}{z + a_0^< - \cfrac{b_1^{<2}}{z + a_1^< - \cfrac{b_2^{<2}}{z + a_2^< - \cdots}}}, \tag{5.37}$$

where the coefficients $a_i^>$, $b_i^{>2}$ and $a_i^<$, $b_i^{<2}$ are obtained in Lanczos procedure with $c^\dagger|0\rangle$ and $c|0\rangle$ as the initial vectors respectively.

Finally

$$
\begin{aligned}
G^{\mathrm{AIM}}(i\omega_n) &= \cfrac{\langle 0|\, d\, d^{\dagger}\, |0\rangle}{i\omega_n - a_0^{>} - \cfrac{b_1^{>2}}{i\omega_n - a_1^{>} - \cfrac{b_2^{>2}}{i\omega_n - a_2^{>} - \ldots}}} \\
&+ \cfrac{\langle 0|\, d^{\dagger}\, d\, |0\rangle}{i\omega_n + a_0^{>} - \cfrac{b_1^{>2}}{i\omega_n + a_1^{>} - \cfrac{b_2^{>2}}{i\omega_n + a_2^{>} - \ldots}}}.
\end{aligned}
\tag{5.38}
$$

where ω_n is the Matsubara frequency

$$
\omega_n = \frac{(2n+1)\pi}{\beta}. \tag{5.39}
$$

The noninteracting Green's function G_0^{AIM} of the impurity is given by

$$
G_0^{\mathrm{AIM}}(i\omega_n) = (i\omega_n + \mu - \sum_{i=2}^{n_s} \frac{V_i^2}{i\omega_n - \epsilon_i})^{-1}. \tag{5.40}
$$

Since the local Green's function calculated by Hilbert transform has an analytic form, the Weiss function G_0 and the local Green's function of the lattice G^{Lat} are connected by a self-consistency relation which reads

$$
\begin{aligned}
G_0^{\mathrm{Lat}-1}(i\omega_n) &= i\omega_n + \mu - t^2 G^{\mathrm{Lat}}(i\omega_n) \\
&= i\omega_n + \mu - \frac{G^{\mathrm{Lat}}(i\omega_n)}{2}
\end{aligned}
\tag{5.41}
$$

where

$$
t = \sqrt{z}\, t_{ij} = \frac{1}{\sqrt{2}}. \tag{5.42}
$$

It is assumed that the local Green's function G^{Lat} and the Weiss field G_0 can be approximated by the impurity Green's function G^{AIM} and noninteracting impurity Green's function G_0^{AIM} respectively given a finite number of degrees of freedom of the Anderson model,

$$G^{\mathrm{Lat}}(i\omega_n) \approx G^{\mathrm{AIM}}(i\omega_n) \tag{5.43}$$

and

$$G_0^{\mathrm{Lat}}(i\omega_n) \approx G_0^{\mathrm{AIM}}(i\omega_n) \tag{5.44}$$

Therefore the self-consistency relation in Eq. (5.41) is rewritten by

$$G_0^{\mathrm{Lat}-1}(i\omega_n) = i\omega_n + \mu - \frac{G^{\mathrm{AIM}}(i\omega_n)}{2}. \tag{5.45}$$

In the calculation, the noninteracting Green's function of the impurity G_0^{AIM} is fitted to the Weiss function G_0 is in order to find optimized parameters ϵ_i and V_i. This can be cast into a minimization problem with the cost function

$$\chi^2 = \frac{1}{n_{\max}+1} \sum_{n=0}^{n_{\max}} |G_0^{-1}(i\omega_n) - G_0^{-1\mathrm{AIM}}(i\omega_n)|^2. \tag{5.46}$$

Hence the procedure of the DMFT calculation goes as follows.

$$\begin{aligned} \{\epsilon_i, V_i\}_{\mathrm{initial}} \quad &\xrightarrow{\text{Eq. (5.40)}} G_0^{\mathrm{AIM}}(i\omega_n) \xrightarrow{\text{Eq. (5.38)}} G^{\mathrm{AIM}}(i\omega_n) \\ &\xrightarrow{\text{Eq. (5.45)}} G_0(i\omega_n) \xrightarrow{\text{Eq. (5.46)}} \{\epsilon_i, V_i\}_{\mathrm{new}} \end{aligned} \tag{5.47}$$

The loop is iterated to convergence.

5.4 The Hirsch-Fye Impurity Solver

The local $d\uparrow d\uparrow$ site Green's function is

$$G_{d\uparrow,d\uparrow}(\tau,\tau) = \mathrm{Tr}\Big[\frac{e^{-\beta H}}{\mathrm{Tr}e^{-\beta H}} T_\tau[c_{d\uparrow}(\tau)c^\dagger_{d\uparrow}(\tau')]\Big] \tag{5.48}$$

In the HF solver the AIM greens function and the local lattice Green's function are set equal according to the cycle in Fig. (5.3) [67]. The Greens function of the AIM, G, is on the right side in Fig. (5.3). The local Green's function of the lattice, $\bar{G}$ is produced by the integral at the bottom of the figure (a Hilbert transformation, integral over the lattice independent particle wave vectors, $\vec{k}$s). (The self energy Σ is assumed to be only a function of the energy (ω) making the Hilbert transformation tractable.) After getting $G(\tau)$, we use Fourier transform to calculate $G(i\omega)$. The major cost in the DMFT calculation is the calculation of the Green's function (self energy, Impurity Solver, Fig. (5.1)) of the Anderson impurity model (AIM).

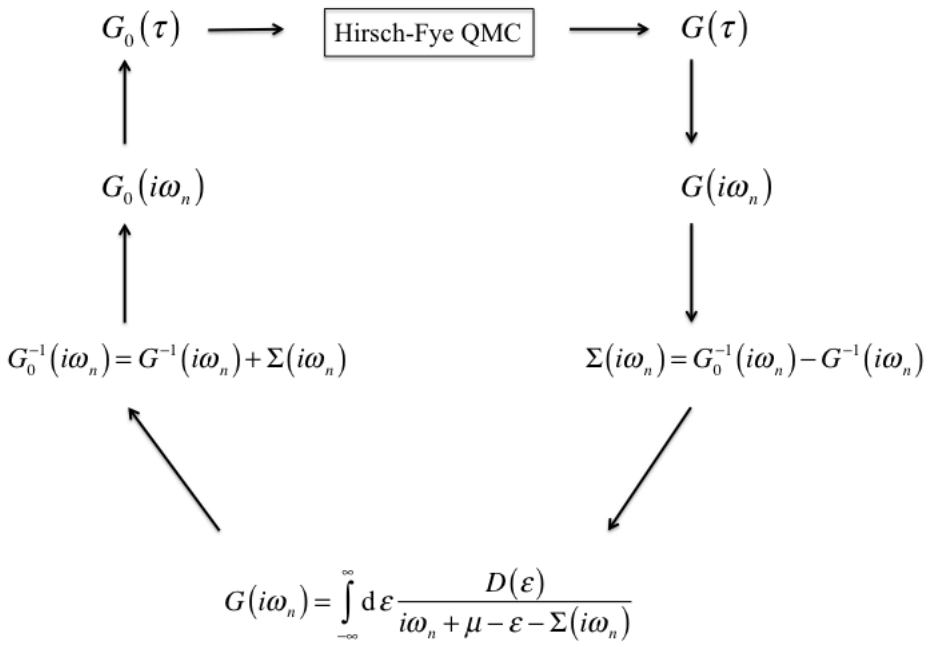


Figure 5.3: DMFT cycle for the Hirsch-Fye QMC impurity solver

We begin by developing a computational scheme for the partition function,

$$Z = \mathbf{Tr}\left(e^{-\beta H}\right). \tag{5.49}$$

In the following we are interested in the Anderson model solution. However, we will suppress the AIM subscript on the Hamiltonian. To evaluate the Tr we divide the sum Tr over β in Z into small steps, $\Delta\tau$, where $\Delta\tau$ is an imaginary time step, $\Delta\tau = \dfrac{\beta}{M}$ and M is the number of τ slices with total length from $\tau = 0$ to $\tau = M\Delta\tau$. H commutes with itself [](Messiah p442) so,

$$e^{-\beta H} = e^{-\Delta\tau H} e^{-\Delta\tau H} \cdots e^{-\Delta\tau H} \tag{5.50}$$

Using the Trotter-Suzuki breakup the single particle and two particle parts of the Hamiltonian may be separated as,

$$e^{-\Delta\tau(H_0+H_{\text{int}})} = e^{-\Delta\tau H_0} e^{-\Delta\tau H_{\text{int}}} + O(\Delta\tau^2[H_0, H_{\text{int}}]) \tag{5.51}$$

the partition function Z can then be approximated as,

$$Z = \mathbf{Tr}\left(e^{-\beta H}\right) = \mathbf{Tr}\left(\prod_{i=M}^{1} e^{-\Delta\tau(H_0+H_{\text{int}})}\right) \approx \mathbf{Tr}\left(\prod_{i=M}^{1} e^{-\Delta\tau H_0} e^{-\Delta\tau H_{\text{int}}}\right) + O(\Delta\tau^2 U). \tag{5.52}$$

The nonlinear operator H_{int} is still difficult to calculate. The discrete Hubbard-Stratonovich decomposition of the interaction term, H_{int} in the exponential reduces the nonlinear contributions to linear operators as follows [103],

$$
\begin{aligned}
e^{-\Delta\tau H_{\rm int}} &= e^{-\Delta\tau U[n_{d\uparrow}n_{d\downarrow}-\frac{1}{2}(n_{d\uparrow}+n_{d\downarrow})]} = \frac{1}{2}\sum_{s_i=\pm 1} e^{-\lambda s_i(n_{d\uparrow}-n_{d\downarrow})} \\
&= \frac{1}{2}\sum_{s_i=\pm 1} e^{-\sum_\sigma \lambda s_i \gamma_\sigma n_{d\sigma}} = \frac{1}{2}\sum_{s_i=\pm 1}\prod_\sigma e^{-\lambda s_i \gamma_\sigma n_{d\sigma}}, \qquad (5.53)
\end{aligned}
$$

In Eq. (5.53) a discrete variable, $s_i = \pm 1$ (an Ising like spin variable), has been introduced for each layer i. γ_σ is defined by $\gamma_+ = 1$ (spin up) and $\gamma_- = -1$ (spin down). λ is given by

$$
\cosh(\lambda) = \exp(\Delta\tau\frac{U}{2}), \qquad (5.54)
$$

leading to,

$$
\lambda = \exp(\Delta\tau\frac{U}{2}) + \sqrt{\exp(\Delta\tau U) - 1}. \qquad (5.55)
$$

To proceed we define a diagonal quadratic operator $\mathscr{V}_\sigma^{(l)}$, which depends on the Ising spin configuration on slice l as,

$$
\mathscr{V}_\sigma(i) = \sum_{jk}(\mathbb{V}_\sigma(i))_{jk} c^\dagger_{j\sigma} c_{k\sigma} \qquad (5.56)
$$

where

$$
\mathbb{V}_\sigma(i) = \begin{pmatrix} \lambda s_i \gamma_\sigma & 0 & \cdots & 0 \\ 0 & 0 & \cdots & 0 \\ \vdots & \vdots & \ddots & \vdots \\ 0 & 0 & \cdots & 0, \end{pmatrix} \qquad (5.57)
$$

where we have reserved position 1 of the matrix representation for the impurity d_σ orbital.

Thus

$$e^{-\Delta\tau H_{\rm int}} = \frac{1}{2}\sum_{s_i,\sigma} e^{-\mathscr{V}_\sigma(i)} \tag{5.58}$$

Now the partition function becomes

$$\begin{aligned} Z &= \mathbf{Tr}\left(\prod_{i=M}^{1}\sum_{s_i}\frac{1}{2}\prod_{\sigma} e^{-\Delta\tau H_{0\sigma}} e^{-\mathscr{V}_\sigma(i)}\right) \\ &= \frac{1}{2^M}\sum_{\{s\}}\mathbf{Tr}\left(\prod_{i=M}^{1} e^{-\Delta\tau H_{0\uparrow}} e^{-\mathscr{V}_\uparrow(i)} e^{-\Delta\tau H_{0\downarrow}} e^{-\mathscr{V}_\downarrow(i)}\right) \\ &= \frac{1}{2^M}\sum_{\{s\}}\mathbf{Tr}\left(\prod_{i=M}^{1} e^{-\Delta\tau H_{0\uparrow}} e^{-\mathscr{V}_\uparrow(i)}\right)\mathbf{Tr}\left(\prod_{i=M}^{1} e^{-\Delta\tau H_{0\downarrow}} e^{-\mathscr{V}_\downarrow(i)}\right) \end{aligned} \tag{5.59}$$

Note that $\{s\}$ is one set of s_l for the layers where each layer is indexed by supperscript l, that is, $\{s\} = \{s_1, \cdots, s_L\}$. In total, there are 2^L possible sets of $\{s\}$. (The difficult step in the problem is now how to calculate the $\sum_{\{s_i\}}$ in Eq. (5.59). This will become a Metropolis sampling problem.)

Since the H_0 term has the form (the spin is omitted in the following derivations)

$$H_0 = \sum_{jk}(\mathbb{H}_0)_{jk} c_j^\dagger c_k, \tag{5.60}$$

from Eq. (5.59) the partition function $Z_{\{s\}}$ at fixed Ising configuration $\{s_l\}$ becomes

$$Z(\{s\}) = \frac{1}{2^M}\mathrm{Tr}\prod_{i=M}^{1}\exp(-\Delta\tau(\sum_{jk} c_j^\dagger \mathbb{H}_{jk}(i) c_k)) \tag{5.61}$$

where

$$\mathbb{H}_{jk}(i) = (\mathbb{H}_0)_{jk} - \frac{\lambda}{\Delta\tau} s_i \gamma \delta_{j=k=1}. \tag{5.62}$$

and

$$Z = \sum_{\{s\}} Z(\{s\}). \tag{5.63}$$

where

$$\begin{aligned} Z(\{s\}) &= \frac{1}{2^M}\mathbf{det}\Big(\mathbb{I} + \prod_{i=M}^{1} e^{-\Delta\tau\mathbb{H}_{0\uparrow}} e^{-\mathbb{V}_{\uparrow}(i)}\Big)\mathbf{det}\Big(\mathbb{I} + \prod_{i=M}^{1} e^{-\Delta\tau\mathbb{H}_{0\downarrow}} e^{-\mathbb{V}_{\downarrow}(i)}\Big) \\ &= \frac{1}{2^M}\mathbf{det}\Big(\mathbb{I} + \prod_{i=M}^{1} \mathbb{M}_{\uparrow}(i)\Big)\mathbf{det}\Big(\mathbb{I} + \prod_{i=M}^{1} \mathbb{M}_{\downarrow}(i)\Big) \end{aligned} \tag{5.64}$$

by defining matrices

$$\mathbb{M}_{\sigma}(i) = e^{-\Delta\tau\mathbb{H}_{0\sigma}} e^{-\mathbb{V}_{\sigma}(i)} \tag{5.65}$$

Z now equals,

$$\begin{aligned} Z &= \frac{1}{2^M}\sum_{\{s\}}\mathbf{det}\Big(\mathbb{I} + \prod_{i=M}^{1} e^{-\Delta\tau\mathbb{H}_{0\uparrow}} e^{-\mathbb{V}_{\uparrow}(i)}\Big)\mathbf{det}\Big(\mathbb{I} + \prod_{i=M}^{1} e^{-\Delta\tau\mathbb{H}_{0\downarrow}} e^{-\mathbb{V}_{\downarrow}(i)}\Big) \\ &= \frac{1}{2^M}\sum_{\{s\}}\mathbf{det}\Big(\mathbb{I} + \prod_{i=M}^{1} \mathbb{M}_{\uparrow}(i)\Big)\mathbf{det}\Big(\mathbb{I} + \prod_{i=M}^{1} \mathbb{M}_{\downarrow}(i)\Big). \end{aligned} \tag{5.66}$$

with the expansion of the **det** in minors this can be written as,

$$\mathbf{det}\Big(\mathbb{I} + \prod_{i=M}^{1} \mathbb{M}_{\sigma}(i)\Big) = \mathbf{det}\mathbb{O}_{\sigma}(\{s\}) \tag{5.67}$$

where

$$\mathbb{O}_\sigma(\{s\}) = \begin{pmatrix} \mathbb{I} & \mathbf{0} & \mathbf{0} & \cdots & \mathbf{0} & \mathbf{0} & \mathbb{M}(1) \\ -\mathbb{M}(M) & \mathbb{I} & \mathbf{0} & \cdots & \mathbf{0} & \mathbf{0} & \mathbf{0} \\ \mathbf{0} & -\mathbb{M}(M-1) & \mathbb{I} & \cdots & \mathbf{0} & \mathbf{0} & \mathbf{0} \\ \vdots & \vdots & \vdots & \ddots & \vdots & \vdots & \vdots \\ \mathbf{0} & \mathbf{0} & \mathbf{0} & \cdots & -\mathbb{M}(3) & \mathbb{I} & \mathbf{0} \\ \mathbf{0} & \mathbf{0} & \mathbf{0} & \cdots & \mathbf{0} & -\mathbb{M}(2) & \mathbb{I} \end{pmatrix}_{n_s M \times n_s M} . \tag{5.68}$$

$\mathbb{O}_\sigma(\{s\})$ is an $M \times M$ matrix of $n_s \times n_s$ matrices, where n_s is the number of sites in the lattice. The partition function is now

$$Z = \frac{1}{2^M} \sum_{\{s\}} \mathbf{det}\mathbb{O}_\uparrow(\{s\}) \mathbf{det}\mathbb{O}_\downarrow(\{s\}) \tag{5.69}$$

Observables A can be calculated for a given Ising spin configuration as $A(\{s_l\})$ by Wick's theorem

$$\begin{aligned} \langle A \rangle &= \frac{1}{2^M} \sum_{\{s\}} A(\{s\}) \frac{\mathbf{det}\mathbb{O}_\uparrow(\{s\}) \mathbf{det}\mathbb{O}_\downarrow(\{s\})}{Z} \\ &= \sum_{\{s\}} A(\{s\}) \frac{Z(\{s\})}{Z} \end{aligned} \tag{5.70}$$

Therefore $\dfrac{Z(\{s\})}{Z}$ may be interpreted as the statistical weight of the Ising spin configuration.

It can be proved that

$$\mathscr{G}_\sigma(\{s\}) = \mathbb{O}_\sigma^{-1}(\{s\})) \tag{5.71}$$

So far these are the general results of determinantal QMC.

Based on the above results Hirsch and Fye pointed out that there exists a Dyson equation which connects Green's function of different Ising configurations $\{s_i\}$ and $\{s'_i\}$. Let $\mathcal{G}_\sigma(\{s'_i\}) = \mathcal{G}'_\sigma$, it's observed that

$$\mathcal{G}_\sigma^{-1} e^{\mathbb{V}_\sigma} - \mathcal{G}_\sigma'^{-1} e^{\mathbb{V}'_\sigma} = e^{\mathbb{V}_\sigma} - e^{\mathbb{V}'_\sigma} \tag{5.72}$$

Rewrite Eq. (5.72) to obtain

$$\mathcal{G}_\sigma'^{-1} - \mathcal{G}_\sigma^{-1} = (\mathbb{I} - \mathcal{G}_\sigma^{-1})(\mathbb{I} - e^{\mathbb{V}_\sigma - \mathbb{V}'_\sigma}) \tag{5.73}$$

or

$$\mathcal{G}'_\sigma - \mathcal{G}_\sigma = (\mathcal{G}_\sigma - \mathbb{I})(\exp(\mathbb{V}_\sigma - \mathbb{V}'_\sigma) - \mathbb{I})\mathcal{G}'_\sigma \tag{5.74}$$

where 1 is an $n_s L \times n_s L$ identity matrix and $\mathscr{V}$ is an $n_s L \times n_s L$ diagonal matrix.

$$(\mathbb{V}_\sigma)_{ij}^{(l_1 l_2)} = \delta_{i,1}\delta_{j,1}\delta_{l_1,l_2}\gamma_\sigma \lambda s_{l_1} \tag{5.75}$$

The presence of the projection operator $\exp(\mathbb{V}'_\sigma - \mathbb{V}_\sigma) - \mathbb{I}$ comes from the possibility of integrating out the conduction band. As a consequence, the Dyson equation Eq. 5.72 directly relates the Green's function on the impurity site one to another. Hence the impurity Green's function also satisfies

$$\mathbb{G}'_\sigma = \mathbb{G}_\sigma + (\mathbb{G}_\sigma - 1)(e^{V_\sigma - V'_\sigma} - 1)\mathbb{G}'_\sigma. \tag{5.76}$$

where 1 is an $M \times M$ identity matrix and V is an $M \times M$ diagonal matrix.

$$(V_\sigma)_{l_1 l_2} = \delta_{l_1 l_2}\gamma_\sigma \lambda s_{l_1}. \tag{5.77}$$

By Eq. (5.76) we can isolate the impurity site and study the impurity Green's function only. Besides, an $L \times L$ matrix for the impurity site is used instead of the original $n_s L \times n_s L$ matrix.

Rearranging Eq. (5.76) we can see that the $\mathbb{G}'$ can be obtained from $\mathbb{G}$ by the following equation

$$\mathbb{G}'_\sigma = \mathbb{A}_\sigma^{-1}\mathbb{G}_\sigma \tag{5.78}$$

where

$$\mathbb{A}_\sigma = \mathbb{I} + (\mathbb{I} - \mathbb{G}_\sigma)\Big[\exp(V_\sigma - V'_\sigma) - \mathbb{I}\Big]. \tag{5.79}$$

Now we consider the single spin flip case, that is, $\{s'_i\} = \{s'_1, s'_2, \cdots, s'_M\}$ differs from $\{s_i\} = \{s_1, s_2, \cdots, s_M\}$ only by the value of a single spin, say s_i. Hence the matrix $e^{V_\sigma - V'_\sigma}$ is

$$e^{V_\sigma - V'_\sigma} = \begin{pmatrix} 1 & 0 & \cdots & 0 \\ \cdots & \cdots & \cdots & \cdots \\ \cdots & e^{\lambda\gamma_\sigma(s_i - s'_i)} & \cdots & \\ \cdots & \cdots & \cdots & \cdots \\ 0 & \cdots & 0 & 1 \end{pmatrix} \tag{5.80}$$

or

$$(e^{V_\sigma - V'_\sigma} - \mathbb{I})_{l_1 l_2} = (e^{\lambda\gamma_\sigma(s_i - s'_i)} - \mathbb{I})\delta_{l_1 = l_2 = l} \tag{5.81}$$

From Eq. (5.81) we can get the elements of $M \times M$ matrix $\mathbb{A}_\sigma$ are

$$(\mathbb{A}_\sigma)_{l_1 l_2} = \delta_{l_1 l_2} + (\delta_{l_1 l} - (\mathbb{G}_\sigma)_{l_1 l})(e^{\lambda \gamma_\sigma (s_i - s_i')} - 1)\delta_{l_2 l} \tag{5.82}$$

or in matrix form (spin neglected)

$$\mathbb{A} = \begin{pmatrix} 1 & 0 & \mathbb{A}_{1l} & 0 & \cdots \\ 0 & 1 & \mathbb{A}_{2l} & \cdots & \cdots \\ \cdots & 0 & \mathbb{A}_{ll} & \cdots & \cdots \\ \cdots & \cdots & \cdots & 1 & 0 \\ \cdots & \cdots & \mathbb{A}_{Ml} & 0 & 1 \end{pmatrix} \tag{5.83}$$

with

$$\mathbf{det}\mathbb{A} = \mathbb{A}_{ll} = 1 + (1 - (\mathbb{G}_\sigma)_{ll})[\exp((V_\sigma)_{ll} - (V_\sigma')_{ll}) - 1]. \tag{5.84}$$

Let $a \equiv e^{\lambda \gamma_\sigma (s_i - s_i')} - 1$. The inversion of matrix $\mathbb{A}$ can be calculated explicitly.

$$(\mathbb{A}_\sigma)^{-1}_{l_1 l_2} = \delta_{l_1 l_2} - \frac{a}{1 + a(1 - (\mathbb{G}_\sigma)_{ll})}(\delta_{l_1 l} - (\mathbb{G}_\sigma)_{l_1 l})\delta_{l_2 l} \tag{5.85}$$

or in matrix form

$$\mathbb{A}^{-1} = \mathbb{I} + \frac{a}{1 + a(1 - \mathbb{G}_{ll})} \begin{pmatrix} 0 & \cdots & \mathbb{G}_{1l} & \cdots & 0 \\ 0 & \cdots & \mathbb{G}_{2l} & \cdots & 0 \\ 0 & \cdots & \cdots & \cdots & 0 \\ 0 & \cdots & \mathbb{G}_{ll} - 1 & \cdots & 0 \\ 0 & \cdots & \cdots & \cdots & 0 \\ 0 & \cdots & \mathbb{G}_{Ml} & \cdots & 0 \end{pmatrix} \tag{5.86}$$

From Eq. (5.78) and (5.85) the elements of Green's function for configuration $\{s'_l\}$ are

$$(\mathbb{G}'_\sigma)_{l_1 l_2} = (\mathbb{G}_\sigma)_{l_1 l_2} + \frac{a}{1 + a(1 - (\mathbb{G}_\sigma)_{ll})}((\mathbb{G}_\sigma)_{l_1 l} - \delta_{l_1 l})(\mathbb{G}_\sigma)_{l l_2} \tag{5.87}$$

Now we can apply Metropolis method to do the Monte Carlo. If the move is "downhill", the probability of state s' is greater than state s and the new configuration is accepted. If the move is "uphill", the move is accepted with a probability

$$\begin{aligned} P(s,s') &= \frac{\rho'}{\rho} = \frac{\mathbf{det}\mathbb{G}_\uparrow \mathbf{det}\mathbb{G}_\downarrow}{\mathbf{det}\mathbb{G}'_\uparrow \mathbf{det}\mathbb{G}'_\downarrow} \\ &= \mathbf{det}\mathbb{A}_\uparrow \mathbf{det}\mathbb{A}_\downarrow = (\mathbb{A}_\uparrow)_{ll}(\mathbb{A}_\downarrow)_{ll} \\ &= [1 + (1 - (\mathbb{G}_\uparrow)_{ll})(e^{(V_\uparrow)_{ll} - (V'_\uparrow)_{ll}} - 1)][1 + (1 - (\mathbb{G}_\downarrow)_{ll})(e^{(V_\downarrow)_{ll} - (V'_\downarrow)_{ll}} - 1)] \\ &= [1 + (1 - (\mathbb{G}_\uparrow)_{ll})(e^{-2\lambda s_l} - 1)][1 + (1 - (\mathbb{G}_\downarrow)_{ll})(e^{2\lambda s_l} - 1)] \end{aligned} \tag{5.88}$$

To accept a move with a probability of Eq. (5.88), a random number ζ is generated uniformly on (0,1) and compared with the probability $P(s,s')$. If it is less than $P(s,s')$ the move is accepted otherwise it is rejected. If a move is rejected, the system remains in state s. The procedure can be summarized that we accept any move with probability $\min(1, \frac{\rho'}{\rho})$.

$$P(s,s') = \begin{cases} 1 & \text{if } \rho' > \rho \\ \dfrac{\rho'}{\rho} & \text{otherwise} \end{cases} \tag{5.89}$$

Once the new Ising spin configuration is accepted, the elements of new Green's function can be calculated according to Eq. (9), (10) and (12) as

$$
\begin{aligned}
(\mathbb{G}'_\sigma)_{l_1 l_2} &= (\mathbb{G}_\sigma)_{l_1 l_2} + ((\mathbb{G}_\sigma)_{l_1 l} - \delta_{l_1 l})(e^{(V_\sigma)_{ll} - (V'_\sigma)_{ll}} - 1)(\mathbb{A}_\sigma)^{-1}_{ll}(\mathbb{G}_\sigma)_{l l_2} \\
&= (\mathbb{G}_\sigma)_{l_1 l_2} + ((\mathbb{G}_\sigma)_{l_1 l} - \delta_{l_1 l}) \frac{e^{-2\lambda\gamma_\sigma s_l} - 1}{1 + (1 - (\mathbb{G}_\sigma)_{ll})[e^{-2\lambda\gamma_\sigma s_l} - 1]} (\mathbb{G}_\sigma)_{l l_2}
\end{aligned}
\tag{5.90}
$$

At last the Green's function on imaginary time axis is estimated by a Monte Carlo average.

$$
\langle G_\sigma(\{s_1, s_2, ..., s_L\})\rangle_{\mathrm{MC}} = \frac{\sum\limits_{\text{accepted}} \mathbb{G}_\sigma(\{s_l\})\mathbf{det}\mathbb{G}_\uparrow(\{s_l\})\mathbf{det}\mathbb{G}_\downarrow(\{s_l\})}{\sum\limits_{\text{accepted}} \mathbf{det}\mathbb{G}_\uparrow(\{s_l\})\mathbf{det}\mathbb{G}_\downarrow(\{s_l\})}. \tag{5.91}
$$

With the Hirsch-Fye solver, the self-consistent iteration goes as

$$
G_0(\tau) \rightarrow \left\{ \begin{array}{c} \xrightarrow{\text{Hirsch-Fye}} G(\tau) \xrightarrow{\text{FT}} G(i\omega) \\ \xrightarrow{\text{FT}} G_0(i\omega) \end{array} \right\} \rightarrow \Sigma(i\omega) \xrightarrow{\text{HT}} G^{\text{new}}(i\omega) \rightarrow G_0^{\text{new}}(i\omega) \xrightarrow{\text{IFT}} G_0^{\text{new}}(\tau). \tag{5.92}
$$

The explicit flow of the algorithm goes as,

1. Input non-interacting Green's function (initial guess) $G_0(\tau)$. We have L $G_0(\tau)s$ from $G_0(\tau_1)$ to $G_0(\tau_L)$. Make a $L \times L$ matrix out of G_0 by

$$
(\mathbb{G}_0)_{l_1 l_2} = G_0(\tau_{l_1} - \tau_{l_2}). \tag{5.93}
$$

The antiperiodicity is used as

$$
G_0(\tau + \beta) = -G_0(\tau). \tag{5.94}
$$

2. Choose starting Ising configuration $\{s\}$.

3. Calculate $\mathbb{G}_{l_1 l_2}$ from $(\mathbb{G}_0)_{l_1 l_2}$:

$$(\mathbb{G}_\sigma)_{l_1 l_2} = (\mathbb{A}_\sigma)^{-1}_{l_1 l_2} (\mathbb{G}_{0\sigma})_{l_1 l_2} \tag{5.95}$$

with

$$(\mathbb{A}_\sigma)_{l_1 l_2} = \delta_{l_1 l_2} e^{\lambda \gamma_\sigma s_{l_2}} - (\mathbb{G}_{0\sigma})_{l_1 l_2} (e^{\lambda \gamma_\sigma s_{l_2}} - 1). \tag{5.96}$$

Here we can think that the Ising configuration for G_0 is $(0, 0, ..., 0)$.

4. Repeat these steps until enough measurements are collected.

4.1. Choose one time slice l randomly and accept the spin flip at l with transition probability according to

$$P(s \to s') = \min[\frac{\rho(\{s'\})}{\rho(\{s\})}, 1] \tag{5.97}$$

with

$$\rho(\{s\}) = \mathbf{det}[\mathbb{G}^{-1}_\uparrow(\{s\})]\mathbf{det}[\mathbb{G}^{-1}_\downarrow(\{s\})] \tag{5.98}$$

and

$$\frac{\rho(\{s'\})}{\rho(\{s\})} = [1 + (1 - (\mathbb{G}_\uparrow)_{ll})(e^{\lambda(s'_l - s_l)} - 1)][1 + (1 - (\mathbb{G}_\downarrow)_{ll})(e^{-\lambda(s'_l - s_l)} - 1)] \tag{5.99}$$

4.2 Calculate new $\mathbb{G}'$ from $\mathbb{G}$ by

$$(\mathbb{G}'_\sigma)_{l_1 l_2} = (\mathbb{G}_\sigma)_{l_1 l_2} + \frac{e^{\lambda\sigma(s'_l - s_l)} - 1}{1 + (1 - (\mathbb{G}_\sigma)_{ll})(e^{\lambda\sigma(s'_l - s_l)} - 1)}((\mathbb{G}_\sigma)_{l_1 l} - \delta_{l_1 l})(\mathbb{G}_\sigma)_{l l_2} \tag{5.100}$$

4.3 After the number of steps exceeds the number of warmup steps, that is when the distribution reaches equilibrium, start collecting measurements.

4.4 Save all the accepted measurements.

5. Calculate the average of $\mathbb{G}_{l_1 l_2}$

$$(\mathbb{G}_\sigma)_{l_1 l_2} = \frac{\sum\limits_{\text{accepted}} \mathbb{G}_\sigma(\{s_l\})\mathbf{det}\mathbb{G}_\uparrow(\{s_l\})\mathbf{det}\mathbb{G}_\downarrow(\{s_l\})}{\sum\limits_{\text{accepted}} \mathbf{det}\mathbb{G}_\uparrow(\{s_l\})\mathbf{det}\mathbb{G}_\downarrow(\{s_l\})}. \tag{5.101}$$

The distribution function is

$$P(\{s\}) = \frac{\mathbf{det}\mathbb{G}_\uparrow(\{s_l\})\mathbf{det}\mathbb{G}_\downarrow(\{s_l\})}{\sum\limits_{\text{accepted}} \mathbf{det}\mathbb{G}_\uparrow(\{s_l\})\mathbf{det}\mathbb{G}_\downarrow(\{s_l\})}. \tag{5.102}$$

6. Calculate $G(\tau)$ out of $L \times L$ matrix $\mathbb{G}_{l_1 l_2}$.

5.5 Results and Discussion

4.1. Energy

Within the DMFT, the energy per lattice site is given as [55, 49]

$$E = \lim_{\eta\to 0^+} T\sum_{n,\sigma}\int_{-\infty}^{\infty} d\epsilon \frac{e^{i\omega_n\eta}\epsilon\rho(\epsilon)}{i\omega_n - \epsilon + \mu - \Sigma_\sigma(i\omega_n)} + \frac{1}{2}T\sum_{n,\sigma} e^{i\omega_n\eta}\Sigma_\sigma(i\omega_n)G_\sigma(i\omega_n) \tag{5.103}$$

For the kinetic energy [12],

$$\begin{aligned} E_{\text{kin}} &= \lim_{\eta\to 0^+} 2T\sum_{n=-\infty}^{\infty} e^{i\omega_n\eta}\int_{-\infty}^{\infty} d\epsilon \frac{\epsilon\rho(\epsilon)}{i\omega_n - \epsilon + \mu - \Sigma_\sigma(i\omega_n)} \\ &= 2\int_{-\infty}^{\infty} d\epsilon \frac{\epsilon\rho(\epsilon)}{e^{\beta(\epsilon-\mu)}+1} + 2T\sum_{n=-\infty}^{\infty}\int_{-\infty}^{\infty} d\epsilon\epsilon\rho(\epsilon)(G_\epsilon(i\omega_n) - G^0_\epsilon(i\omega_n)) \\ &\approx 2\int_{-\infty}^{\infty} d\epsilon \frac{\epsilon\rho(\epsilon)}{e^{\beta(\epsilon-\mu)}+1} + 4T\sum_{n=1}^{n_{\max}}\int_{-\infty}^{\infty} d\epsilon\epsilon\rho(\epsilon)(G_\epsilon(i\omega_n) - G^0_\epsilon(i\omega_n)), \end{aligned} \tag{5.104}$$

where the paramagnetic case is assumed. The interacting and noninteracting "momentum-dependent" Green's functions are

$$G_\epsilon(i\omega_n) = \frac{1}{i\omega_n - \epsilon + \mu - \Sigma_\sigma(i\omega_n)} \tag{5.105}$$

and

$$G^0_\epsilon(i\omega_n) = \frac{1}{i\omega_n - \epsilon + \mu}. \tag{5.106}$$

The potential energy reads

$$E_{\text{pot}} = UD \tag{5.107}$$

where D is the double occupancy

$$D = \langle n_\uparrow n_\downarrow \rangle = \frac{T}{U} \sum_n e^{i\omega_n \eta} \Sigma_\sigma(i\omega_n) G_\sigma(i\omega_n) \tag{5.108}$$

The energies calculated from exact diagonalization and Hirsch-Fye QMC are shown below

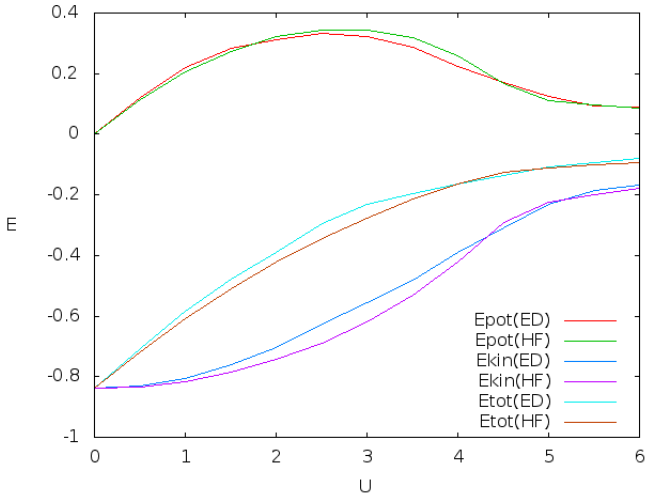


Figure 5.4: Energy for the Bethe lattice (bandwidth W=4) at $T = 0.1$ in the paramagnetic case

From the Fig. 5.4, for small U, the kinetic energy increases quadratically while the potential energy and the total energy increase linearly. A maximum is reached around $U = 3$ for the potential energy. When U is near 4.5, the metal-insulator transition appears. As U gets larger, the energy curves converge, indicating that the system becomes an insulator.

4.2 Spectral density

The spectral density can be calculated by

$$\rho(\omega) = -\frac{1}{\pi} \mathrm{Im} G(\omega) \tag{5.109}$$

where $G(\omega)$ on the real axis is obtained by analytical continuation from the Green's func-

tion along the discrete Matsubara frequency plane. In ED calculation, $G(\omega)$ can be computed by

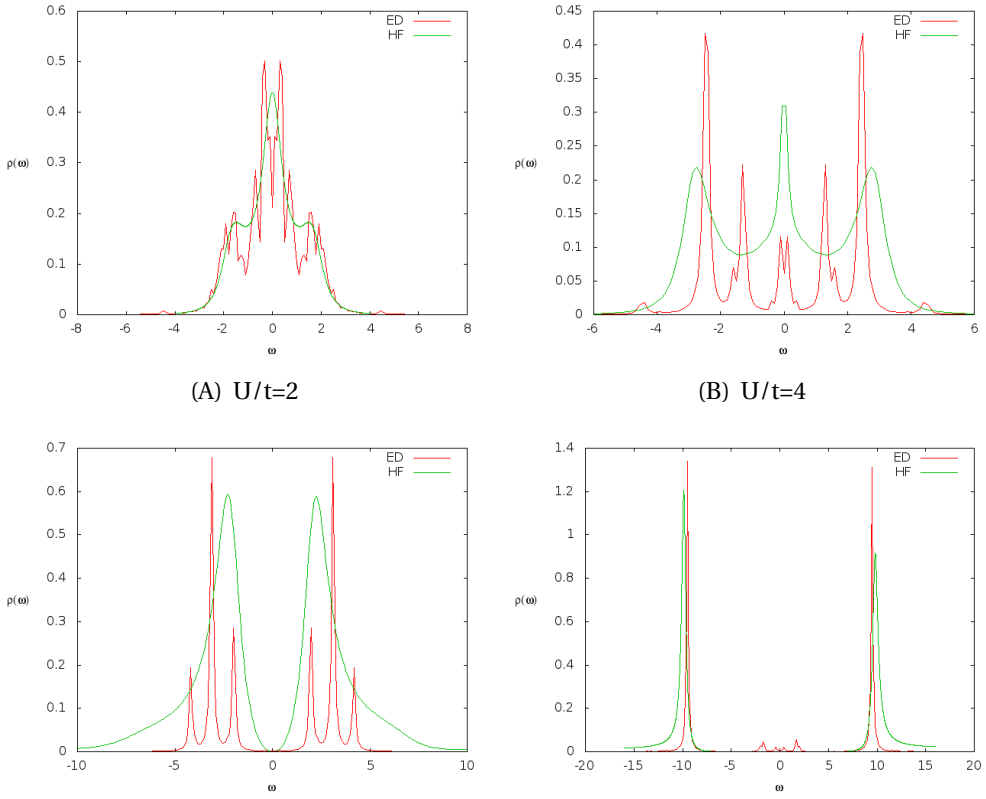
$$G(\omega) = \cfrac{\langle 0|\, d d^\dagger \,|0\rangle}{\omega^> + i\eta - a_0^> - \cfrac{b_1^{>2}}{\omega^> + i\eta - a_1^> - \cfrac{b_2^{>2}}{\omega^> + i\eta - a_2^> - \dots}}} + \cfrac{\langle 0|\, d^\dagger d \,|0\rangle}{\omega^< - i\eta + a_0^> - \cfrac{b_1^{>2}}{\omega^< - i\eta + a_1^> - \cfrac{b_2^{>2}}{\omega^< - i\eta + a_2^> - \dots}}}. \tag{5.110}$$

while in HF calculation, we use Pade approximation whose idea is to fit a rational polynomial function to the data.

$$G(\omega) = \frac{P_n(\omega)}{Q_m(\omega)}, \tag{5.111}$$

where $P_n(\omega)$ and $Q_m(\omega)$ are two polynomial functions with the order n and m respectively.

Fig. 5.5 displays the spectral density of Bethe lattice calculated from ED and HF methods at $T = 0.1$ for different Us. It is observed that in the small U region, HF method yields Kondo peaks at the origin point while ED does not. As U increases, Hubbard bands appear due to the metal-insulator transition and for large U the lattice is an insulator with a big band gap.

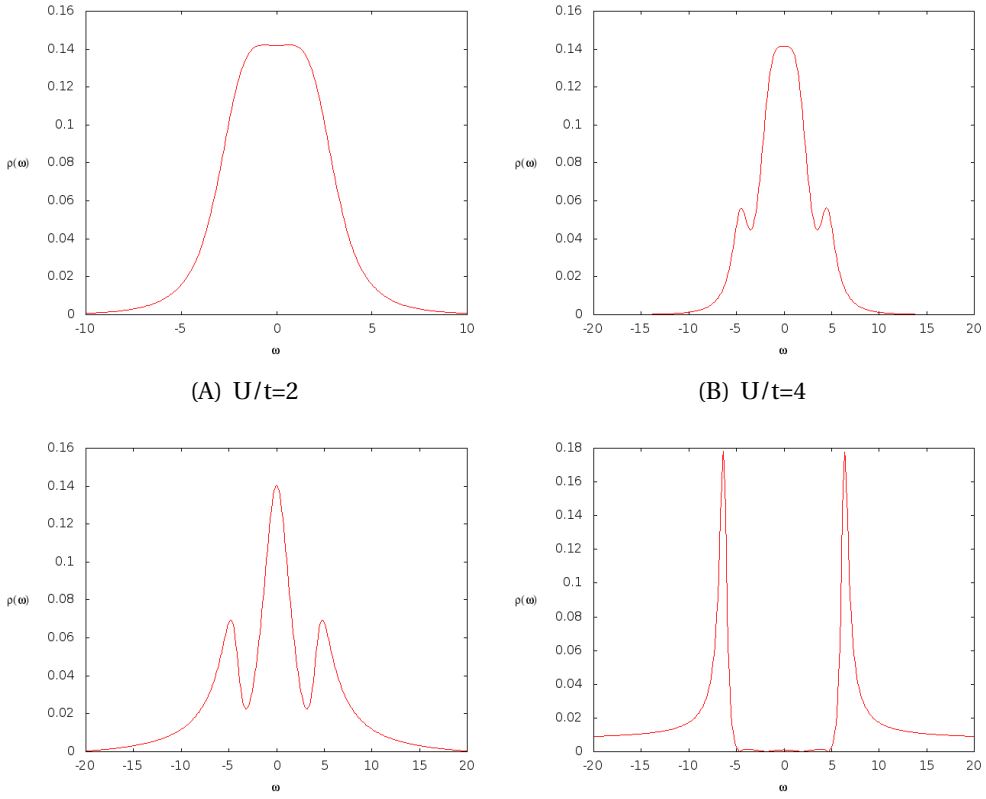


(A) U/t=2 (B) U/t=4

(C) U/t=6 (D) U/t=20

Figure 5.5: Spectral density of Bethe lattice for different Us at $T = 0.1$

We also have the spectral density of three-dimensional Hubbard model by Hirsch-Fye in Fig. 5.6.



(A) U/t=2 (B) U/t=4

(C) U/t=6 (D) U/t=20

Figure 5.6: Spectral density of three-dimensional Hubbard model for different Us at $T = 0.1$

Chapter 6

Summary and future work

6.1 Summary

In this research, ab-initio methods have been employed to study bulk, surface, aqueous fluid interface regions of important mineral materials. It is observed DFT provides good predictions to corundum both in structure and electronic structure. Additional correlation needs to be added to DFT when calculating transition metal oxides/oxyhydroxides. Although DFT prediction in structure (including lattice parameters and bond lengths) is within similar accuracy comparing to DFT+U/hybrid DFT to these materials, DFT+U and hybrid DFT lead to correct physics while DFT fails to predict band gap and other properties in electronic structure.

The calculations of surface and aqueous interface of Hematite (001) and (012) have been carried out in chapter 3. For hematite (001) and (012), ordered water layers and hydrogen bonds in interface regions from the simulations have been reported and compared to experiments. Fe (II) adsorption in interfacial region has also been simulated by AIMD, although electron transfer doesn't happen spontaneously in the 15s ps simulations, our electronic structure analysis provide some insights in understanding the electron transfer mechanism. AIMD simulations of O-terminated surface with aqueous fluid interface have been taken in

different sizes of computational cells. Direct comparisons of multiple ab initio molecular dynamics (AIMD) simulations with high-resolution specular X-ray reflectivity (XR) data have been carried out.

In Chapter 4 we study symmetry breaking in the mean field solutions to the 2 electron hydrogen molecule within Kohn Sham (KS) local spin density function theory with Dirac exchange (the XLDA model). This simplified model shows behavior related to that of the (KS) spin density functional theory (SDFT) predictions in condensed and molecular systems. The Kohn Sham solutions to the constrained SDFT variation problem under go spontaneous symmetry breaking as the relative strength of the non- convex exchange term increases. This results in the change of the molecular ground state from a paramagnetic state to an antiferromagnetic ground states and a stationary symmetric delocalized 1st excited state. We further characterize the limiting behavior of the minimizer when the strength of the exchange term goes to infinity. This leads to further bifurcations and highly localized states with varying character. The stability of the various solution classes is demonstrated by Hessian analysis. Finite element numerical results provide support for the formal conjectures.

6.2 Future Work

6.2.1 QM/MM simulation in the interface region

The simulation of complex chemical systems often requires a multi-level description, in which a region of special interest is treated using a computationally expensive quantum mechanical (QM) model while its environment is described by a faster, simpler molecular mechanical (MM) model [50, 97]. The correctness and efficiency of this method has been proved from biological systems [118, 128] to physical systems [34]. In AIMD of mineral/aqueous fluid interface, the thickness of liquid water slab in the simulation can significantly influence the properties of interfacial region. But we are not focusing in the bulk water properties or process

in bulk water region in interface simulations. So MM could be applied to bulk water region in which way much more bulk water molecules (or thicker water slabs) could be included without too much increase of computational cost, while QM (usually DFT or DF+U) can be applied to interfacial region which we focus on.

6.2.2 Dynamic Mean Field theory

Our long term objective is to solve the real solid system using DMFT embedding. In real DMFT calculation, a realistic start point of the loop is necessary. Density of states from the system calculated by other methods such as DFT has to be presented. After the Hamiltonian is solved and local Green's function is built, Hilbert transformation is a useful tool to produce Green's function with self energy. Then from the new Green's function we can get the new self energy. The loop is iterated until self consistence is achieved. In near future, I will be working on this real DMFT loop. My objective for my PhD education is to develop Lanczos and full CI solvers and implement them in DMFT to solve periodic Anderson model. Moreover, imbedding DMFT in DFT is also a topic I will do research on and the target is to apply DMFT or DMFT+DFT to surface calculation. The electronic structure at iron oxide surface or solid/solution interfaces will be calculated and the localization of electron will be studied.

We will apply both exact diagonalization and Hirsch-Fye QMC methods to study the electron behavior of iron oxides such as hematite and goethite that are strongly correlated systems with electrons on d orbitals. For now the single site in the Anderson model has only one orbital. Mutl-orbital Anderson model will then be developed and used to calculate the spectral density of iron oxides.

6.2.3 Symmetry Breaking

A similar analysis to the large α case gives that the ground state Euler-Lagrange equation for large R can be transformed to an equation of the form

$$-\Delta\phi_{\pm} + R^2 E(R) - RV_1\phi_{\pm} + \frac{2}{R}\int \frac{|\phi_+|^2 + |\phi_-|^2}{|x-y|}\phi_{\pm}(x) + R\alpha|\phi_{\pm}|^{\frac{2}{3}}\phi_{\pm} = 0, \tag{6.1}$$

taking $\phi_{\pm} = R^{\frac{3}{2}}\psi_{\pm}$. This correlates to a new problem with no Coulomb repulsion, large but unit distance apart nuclear masses $Z = R$, and a very strong exchange-correlation nonlinearity $R\alpha$. Thus, the main issue is to study the nature of the stable curve for a large nuclear mass with strong exchange-correlation nonlinearity and observe what the nature of the Lagrange multiplier $R^2E(R)$ should be as $R \to \infty$. The intuition is that this scales the problem to be localized since moving along the stable branch of states from low electron mass (small Lagrange multiplier) for the potential V_1 to large electron mass (large Lagrange multiplier) eventually concentrates onto localized states over each well. As the nonlinearity is growing in strength with the nuclear potential, this bifurcation onto localized modes will still happen at relatively low mass since after a scaling the model Lagrangian is

$$\frac{1}{2}\int |\nabla\phi|^2 dx + R\left(\int V_1|\phi|^2 dx - \alpha\int |\phi|^{\frac{8}{3}} dx\right), \quad \|\phi\|_{L^2} = 1, \tag{6.2}$$

meaning the behavior for large R should correlate to the mass 1 stability profile of the simplified (6.2).

Choosing $\phi_{\pm} = R^{\frac{3}{2}}\psi_{\pm}(Rx)$, the resulting modified Lagrangian has critical points given by

$$-\epsilon^2\Delta\phi_{\pm} + \phi_{\pm} - V_1\phi_{\pm} + \int \frac{|\phi_+|^2 + |\phi_-|^2}{|x-y|}\phi_{\pm}(x) + \alpha|\phi_{\pm}|^{\frac{2}{3}}\phi_{\pm} = 0, \tag{6.3}$$

which looks like a singular-perturbation Ginzburg-Landau style. As a result, this motivates the

following question for a (strange) Hydrogen model: Is the minimizer of

$$E_H(u) = \frac{1}{2}\int |\nabla u|^2 \,\mathrm{d}x - \int \frac{Z}{|x|}|u|^2(x)\,\mathrm{d}x + \frac{1}{2}\iint \frac{|u|^2(x)|u|^2(y)}{|x-y|}\,\mathrm{d}x\,\mathrm{d}y - \int |u|^{8/3} dx \tag{6.4}$$

such that $\|u\|_{L^2} = 1$ orbitally stable. This has been answered in some sense when $Z = 0$ in [125] when the mass is that of the absolute minimizer. Understanding what occurs for the natural electronic mass 1 requires further investigation of this model and will be a topic of future work.

Appendix A

We recall here the basics of the finite element methods we use in this work to numerically find critical points of the XLDA Lagrangian. The numerical algorithms are implemented using a *python* implementation of the FENICS finite element package, [47]. Many of the tools we use here are discussed in more detail in the works [26, 70]. For complete discussions of Finite Element Methods, see the books of [4, 13, 18, 5]. The method we develop here takes advantage of the sparsity of the FEM representation of the eigenvalue problem leading to an algorithm that scales linearly with number of basis functions. For resources on large scale computing in computational chemistry, see [74, 146].

A.1 Finite Element Set Up

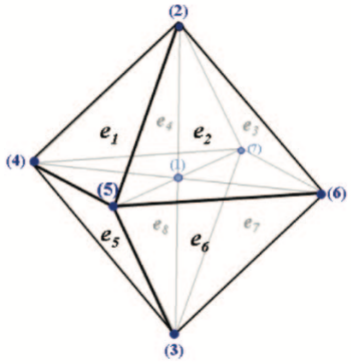


Figure A.1: Finite element tetrahedron defining FEM elements and nodes. The L tetrahedral elements are identified by e_l. The global node are indexes by (m). For each element e_l a there is global node at each corner. Generally a local nodes belonging to individual tetrahedra are also defined. see [18, 4, 13, 26].These are not shown and are managed transparently by the Dolfin software [96].

Assume that the solution, ϕ exists in a bounded domain $\Omega \in \mathscr{R}^3$ that can be divided into a set of L non overlapping tetrahedral elements, $\{e_l\}_{l=1}^{L}$ [18, 4, 13, 26], see Figures (A.1) and (4.1). For the electronic structure problems we are concerned with in this work the atomic potentials represented by $V(\vec{r})$ in the Hamlitonian below Eq. (A.6) are singular. This leads to

rapid variation of the solution to the eigenvalue problem in this region. This requires that in order to obtain accuracy the FEM grid in this region must have a finer resolution as illustrated in Figure 4.1 and discussed in [27, 79, 26].

To construct the grid used in the calculation, we

1. Use BoxMesh to generate a coarse mesh in a $50 \times 50 \times 50$ domain. The initial number of cells in each direction is 2. So the total number of tetrahedra will be 48 and the total number of vertices will be 27 in the coarse mesh.

2. Find the closest mesh grids to the nuclei and set the parameter *cell_markers* true and use the refine function in DOLFIN [1, 26, 18, 4, 13] to refine the grids 20 times.

3. Refine the whole grids for 3 times.

Generally FEM nodes can be located at corners in along boundaries or in the centers of regions (tetrahedra) [18, 4, 13, 1]. However, for the calculations her nodes are located only at the corners of the tetrahedra. These nodes are shared by adjacent tetrahedra as in Figure (A.1). Each tetrahedral l has four corner nodes. A global index identifies a node as in Figure (A.1) (global node numbers in brackets). There are M global nodes in the construction. In actual calculations a local node index identifying a corner global node with a basis function inside a particular tetrahedral is also defined in Dolfin[1, 26, 18, 4, 13] to identify variation associated with a node within a particular tetrahedra [18, 4, 13, 1]. The somewhat difficult book keeping problem of keeping track of the global variation of the basis functions consistent with their local behavior is taken care of nicely in the FEniCS software.[95]

For each node (with global index m and local index i) in a tetrahedral element, l, a finite element basis functions $\{\chi_i^{e_l}\}$ is defined. In these caculations the $\{\chi_i^{e_l}\}$ are linear functions centered on local nodes i in element e_l [1, 26, 18, 4, 13]. For each global node m the linear basis function $\{\chi_i^{e_l}\}$ is 1 on global node i and zero on all other nodes contained in the tetrahedrals containing global node m. For a particular tetrahedron the linear basis associated with local node i of tetrahedral e_l, $\{\chi_i^{e_l}\}$, has value only in tetrahedra e_l. Illustrations of how this works

are given in [1]. The local node functions $\{\chi_i^{e_l}\}$ can be assembled in functions centered around the global nodes with index m as the global basis functions $\eta_m(\vec{r})$.

A piecewise continuous function (here the $\phi(\vec{x})$) can now be expanded as [26],

$$\phi(\vec{r}) = \sum_{m=1}^{M} c_m \eta_m(\vec{r}). \tag{A.1}$$

Here, M is the dimension of space of global nodes and c_m is the coefficient of basis element η_m. The value of the ψ_i on node i is c_m.

A.2 The Generalized Eigenvalue Problem:

With the above formulation, solving the Kohn-Sham minimization problem related to Eq. (4.3) leads to the generalized eigenvalue problem,

$$\mathbf{Hc} = \epsilon \mathbf{Sc}, \tag{A.2}$$

or more explicitly

$$H_{mn} c_{n,k} = \epsilon_k S_{mn} c_{n.k} \tag{A.3}$$

where k identifies the k^{th} eigenfunction,

$$S_{mn} = \int_{\Omega} d\vec{r} \eta_m(\vec{r}) \eta_n(\vec{r}), \tag{A.4}$$

and

$$H_{mn} = \frac{1}{2} \int_{\Omega} d\vec{r} \nabla\eta_m(\vec{r}) \nabla\eta_n(\vec{r}) + \int_{\Omega} d\vec{r} \eta_m(\vec{r}) V_{\text{eff}} \eta_n(\vec{r}) \tag{A.5}$$

with V_{eff} given by

$$V_{\text{eff}} = V(\vec{r}) + V_{ee}(\rho) + V_{ex}(\rho, \alpha) = V(\vec{r}) + \int \frac{\rho(r')}{|\vec{r} - \vec{r'}|} d\vec{r'} + V_{ex}(\rho, \alpha). \tag{A.6}$$

Here $\rho(\vec{r})$ is the total electron density, $\left[\phi_+^2 + \phi_-^2\right]$ and $V_{ex}(\rho,\alpha)$ is given by the scaled Dirac form studied above,

$$V_{ex}(\rho,\alpha) = \alpha\rho^{\frac{1}{3}}. \tag{A.7}$$

The matrix H_{mn}, Eq.(A.5), the overlap matrix S_{mn}, Eq. (A.4) and integrals over $V(\vec{r})$ in Eq. (A.6) can be obtained from the FEnics software [95]. The calculation of these matrix are also carefully discussed for electronic structure problem in ([26]) and in general in [18, 4, 13]. However, the full potential $V_{eff}(\rho)$ given by Eq. (A.6) is a function of the density requiring that the eigenvalue problem, Eq. (A.2), be solved iteratively to achieve self consistency.

A.3 Solution to the generalized eigenvalue problem and the associate Coulomb problem

The principle objective of the calculation is the solution of the generalized eigenvalue problem, Eq. (A.2). However, this 1st requires the input of a current estimate of the Classical potential V_{ee} required in V_{eff}, Eq. (A.6). This may be found as the solution to the Poisson equation

$$\nabla^2 V_{ee}(\vec{r}) = -4\pi\rho(\vec{r}) = -4\pi \sum_{i=1}^{N_e/2} \left|\phi_i(\vec{r})\right|^2. \tag{A.8}$$

To solve this pde $V_{ee}(\rho(\vec{(}r))$ is also expanded in the finite element basis as,

$$V_{ee}(\vec{r}) = \sum_{m=1}^{M} \upsilon_m \eta_m(\vec{r}). \tag{A.9}$$

Eq. (A.8) is then discretized and reduced to a system of linear equations giving the $\{\upsilon_m\}$. Given a solution to the Coulomb problem, Eq. (A.8), based on a current density for the iteration, the generalized eigenvalue problem, Eq. (A.2) is also solved in the $\{\eta_m\}_{m=1}^M$ finite element basis functions. Each molecular orbital is represented as, (for this problem there is only one filled

molecular orbital for each spin)

$$\phi_i = \sum_{\alpha=1}^{M} c_{im}\eta_m, i = 1,\ldots,n. \tag{A.10}$$

The finite element discretization of the one-electron equation for the current iteration is given as,

$$(T_i - \epsilon_i)c_i = v_i(\vec{r}). \tag{A.11}$$

$c_i = \{c_{i1},\ldots,c_{im}\}$ are the coefficients of molecular orbital in the expansions of finite element basis. The elements of the operator $(T_i - \epsilon_i)$, are,

$$(T_i - \epsilon_i)_{mn} = \int_\Omega \left\{ \frac{1}{2}\nabla\eta_m\nabla\eta_n - \epsilon_i\eta_m\eta_n \right\} d\Omega. \tag{A.12}$$

The elements of v_i are,

$$\begin{aligned}(v_i)_m &= \int \eta_m(\vec{r})V_{\text{eff}}(\vec{r})\phi_i(\vec{r})d\Omega \\ &= \int_\Omega \eta_m \left\{ V(\vec{r})\phi_i(\vec{r}) - \int \frac{\left(|\phi_+(y)|^2 + |\phi_-(y)|^2\right)}{|x-y|}\mathrm{d}y\phi_i - \frac{4}{3}\alpha|\phi_i(x)|^{2/3}\phi_i \right\} d\Omega,\end{aligned} \tag{A.13}$$

are calculated in an iterative process in which $V_{\text{eff}}(\vec{r})$ is defined for step k from the results of the self-consistent solver in the prior iteration.

A.3.1 Details of the FEniCS solver

The AMG is based on a V-cycle with a maximum number of multi grid levels of 25. For each fine to course grid transfer a single pre smoothing step is taken. For each course to fine transfer a single post smoothing step is taken. These smoothing steps use a symmetric-SOR/Jacobi method. On the coarsest level the course FEM equation is relaxed by Gaussian

elimination. In the iteration an energy correction step is applied to update new eigenvalues after the Helmholtz equation is solved for a set of $\epsilon^{(k)}$ from the prior AMGCG cycle (see Appendix). The self-consistent solver converges when the total energy difference in two consecutive iterations is smaller than a selected tolerance (see appendix). These are solved via the FEniCs code using the GMRES [127] and BOOMER AMG (Algebraic Multigrid [19]) packages. The solution to this problem is of order M [70].

Eq. (A.11) or (A.12) can be solved in $O(m)$ steps using the FEniCS software [95] The solution to Eq. (A.12) is can be solved by general minimal residue method (GMRES) [127] using the FEniCS software. To improve the convergence of the solution to a preconditioning based on the algebraic multigrid method is used [139, 147]. For an introduction to multigrid methods and their application to problems in electronic structure, see [27, 79, 19, 14, 15, 16, 17, 60, 63, 101].

A.4 The Wavefunction and Orbital Energy update and iteration

A.4.1 Some Preliminaries

The eigenvalue problem is solved using an iterative process in which for step k the ϕ_{pm} on right hand side of Eq. (A.11) and the orbital energies, $\epsilon_{\pm}^{(k)}$, at step k are assigned the the values and functionality from the $k-1$ step The iteration is developed with the intention of producing linear scaling in the number of FEL basis functions m. We note that *scaling in the number of electrons (n) is typically higher.* This is achieved by developing a solver strategy that emphasizes the use of the operator $(\nabla^2 - k^2)$ which is easily implemented in multigrid schemes.

The density functional equations at iteration k are written as

$$\left[-\frac{1}{2}\nabla^2_{\vec{r}} - \epsilon_i\right]\phi_i^{(k+1)}(\vec{r}) = \left[V_{ext}(\vec{r}) + V_{ee}(\rho^{(k)}(\vec{r}) + V_{ex}(\rho^{(k)}(\vec{r}))\right]\phi_i^{(k)}(\vec{r}) \tag{A.14}$$

Here n is the number of filled electron states and V_i^{ext} is the external potential. The Coulomb potential (calculated from FeniCS as above) is defined by

$$V_{ee}(\vec{r}) = \int \frac{\phi_j^{(k)}(\vec{r'})\phi_j^{(k)}(\vec{r'})}{\left|\vec{r} - \vec{r'}\right|} d\vec{r'}. \tag{A.15}$$

The exchange potential is given by

$$V_{ex}(\vec{r}) = \alpha\rho^{(k)}(\vec{r})^{\frac{1}{3}}. \tag{A.16}$$

In this work we developed a multigrid based solver that captures the efficiency of the sparsity of the FEM representation of the eigenvalue problem.
The point here is that this is now a linear PDE of the form

$$\left[-\frac{1}{2}\nabla^2_{\vec{r}} - \epsilon_i^{(k-1)}\right]\phi_i^{(k)}(\vec{r}) = f_i^{(k-1)}(\vec{r}) \tag{A.17}$$

We now calculate the solution to this equation using an efficient multigrid method. Because of the complexity of the grid we use the AMGCG implemented in the FEniCS software [95]. At this point we have an equation that efficiently updates $\phi_i^{(k-1)}$ to $\phi_i^{(k)}$. But for a full update we need $\epsilon^{(k)}$. To obtain the energy update Houdong introduced two methods. The most straightforward is to use the updated $\phi_i^{(k)}$ to diagonalize the Fock matrix. A second method develops an iterative solution.

Update of the wavefunction, $\phi_i(\vec{x})$:

Suppose we have solutions $\phi_i^{(k-1)}(\vec{x})$ and $\epsilon_i^{(k-1)}$. The update of $\phi_i^{(k-1)}(\vec{x})$ to $\phi_i^{(k)}(\vec{x})$ proceeds directly from

$$\phi_i^{(k)}(\vec{x}) = \left[-\frac{1}{2}\nabla_{\vec{x}}^2 - \epsilon_i^{(k-1)} \right]^{-1} f_i^{(k-1)}(\vec{x}). \tag{A.18}$$

All the functions in this equation are defined. Indeed, this is the solution that we obtain from AMGCG. This then is the update of the wave function from $\phi_i^{(k-1)}(\vec{x})$ to $\phi_i^{(k)}(\vec{x})$, which we will sometimes refer to $\tilde{\phi}_i^{(k)}(\vec{x})$ below. Now we also need an update of the orbital energy.

A.4.2 Update of the orbital energy:

Again we assume we have $\phi_i^{(k-1)}(\vec{x})$ and $\epsilon_i^{(k-1)}$. Keep in mind that we obtained $\phi_i^{(k-1)}(\vec{x})$ from an AMGCG upgrade using the potentials $f_i^{(k-2)}(\vec{x})$. We begin by defining two Greens functions (propagators):
The $(k-1)$ Green's function, $G_i^{(k-1)}$, with energy $\epsilon^{(k-1)}$:

$$G_i^{(k-1)} = \left\{ -\frac{1}{2}\nabla^2 - \epsilon_i^{(k-1)} \right\}^{-1} \tag{A.19}$$

and a Green's function, G_i^{con} with the converged HF orbital energy, ϵ_i^{con},

$$\epsilon_i^{con} = (\epsilon_i^{(k-1)} + \delta\epsilon_i^{(k-1)}) \tag{A.20}$$

giving

$$G_i^{con} = \left\{ -\frac{1}{2}\nabla^2 - \epsilon_i \right\}^{-1} = \left\{ \frac{1}{2}\nabla^2 - (\epsilon_i^{(k-1)} + \delta\epsilon_i^{(k-1)}) \right\}^{-1} \tag{A.21}$$

the objective is to calculate an orbital energy correction from these equations.

Suppose that $\phi_i^{(k-1)}$ is a good approximation to the converged HF orbital ϕ_i^{con}. ϕ_i^{con} satisfies the Fock orbital PDE with solution,

$$\phi_i^{con}(\vec{x}) = \left\{-\frac{1}{2}\nabla^2 - \epsilon_i^{con}\right\}^{-1} f_i^{con}(\vec{x}). \tag{A.22}$$

In this equation ϵ_i^{con} is the converged orbital energy. We also define $\delta\epsilon_i^{(k-1)}$ (*the energy update*) by

$$\epsilon_i^{con} = \epsilon_i^{(k-1)} + \delta\epsilon_i^{(k-1)} \tag{A.23}$$

$\phi^{(k-1)}$ is a good approximation to ϕ_i^{con}. That means it approximately satisfies,

$$\phi_i^{(k-1)}(\vec{x}) = \left\{-\frac{1}{2}\nabla^2 - \epsilon_i\right\}^{-1} f i_i^{(k-1)}(\vec{x}) = \left\{-\frac{1}{2}\nabla^2 - (\epsilon_i^{(k-1)} + \delta\epsilon_i^{(k-1)})\right\}^{-1} f^{(k-1)}(\vec{x}) \tag{A.24}$$

Now we need to expand the full Greens function (RHS) in the energy correction $\delta\epsilon_I^{(k-1)}$ to obtain an equation that will update the orbital energy (find an optimal correction to $\epsilon_i^{(k-1)}$).

Now we use the operator identity

$$\frac{1}{(1+a+b)} = \frac{1}{(1+a)} + \frac{1}{(1+a)}\frac{-b}{(1+a+b)}. \tag{A.25}$$

Using in the full propagator we obtain (reproduced from above for completeness)

$$\begin{aligned}\left\{-\frac{1}{2}\nabla^2 - \epsilon_i^{(k-1)} - \delta\epsilon_i^{(k-1)}\right\}^{-1} =& \left\{-\frac{1}{2}\nabla^2 - \epsilon_i^{(k-1)}\right\}^{-1} - \left[\left\{-\frac{1}{2}\nabla^2 - \epsilon_i^{(k-1)}\right\}^{-1}\right. \\ & \left.\left\{-\delta\epsilon_i^{(k-1)}\right\}\left\{-\frac{1}{2}\nabla^2 - \epsilon_i^{(k-1)} - \delta\epsilon_i^{(k-1)}\right\}^{-1}\right].\end{aligned} \tag{A.26}$$

Iteration of this equation to obtain an expression for the propagator to 1st order in the number

$\delta\epsilon_i^{(k-1)}$ we obtain,

$$\begin{aligned}\left\{-\frac{1}{2}\nabla^2-\epsilon_i^{(k-1)}-\delta\epsilon_i^{(k-1)}\right\}^{-1} =&\left\{-\frac{1}{2}\nabla^2-\epsilon_i^{(k-1)}\right\}^{-1}-\left[\left\{-\frac{1}{2}\nabla^2-\epsilon_i^{(k-1)}\right\}^{-1}\right.\\ &\left.\times\left\{\delta\epsilon_i^{(k-1)}\right\}\left\{-\frac{1}{2}\nabla^2-\epsilon_i^{(k-1)}\right\}^{-1}\right].\end{aligned} \tag{A.27}$$

Now we can use this result in Eq. (A.24) to obtain,

$$\begin{aligned}\phi_i^{(k-1)}(\vec{x}) =&\left\{-\frac{1}{2}\nabla^2-\epsilon^{(k-1)}\right\}^{-1}f_i^{(k-1)}(\vec{x})\\ &-\left\{-\frac{1}{2}\nabla^2-\epsilon^{(k-1)}\right\}^{-1}\delta\epsilon^{(k-1)}\left\{-\frac{1}{2}\nabla^2-\epsilon^{(k-1)}\right\}^{-1}f_i^{(k-1)}(\vec{x}).\end{aligned} \tag{A.28}$$

In vector notation this is,

$$\begin{aligned}\left|\phi_i^{(k-1)}(\vec{x})\right\rangle =&\left\{-\frac{1}{2}\nabla^2-\epsilon^{(k-1)}\right\}^{-1}\left|f_i^{(k-1)}\right\rangle\\ &-\left\{-\frac{1}{2}\nabla^2-\epsilon^{(k-1)}\right\}^{-1}\delta\epsilon_i^{(k-1)}\left\{-\frac{1}{2}\nabla^2-\epsilon^{(k-1)}\right\}^{-1}|f_i^{(k-1)}\rangle\end{aligned} \tag{A.29}$$

or

$$\begin{aligned}0=&-\left|\phi_i^{(k-1)}\right\rangle+\left\{-\frac{1}{2}\nabla^2-\epsilon^{(k-1)}\right\}^{-1}\left|f_i^{(k-1)}\right\rangle\\ &-\left\{-\frac{1}{2}\nabla^2-\epsilon^{(k-1)}\right\}^{-1}\delta\epsilon_i^{(k-1)}\left\{-\frac{1}{2}\nabla^2-\epsilon^{(k-1)}\right\}^{-1}|f_i^{(k-1)}\rangle\,.\end{aligned} \tag{A.30}$$

Closing this equation on the left with $\left\langle f^{(k-1)}\right|$ gives a linear expression for $\delta\epsilon_i^{(k-1)}$ which may be in terms of the $\tilde{\phi}_i^{(k-1)}$ as,

$$\begin{aligned}0=&-\left\langle f_i^{(k-1)}\middle|\phi_i^{(k-1)}\right\rangle+\left\langle f^{(k-1)_i}\middle|\tilde{\phi}_i^{(k-1)}\right\rangle\\ &-\delta\epsilon_i^{(k-1)}||\left\langle\tilde{\phi}^{(k-1)_i}\middle|\tilde{\phi}_i^{(k-1)}\right\rangle||^2.\end{aligned} \tag{A.31}$$

This may be solved for $\delta\epsilon_i^{(k-1)}$ to obtain

$$\delta\epsilon_i^{(k-1)} = \frac{-\left\langle f_i^{(k-1)} \middle| \phi_i^{(k-1)} \right\rangle + \left\langle f^{(k-1)_i} \middle| \tilde{\phi}_i^{(k-1)} \right\rangle}{|| \left\langle \tilde{\phi}^{(k-1)_i} \middle| \tilde{\phi}_i^{(k-1)} \right\rangle ||^2}. \tag{A.32}$$

This is essentially Eq. (4.4.10) in [70] and the equation we use in our iteration.

A.5 The Self Consistent Iteration

Algorithm 1 shows the process of the self-consistent solver. An initial guess $(c_i^{(0)}, \epsilon_i^{(0)})$, $i = 1, \ldots, n$ is given to start the self-consistent solver. The self-consistent solver will stop when the total energy difference in two consecutive iterations is smaller than the tolerance TOL.

Algorithm 1 The Self-consistent Iteration

Input $(c_i^{(0)}, \epsilon_i^{(0)})$, $i = 1, \ldots, n$, TOL;
while $\|\epsilon_{total}^{(k)} - \epsilon_{total}^{(k-1)}\|$ >TOL **do**
  Evaluate potentials $V_{ij}^{(k)}$, $i, j = 1, \ldots, n$;
  Evaluate $v_i^{(k)}(\vec{x})$, $i = 1, \ldots, n$;
  Solve Helmholtz equation, and get updated $\{c_i^{(k+1)}, i = 1, \ldots, n\}$;
  energy correction step, and get updated $\{\epsilon_i^{(k+1)}, i = 1, \ldots, n\}$;
  k++;
Output (c_i, ϵ_i), $i = 1, \ldots, n$.

A.6 Hessian analysis

The unrestricted density functional theory for two-electrons' system has two orbital wavefunctions (ψ_+, ψ_-). The model we discussed below is local spin density approximation without correlation energy functional. Total energy functional is $E(\psi)$ is

$$E_\alpha(\psi_+,\psi_-)=\frac{1}{2}\int\left|\nabla\psi_+\right|^2\mathrm{d}x+\frac{1}{2}\int\left|\nabla\psi_-\right|^2\mathrm{d}x+\int V_R(x)\left(\left|\psi_+(x)\right|^2+\left|\psi_-(x)\right|^2\right)\mathrm{d}x$$
$$+\frac{1}{2}\iint\frac{\left(\left|\psi_+(x)\right|^2+\left|\psi_-(x)\right|^2\right)\left(\left|\psi_+(y)\right|^2+\left|\psi_-(y)\right|^2\right)}{\left|x-y\right|}\mathrm{d}x\,\mathrm{d}y-\alpha\int\left(\left|\psi_+(x)\right|^{8/3}+\left|\psi_-(x)\right|^{8/3}\right)\mathrm{d}x, \tag{A.33}$$

where $V_R(x)$ is the nuclear potential. The constraints on (ψ_+,ψ_-) are

$$\int\left|\psi_i(x)\right|^2\mathrm{d}x=1, i=+,-. \tag{A.34}$$

By Lagrange multiplier method, we have

$$L(\psi_+,\psi_-,\epsilon_+,\epsilon_-)=\frac{1}{2}\int\left|\nabla\psi_+\right|^2\mathrm{d}x+\frac{1}{2}\int\left|\nabla\psi_-\right|^2\mathrm{d}x+\int V_R(x)\left(\left|\psi_+(x)\right|^2+\left|\psi_-(x)\right|^2\right)\mathrm{d}x$$
$$+\frac{1}{2}\iint\frac{\left(\left|\psi_+(x)\right|^2+\left|\psi_-(x)\right|^2\right)\left(\left|\psi_+(y)\right|^2+\left|\psi_-(y)\right|^2\right)}{\left|x-y\right|}\mathrm{d}x\,\mathrm{d}y-\alpha\int\left(\left|\psi_+(x)\right|^{8/3}+\left|\psi_-(x)\right|^{8/3}\right)\mathrm{d}x$$
$$-\epsilon_+\left(\int\left|\psi_+(x)\right|^2\mathrm{d}x-1\right)-\epsilon_-\left(\int\left|\psi_-(x)\right|^2\mathrm{d}x-1\right), \tag{A.35}$$

where (ϵ_+,ϵ_-) are the Lagrange multipliers.

Using the Euler-Lagrange equations of the total energy functional with the constraints, which are the effective one-electron eigenvalue equations, we can calculate the extremum of $L(\psi,\epsilon)$

$$\frac{\delta L}{\delta\psi_i}=0\Rightarrow\left(-\frac{1}{2}\nabla^2+V_R(x)+\int\frac{\left(\left|\phi_+(y)\right|^2+\left|\phi_-(y)\right|^2\right)}{\left|x-y\right|}\mathrm{d}y-\frac{4}{3}\alpha\left|\phi_i(x)\right|^{2/3}\right)\phi_i(x)=\varepsilon_i\phi_i(x), i=+,-, \tag{A.36}$$

where (ψ_+, ψ_-) and $(\varepsilon_+, \varepsilon_-)$are the solutions that satisfy the constraints (A.36).

In order to determine whether an extremum is a maximizer, minimizer or saddle point, the second order functional derivative (Hessian matrix) has to be analyzed. Suppose the extremum (ϕ_+, ϕ_-) and $(\varepsilon_+, \varepsilon_-)$ satisfy both (A.36) and (A.34) and (λ_i, w_i) are eigenvalues and eigenvectors of **Hess** respectively, the Hessian analysis involves the solutions of the eigenvalue problems

$$\mathbf{Hess}\, w_i(y) = \int \frac{\delta L(\psi,\epsilon)}{\delta\psi_i(x)\delta\psi_j(y)} w_i(y)\,\mathrm{d}y\Big|_{(\psi,\epsilon)=(\phi,\varepsilon)} = \lambda_i w_i(x), i = +,-, \tag{A.37}$$

which lead to the Hessian matrix

$$\mathbf{Hess} = \begin{pmatrix} H_{11} & \int \frac{2\phi_-(y)}{|x-y|}\mathrm{d}y\phi_+(x) \\ \int \frac{2\phi_+(y)}{|x-y|}\mathrm{d}y\phi_-(x) & H_{22} \end{pmatrix} \tag{A.38}$$

where

$$H_{11} = -\tfrac{1}{2}\nabla^2 + V_R + \int \frac{|\phi_-(y)|^2}{|x-y|}\mathrm{d}y - \tfrac{20}{9}\alpha|\phi_+(x)|^{2/3} - \varepsilon_+,$$
$$H_{22} = -\tfrac{1}{2}\nabla^2 + V_R + \int \frac{|\phi_+(y)|^2}{|x-y|}\mathrm{d}y - \tfrac{20}{9}\alpha(|\phi_-(x)|^{2/3} - \varepsilon_-.$$

and w_i need to satisfy the constraints

$$\int \phi_i(x)\, w_i(x)\,\mathrm{d}x = 0, i = +,- \tag{A.39}$$

meaning that w_i are orthonormal to ϕ_i.

Appendix B

B.1 Background equations

To have all the equations needed for the derivations I will begin with the AIM Hamiltonian.

$$H = \underbrace{\sum_{ij\sigma}^{n_s} t_{ij} c_{i\sigma}^{\dagger} c_{j\sigma} + \sum_{i\sigma}^{n_s} (V_i c_{i\sigma}^{\dagger} d_{\sigma} + \text{H.c.})}_{H^0} + \underbrace{U(n_{d\uparrow} n_{d\downarrow} - \frac{n_{d\uparrow} + n_{d\downarrow}}{2})}_{H_i^{AIM} = H_{\text{int}}} \tag{B.1}$$

To focus the calculation I will develop the computational scheme for the partition function. The approach used is similar to that used for the more complicated Greens functions developed further on.

The partition function is,

$$Z = \mathbf{Tr}\left(e^{-\beta H}\right). \tag{B.2}$$

The the AIM H has a quartic term in the annihilation/creation operators (the electron-electron interaction, H_i Eq.(B.1)), which is computationally intractable. The most accurate method to evaluate the petition function is QMC sampling. Begin by dividing the exponent in βH into M small slices (layers) each $\Delta\tau$ in length, where $\Delta\tau = \frac{\beta}{M}$. Since M is the number of τ slices (layers) the total will vary from $\tau = 0$ to $\tau = M\Delta\tau = \beta$.

$$e^{-\beta H} = \underbrace{e^{-(\Delta\tau H + \cdots + \Delta\tau H)}}_{L\ intervals\ slices} = \underbrace{e^{-\Delta\tau H} e^{-\Delta\tau H} \cdots e^{-\Delta\tau H}}_{L\ slices\ products} = \left[e^{-\Delta\tau H}\right]^L \tag{B.3}$$

The quartic (two particle H_i) part of the H is still difficult to calculate, but because of the smallness of $\Delta\tau$ this may be separated from the single particle part (H_0) using the Trotter-Suzuki breakup, as (Messiah p442),

$$e^{\Delta\tau(H_0 + H_{\text{int}})} = e^{\Delta\tau H_0} e^{\Delta\tau H_{\text{int}}} + O(\Delta\tau^2 [H_0, H_{\text{int}}]). \tag{B.4}$$

The partition function Z now is approximated as,

$$Z = \mathbf{Tr}\left(e^{-\beta H}\right) = \mathbf{Tr}\left(\left[e^{-\Delta\tau(H_0+H_{\rm int})}\right]^M\right) \approx \mathbf{Tr}\left(\left[e^{-\Delta\tau H_0}e^{-\Delta\tau H_{\rm int}}\right]^M\right) + O(\Delta\tau^2 U). \tag{B.5}$$

The nonlinear operator H_i is still difficult to calculate. However the discrete Hubbard-Stratonovich (HS) decomposition of this interaction term reduces the nonlinear contributions to bilinear operators as follows. The HS identity is given as,

$$\begin{aligned} e^{-\Delta\tau H_{\rm int}} &= e^{-\Delta\tau U[n_{d\uparrow}n_{d\downarrow}-\frac{1}{2}(n_{d\uparrow}+n_{d\downarrow})]} = \frac{1}{2}\sum_{s_i=\pm 1} e^{-\lambda s_i(n_{d\uparrow}-n_{d\downarrow})} \\ &= \frac{1}{2}\sum_{s_i=\pm 1} e^{-\sum_\sigma \lambda s_i \gamma_\sigma n_{d\sigma}} = \frac{1}{2}\sum_{s_i=\pm 1}\prod_\sigma e^{-\lambda s_i \gamma_\sigma n_{d\sigma}}. \end{aligned} \tag{B.6}$$

In Eq. (B.6) a discrete variable, $s_i = \pm 1$ (an Ising like spin variable), has been introduced for each layer i. γ_σ is defined by $\gamma_+ = 1$ (spin up) and $\gamma_- = -1$ (spin down). λ is given by

$$\cosh(\lambda) = e^{(\Delta\tau\frac{U}{2})}, \tag{B.7}$$

leading to,

$$\lambda = e^{(\Delta\tau\frac{U}{2})} + \sqrt{e^{(\Delta\tau U)} - 1}. \tag{B.8}$$

To proceed we define a diagonal quadratic operator $\mathscr{V}_\sigma^{(l)}$, which depends on the Ising spin configuration of slice l as,

$$\mathscr{V}_\sigma(i) = \sum_{jk}(\mathbb{V}_\sigma(i))_{jk}c^\dagger_{j\sigma}c_{k\sigma} \tag{B.9}$$

where

$$\mathbb{V}_\sigma(i) = \begin{pmatrix} \frac{\lambda}{\Delta\tau} s_i \gamma_\sigma & 0 & \cdots & 0 \\ 0 & 0 & \cdots & 0 \\ \vdots & \vdots & \ddots & \vdots \\ 0 & 0 & \cdots & 0. \end{pmatrix} \tag{B.10}$$

We have reserved position 1 of the matrix representation for the impurity d_σ orbital. Thus

$$e^{-\Delta\tau H_{\rm int}} = \frac{1}{2}\sum_{s_i,\sigma} e^{-\Delta\tau \mathscr{V}_\sigma(i)} \tag{B.11}$$

Now the partition function becomes

$$\begin{aligned} Z &= \mathbf{Tr}\left(\prod_{i=M}^{1} \left[\sum_{s_1,\cdots,s_M} \frac{1}{2} \prod_\sigma e^{-\Delta\tau H_{0\sigma}} e^{-\Delta\tau \mathscr{V}_\sigma(i)} \right] \right) = \sum_{s_1,\cdots,s_M} Z(s_1,\cdots,s_M) \\ &= \frac{1}{2^M} \sum_{s_1,\cdots,s_M} \mathbf{Tr}\left(\prod_{i=M}^{1} \left[e^{-\Delta\tau H_{0\uparrow}} e^{-\Delta\tau \mathscr{V}_\uparrow(i)} \right] \left[e^{-\Delta\tau H_{0\downarrow}} e^{-\Delta\tau \mathscr{V}_\downarrow(i)} \right] \right) \\ &= \frac{1}{2^M} \sum_{s_1,\cdots,s_M} \mathbf{Tr}\left(\prod_{i=M}^{1} \left[e^{-\Delta\tau H_{0\uparrow}} e^{-\Delta\tau \mathscr{V}_\uparrow(i)} \right] \right) \mathbf{Tr}\left(\prod_{i=M}^{1} \left[e^{-\Delta\tau H_{0\downarrow}} e^{-\Delta\tau \mathscr{V}_\downarrow(i)} \right] \right) \end{aligned} \tag{B.12}$$

Note that now the products in Eq. (B.12) have a i time slab index. $\{s_1,\cdots,s_M\}$ is one set of s_l for the layers where each layer is indexed by the subscript l. $\{s_i\} = \{s_1,\cdots,s_M\}$. In total, there are 2^M possible sets of $\{s\}$. (The difficult step in the problem is now how to calculate the $\sum_{\{s_i\}}$ in Eq. (B.12). In principle this is just a sum but the common size of the problem makes direct calculation very expensive. Here this will be treated as a Metropolis sampling problem.)

H_0 is bilinear in the site basis,

$$H_0 = \sum_{jk\sigma} (\mathbb{H}_0)_{jk} c^\dagger_{j\sigma} c_{k\sigma}. \tag{B.13}$$

Therefore, we can define $\mathbb{H}_{jk\sigma}(i)$

$$\mathbb{H}_{jk\sigma}(i) = (\mathbb{H}_0)_{jk} - \frac{\lambda}{\Delta\tau} s_i \gamma_\sigma \delta_{j=k=1} = (\mathbb{H}_0)_{jk} - \mathbb{V}_{jk\sigma}(i). \tag{B.14}$$

or the operator,

$$H(i)_\sigma = H_0 - \mathscr{V}_\sigma(i). \tag{B.15}$$

From Eq. (B.12) the partition function $Z(\{s_l\})$ at fixed Ising configuration $\{s_l\}$ becomes (within $\Delta\tau$ accuracy because H_0 and $\mathscr{V}^l_\sigma$ don't commute),

$$\begin{aligned} Z(\{s\}) &= \frac{1}{2^M} \mathrm{Tr} \prod_{i=M}^{1} \left[e^{(-\Delta\tau(\sum_{jk} c^\dagger_{j\uparrow} \mathbb{H}_{jk\uparrow}(i) c_{k\uparrow})} \right] \mathrm{Tr} \prod_{i=M}^{1} \left[e^{(-\Delta\tau(\sum_{jk} c^\dagger_{j\downarrow} \mathbb{H}_{jk\downarrow}(i) c_{k\downarrow})} \right] \\ &= \frac{1}{2^M} \mathrm{Tr} \prod_{i=M}^{1} \left[e^{(-\Delta\tau \tilde{H}(i)_\uparrow} \right] \mathrm{Tr} \prod_{i=M}^{1} \left[e^{(-\Delta\tau \tilde{H}(i)_\downarrow)} \right]. \end{aligned} \tag{B.16}$$

B.2 Grouping products of exponentials

To evaluate the **Tr** in Eq. (B.16) we will use the result that the product of exponentials of bilinear layer Hamiltonian operators (we omit the spins)

$$H(i) = \sum_{jk} \mathbb{H}_{jk}(i) c^\dagger_j c_k, \tag{B.17}$$

is equivalent to an exponential of an effective bilinear Hamiltonian,

$$\tilde{H} = \sum_{jk} \tilde{\mathbb{H}}_{jk} c_j^\dagger c_k. \tag{B.18}$$

That is

$$\prod_i e^{-\Delta\tau H(i)} = e^{-\Delta\tau \tilde{H}} \tag{B.19}$$

This will be shown in the following.

In the Schrödinger representation the time dependence of the expectation of an operator, a, evolving under a H, is given by,

$$\begin{aligned} \frac{\partial \overline{a(t)}}{\partial t} &= \left\{ < \frac{\partial \Psi(t)}{\partial t} | a | \Psi(t) > + < \Psi(t) | a | \frac{\partial \Psi(t)}{\partial t} > \right\} \\ &= -\frac{1}{i\hbar} \left\{ < \Psi(t) | Ha | \Psi(t) > - < \Psi(t) | aH | \Psi(t) > \right\} \end{aligned} \tag{B.20}$$

In the Heisenberg representation the evolution of the wave function is replaced by the evolution of operators by introducing a time dependent operator, $a(t)$, given as,

$$a(t) = e^{iHt} a e^{-iHt} \tag{B.21}$$

or in imaginary time (replace it by τ),

$$a(\tau) = e^{H\tau} a e^{-H\tau}. \tag{B.22}$$

From Eq. (B.20) the imaginary time evolution of Heisenberg operators is given by the differential equation,

$$\frac{da(\tau)}{d\tau} = [H, a(\tau)] \tag{B.23}$$

If the operator is a creation operator, $c_i^\dagger$ in the same representation as $H^{(l)}$ used in Eq. (B.17) and defined in Eq. (B.15) we obtain from Eq. (B.23)

$$\frac{dc_r^\dagger}{d\tau} = \sum_{jk} \mathbb{H}(i)_{jk} \left(c_j^\dagger c_k c_r^\dagger - c_r^\dagger c_j^\dagger c_k \right) = \sum_j \mathbb{H}(i)_{jr} c_j^\dagger \tag{B.24}$$

where we have used the anticommutation relations for Fermion operators,

$$\begin{aligned} \left\{ c_r, c_s^\dagger \right\} &= \delta_{r,s} \\ \left\{ c_r, c_s \right\} &= 0. \end{aligned} \tag{B.25}$$

the solution to Eq. (B.24) is,

$$c_j^\dagger(\tau) = \sum_r [e^{\tau H(i)}]_{rj} c_r^\dagger, \tag{B.26}$$

We introduce the imaginary time step $\Delta\tau$ and utilize Eq. (B.22) to obtain from Eq. (B.26),

$$\begin{aligned} c_j^\dagger(\Delta\tau) &= e^{\Delta\tau H(i)} c_j^\dagger e^{-\Delta\tau H(i)} \\ &= \sum_r [e^{\Delta\tau H(i)}]_{rj} c_r^\dagger \end{aligned} \tag{B.27}$$

A similar result for the annihilation operator may be obtained as,

$$\begin{aligned} c_j(\Delta\tau) &= e^{\Delta\tau H(i)} c_j e^{-\Delta\tau H(i)} \\ &= \sum_r [e^{-\Delta\tau H(i)}]_{jr} c_r \end{aligned} \tag{B.28}$$

Note that in the τ coordinate $c^\dagger(\Delta\tau)$ is NOT the Hermitian conjugate of $c(\Delta\tau)$ unless τ is an imaginary.

Now we want to derive the time evolution of $c_j(\Delta\tau)$ and $c_j^\dagger(\Delta\tau)$ under the influence of products of slab operators, $\prod_{i=l_M}^{1} e^{H(i)\Delta\tau}$. Multiplying Eq. (B.27) on the right by $e^{H^{(l)}\Delta\tau}$ we obtain,

$$e^{\Delta\tau H(i)} c_j^\dagger = \sum_r [e^{\Delta\tau H(i)}]_{rj} c_r^\dagger e^{\Delta\tau H(i)}. \tag{B.29}$$

Keeping in mind that Eq. (B.29) results from the bilinear form of the Hamiltonian, Eq. (B.17) we now form a similar product with a 2nd exponential, $e^{\Delta\tau H(i')}$. This yields

$$\begin{gathered} e^{\Delta\tau H(i')} e^{\Delta\tau H(i)} c_j^\dagger = \\ \sum_s \sum_r [e^{\Delta\tau H^{(i')}}]_{sr} [e^{\Delta\tau H^{(i)}}]_{rj} c_s^\dagger e^{\Delta\tau H(i')} e^{\Delta\tau H(i)} = \\ \sum_s [e^{\Delta\tau H(i')} e^{\Delta\tau H(i)}]_{sj} c_s^\dagger e^{\Delta\tau H(i')} e^{\Delta\tau H(i)} \end{gathered} \tag{B.30}$$

Multiplying this equation on the right by $e^{-\Delta\tau H(i)} e^{-\Delta\tau H(i')}$ gives using a more general notation,

$$\begin{aligned} c_{j,\text{slices}}^\dagger(i_1, i_2, \Delta\tau) &= e^{\Delta\tau H(i_2)} e^{\Delta\tau H(i_1)} c_j^\dagger e^{-\Delta\tau H(i_1)} e^{-\Delta\tau H(i_2)} \\ &= \sum_s [e^{\Delta\tau H(i_2)} e^{\Delta\tau H(i_1)}]_{sj} c_s^\dagger = \sum_s [\prod_{q=1,2} e^{\Delta\tau H(i_q)}]_{js} c_s^\dagger \end{aligned} \tag{B.31}$$

We now note that Eq. (B.31) has the same form as a creation operator propagation under a single bilinear Hamiltonian as in Eq. (B.26). From this we can assert that the propagation created by the product of operators would be the same as that for an effective operator, $\tilde{H}_2 = \sum_{js} \tilde{\mathbb{H}}_{js} c_j^\dagger c_s$, defined by the condition,

$$[\prod_{q=1,2} e^{\Delta\tau H(i_q)}]_{js} = \underbrace{[e^{\Delta\tau \tilde{H}_2}]_{js}}_{def\ \tilde{H}_2} \tag{B.32}$$

It is straight forward to treat a product of M exponentials (for M layers) in a manner

similar to that of Eq.s (B.30) and (B.31) to obtain the result,

$$c_j^\dagger(i_1,\ldots,i_M,\Delta\tau) = \left[\prod_{i=M}^{1} e^{\Delta\tau H(i)}\right] c_j^\dagger \left[\prod_{i=M}^{1} e^{-\Delta\tau H(i)}\right]$$
$$= \sum_s [\prod_{i=M}^{1} e^{\Delta\tau H(i)}]_{sj} c_s^\dagger \tag{B.33}$$

leading to the definition of the effective Hamiltonian via,

$$[\prod_i e^{\Delta\tau H(i)}]_{js} \stackrel{\text{def}}{=} \underbrace{[e^{\Delta\tau \tilde{H}}]_{js}}_{def\ \tilde{H}} \tag{B.34}$$

A similar expression may be obtained for $c_j(i_1,\ldots,i_M,\Delta\tau)$

$$c_j(i_1,\ldots,i_M,\Delta\tau) = \prod_{i=M}^{1} e^{\Delta\tau H(i)} c_j \prod_{i=M}^{1} e^{-\Delta\tau H(i)}$$
$$= \sum_s [\prod_{i=M}^{1} e^{-\Delta\tau H(i)}]_{js} c_s \tag{B.35}$$

The definition of a the creation operator in the representation α is,

$$c_j^{\alpha\dagger} |\alpha_1,\ldots,\alpha_N\rangle = |\alpha_j,\alpha_1,\ldots,\alpha_N\rangle \tag{B.36}$$

Now suppose we expand the $|\alpha\rangle$ in $|\beta\rangle$ as,

$$|\alpha_j\rangle = \sum_r |\beta_r\rangle \langle\beta_r|\alpha_j\rangle \tag{B.37}$$

This gives

$$\begin{aligned} c_j^{a\dagger}|\alpha_1^a,\ldots,\alpha_N^a\rangle &= |\sum_r \beta_r \langle\beta_r|\alpha_j\rangle, \alpha_1^a\ldots,\alpha_N^a\rangle \\ &= \sum_r c_r^{\beta\dagger}\langle\beta_r|\alpha_j\rangle|\alpha_1^a\ldots,\alpha_N^a\rangle. \end{aligned} \tag{B.38}$$

This leads to the relation giving the creation operator originally in the α representation in the β representation,

$$c_j^{\alpha\dagger} = \sum_r c_r^{\beta\dagger}\langle\beta_r|\alpha_j\rangle. \tag{B.39}$$

A similar relation can be obtained for the annihilation operator as,

$$c_j^{\alpha} = \left[c_j^{\alpha\dagger}\right]^{\dagger} = \sum_r \left[c_r^{\beta\dagger}\right]^{\dagger}\overline{\langle\beta_r|\alpha_j\rangle} = \sum_r c_r^{\beta}\overline{\langle\beta_r|\alpha_j\rangle} = \sum_r c_r^{\beta}\langle\alpha_j|\beta_r\rangle \tag{B.40}$$

Using Eq. (B.33) the creation operator in the α representation will satisfy the evolution,

$$c_j^{\alpha\dagger}(\Delta\tau) = \sum_r\sum_s[\prod_i e^{\Delta\tau H(l)}]_{sr}c_s^{\beta\dagger}\langle\beta_r|\alpha_j\rangle \tag{B.41}$$

B.3 Calculation of the trace of products of layer propagators of fermion operators

The $|\nu\rangle$ basis with creation and annihilation operators $c_\nu^\dagger$ and c_ν is the diagonal representation for the effective Hamiltonian, $\tilde{H}$, defined in Eq. (B.34). The lattice site basis will be identified as in Eq. (B.17) as the $|j\rangle$ basis with annihilation and creation operators $c_j^\dagger$ and c_j . The usual relations between the annihilation and creation operators in the original basis j and the 'new' basis, ν diagonalizing $\tilde{H}(i)$, are given in Eqs. (B.39) and (B.40) as,

$$c_\nu^\dagger = \sum_j \langle j|\nu\rangle\, c_j^\dagger = \sum_j S_{j\nu} c_j^\dagger \tag{B.42}$$

and

$$c_\nu = \sum_j \langle \nu|i\rangle\, c_j = \sum_j S_{\nu i} c_j, \tag{B.43}$$

where $S_{j\nu}$ is the overlap between the two basis, $S_{i\nu} = \langle i|\nu\rangle$. Assuming $\tilde{H}$, can be diagonalized we have,

$$\tilde{H} \quad = \quad \sum_{jk} \tilde{\mathbb{H}}_{jk} c_j^\dagger c_k = \sum_\nu \tilde{\epsilon}_\nu c_\nu^\dagger c_\nu, \tag{B.44}$$

where

$$\sum_{jk} S_{\nu j}^\dagger \tilde{\mathbb{H}}_{jk} S_{k\nu} = \tilde{\epsilon}_\nu. \tag{B.45}$$

Using the independent particle property of $\tilde{H}$ defined in Eq. (B.34) and Fermion filling rules for the $\tilde{H}$ representation (i.e., n_ν =1 or 0) the trace of the grand partition function, Eq. (B.16), can be calculated as (where we have dropped the spin index),

$$
\begin{aligned}
\mathbf{Tr}\Big(\prod_{M}^{1} e^{-\Delta\tau H(i)}\Big) &= \mathbf{Tr}\Big(e^{-\Delta\tau\tilde{H}}\Big) \\
&= \mathbf{Tr}\Big(e^{-\Delta\tau\sum_{\nu}\tilde{\epsilon}_{\nu}c_{\nu}^{\dagger}c_{\nu}}\Big) \\
&= \mathbf{Tr}\Big(\prod_{\nu} e^{-\Delta\tau\tilde{\epsilon}_{\nu}n_{\nu}}\Big) \\
&= \sum_{\{\nu_i\}}\langle\nu_1,\ldots,\nu_N|\Big(\prod_{\nu} e^{-\Delta\tau\tilde{\epsilon}_{\nu}n_{\nu}}\Big)|\nu_1,\ldots,\nu_N\rangle \\
&= \prod_{\nu}\mathbf{Tr}\Big(e^{-\Delta\tau\tilde{\epsilon}_{\nu}n_{\nu}}\Big) \\
Fermion filling,\Rightarrow \quad &= \prod_{\nu}\{\langle n_\nu=0|\,e^{-\Delta\tau\tilde{\epsilon}_{\nu}n_{\nu}}\,|n_\nu=0\rangle+\langle n_\nu=1|\,e^{-\Delta\tau\tilde{\epsilon}_{\nu}n_{\nu}}\,|n_\nu=1\rangle\} \\
&= \prod_{\nu}(1+e^{-\Delta\tau\tilde{\epsilon}_{\nu}}) \\
&\overset{\text{def}}{=} \mathbf{det}(I+e^{-\Delta\tau\tilde{H}})\ Definition\ of\ the\ Det\ of\ an\ operator \\
&= \mathbf{det}(I+\prod_{M}^{1} e^{-\Delta\tau H(i)}).
\end{aligned}
\tag{B.46}
$$

Using the definition, Eq. (B.15), $Z(\{s_i\})$ can now be written as (to order $\Delta\tau$),

$$
\begin{aligned}
Z &= \sum_{\{s_i\}} Z(\{s_i\}) \\
&= \sum_{\{s_i\}}\frac{1}{2^M}\mathbf{det}\Big(I+\prod_{i=M}^{1} e^{-\Delta\tau H_{0\uparrow}}e^{V_{\uparrow}(i)}\Big)\mathbf{det}\Big(I+\prod_{i=M}^{1} e^{-\Delta\tau H_{0\downarrow}}e^{V_{\downarrow}(i)}\Big) \\
&= \sum_{\{s_i\}}\frac{1}{2^M}\mathbf{det}\Big(I+\prod_{i=M}^{1} M_{\uparrow}(i)\Big)\mathbf{det}\Big(I+\prod_{i=M}^{1} M_{\downarrow}(i)\Big) \\
&= \frac{1}{2^M}\sum_{\{s_i\}}\mathbf{det}\mathbb{O}_{\uparrow}(\{s_i\})\mathbf{det}\mathbb{O}_{\downarrow}(\{s_i\}),
\end{aligned}
\tag{B.47}
$$

where we have introduced the operators $M(i)_\sigma = e^{-\Delta\tau H_{0\sigma}}e^{V_\sigma(i)}$ and the matrix $\mathbb{O}_{\uparrow}(\{s_i\}) = \Big(\mathbb{I}+\prod_{i=M}^{1}\mathbb{M}(i)_\sigma\Big)$.

B.4 Derivation of the noninteracting G^0 for the Anderson model

Here we derive the Greens function for an independent particle Hamiltonian describing the interaction of an d Anderson impurity with lattice waves, The Hamiltonian of the model is,

$$H = (\epsilon_d - \mu) d^\dagger d + \sum_k^{n_L} \epsilon_k c_k^\dagger c_k + \sum_k^{n_L} V_k (c_k^\dagger d + d^\dagger c_k). \tag{B.48}$$

where n_L is the number of lattice sites. ϵ_k is the single particle energy of the k^{th} lattice wave, and $c_k / c_k^\dagger$ are the annihilation and creation operator for lattice waves. $V_{k,d\sigma}$ is the interaction of lattice wave l, σ with the impurity d_σ site. ϵ_d is the energy of the d impurity site orbital and μ is the chemical potential of the d impurity site.

The Green's functions $G^0_{d,d}(\tau)$ and $G^0_{k,d}(\tau)$ are defined as,

$$\begin{aligned} G^0_{d,d}(\tau) &= -i < \tilde{T} d(\tau) d^\dagger(0) > \\ &= -i(\Theta(\tau) < d(\tau) d^\dagger(0) > - \Theta(-\tau) < d^\dagger(0) d(\tau) >) \end{aligned} \tag{B.49}$$

and

$$\begin{aligned} G^0_{k,d}(\tau) &= -i < \tilde{T} c_k(\tau) d^\dagger(0) > \\ &= -i(\Theta(\tau) < c_k(\tau) d^\dagger(0) > - \Theta(-\tau) < d^\dagger(0) c_k(\tau) >) \end{aligned} \tag{B.50}$$

where $\Theta(\tau)$ is the step function.

Taking the derivative of the two green's functions with respect to τ, we can get

$$i \frac{\partial}{\partial \tau} G^0_d(\tau) = \delta(\tau) < d(\tau) d^\dagger(0) + d^\dagger(0) d(\tau) > - i < \tilde{T} e^{iH\tau} [d, H] e^{-iH\tau} d^\dagger > \tag{B.51}$$

and

$$i\frac{\partial}{\partial\tau}G_k^0(\tau) = \delta(\tau) < c_k(\tau)d^\dagger(0) + d^\dagger(0)c_k(\tau) > -i < \tilde{T}e^{iH\tau}[c_k, H]e^{-iH\tau}d^\dagger > \tag{B.52}$$

where

$$[d, H] = (\epsilon_d - \mu)d + \sum_k V_k c_k \tag{B.53}$$

and

$$[c_k, H] = \epsilon_k c_k + V_k d. \tag{B.54}$$

Then Fourier transform the above two equations

$$i\omega G_d^0(i\omega) = 1 + (\epsilon_d - \mu)G_d^0(i\omega) + \sum_k V_k G_k^0(i\omega) \tag{B.55}$$

and

$$i\omega G_k^0(i\omega) = \epsilon_k G_k^0(i\omega) + V_k G_d^0(i\omega). \tag{B.56}$$

Solve the two equations,

$$G_d^0(i\omega) = (i\omega - \epsilon_d + \mu - \sum_k \frac{V_k^2}{i\omega - \epsilon_k})^{-1}. \tag{B.57}$$

Bibliography

[1] Finite element basis functions. hplgit.github.io.

[2] Hypre library. https://computation.llnl.gov/projects/hypre-scalable-linear-solvers-multigrid-methods.

[3] ANANTHARAMAN, A., AND CANCÈS, E. Existence of minimizers for Kohn–Sham models in quantum chemistry. 2425–2455.

[4] AXELSSON, O., AND BARKER, V. A. *Finite Element Solution of Boundary Value Problems: Theory and Computation*. SIAM, 2001.

[5] BANK, R. E., AND DUPONT, T. An optimal order process for solving finite element equations. *Mathematics of Computation 36*, 153 (1981), 35–51.

[6] BARCA, G. M. J., GILBERT, A. T. B., AND GILL, P. M. W. Communication: Hartree-Fock description of excited states of H2. *The Journal of chemical physics 141*, 11 (2014), 111104.

[7] BARDUCCI, A., BONOMI, M., AND PARRINELLO, M. Metadynamics. *Wires Comput Mol Sci 1* (2011), 826–843.

[8] BARNES, H. Geochemistry of hydrothermal ore deposites. *Wiley* (1997).

[9] BECKE, A. Perspective: Fifty years of density-functional theory in chemical physics. *Journal of Chemical Physics 140* (2014).

[10] BENGURIA, R., BRÉZIS, H., AND LIEB, E. H. The thomas-Fermi-von Weizsäcker theory of atoms and molecules. *Communications in Mathematical Physics 79*, 2 (1981), 167–180.

[11] BLAKE, H., ZOLTAI, T., AND FINGER, L. Refinement of the hematite structure. *American Mineralogist 51* (1966), 123–129.

[12] BLÜMER, N. Multigrid hirsch-fye quantum monte carlo method for dynamical mean-field theory. *arXiv:0801.1222* (2008).

[13] BRAESS, D. *Finite elements: theory, fast solvers and applications in solid mechanics, second edition*. Cambridge University Press, 2001.

[14] BRAMBLE, J. H. *Multigrid methods*, vol. 294. CRC Press, 1993.

[15] BRAMBLE, J. H., AND PASCIAK, J. E. New convergence estimates for multigrid algorithms. *Mathematics of computation 49*, 180 (1987), 311–329.

[16] BRANDT, A. Algebraic multigrid theory: The symmetric case. *Applied mathematics and computation 19*, 1 (1986), 23–56.

[17] BRANDT, A., MCCORUICK, S., AND HUGE, J. Algebraic multigrid (amg) f0r sparse matrix equati0ns. *Sparsity and its Applications* (1985), 257.

[18] BRENNER, S. C., AND SCOTT, L. R. *The mathematical theory of finite element methods*, vol. 15. Springer, 2008.

[19] BRIGGS, W. L., HENSON, V. E., AND MCCORMICK, S. F. *A multigrid tutorial: second edition*. SIAM, 2000.

[20] BROWN, G. Surface science - how minerals react with water. *Science 294* (2001), 67.

[21] BROWN, G., HENRICH, V., CASEY, W., CLARK, D., EGGLESTON, C., FELMY, A., GOODMAN, D., GR'ATZEL, M., MACIEL, G., MCCARTHY, M., NEALSON, K., SVERJENSKY, D., TONEY, M., AND ZACHARA, J. Metal oxide surfaces and their interactions with aqueous solutions and microbial organisms. *Chem Rev 99* (1998), 77–174.

[22] BROWN, G., HENRICH, V., CASEY, W., CLARK, D., EGGLESTON, C., FELMY, A., GOODMAN, D., GRATZEL, M., MACIEL, G., MCCARTHY, M., NEALSON, K., SVERJENSKY, D., TONEY, M., AND ZACHARA, J. Metal oxide surfaces and their interactions with aqueous solutions and microbial organisms. *Chem Rev 99* (1999), 77–174.

[23] BURKE, K. Perspective on density functional theory. *Journal of Chemical Physics 136* (2012).

[24] BYLANDER, D., AND KLEINMAN, L. Outer-core electron and valence electron pseudopotential. *Physical Review B 29* (1984), 2274–2276.

[25] BYLASKA, E., TSEMEKHMAN, K., BADEN, S., WEARE, J., AND JONSSON, H. Parallel implementation of γ-point pseudopotential plane-wave dft with exact exchange. *Journal of Computational Chemistry 32* (2011), 54–69.

[26] BYLASKA, E. J., HOLST, M., AND WEARE, J. H. Adaptive finite element method for solving the exact kohn- sham equation of density functional theory. *Journal of Chemical Theory and Computation 5*, 4 (2009), 937–948.

[27] BYLASKA, E. J., KOHN, S. R., BADEN, S. B., EDELMAN, A., KAWAI, R., ONG, M. E. G., AND WEARE, J. H. Scalable parallel numerical methods and software tools for material design. *Proceedings of the Seventh SIAM Conference on Parallel Processing for Scientific Computing* (1995), 219–224.

[28] CAFFAREL, M., AND KRAUTH, W. Exact diagonalization approach to correlated fermions in infinite dimensions: Mott transition and superconductivity. *Physical Review Letters 72* (1994), 1545.

[29] CAR, R., AND PARRINELLO, M. Unified approach for molecular-dynamics and density-functional theory. *Physical Review Letters 555* (1985), 2471–2474.

[30] CATALANO, J. Weak interfacial water ordering on isostructural hematite and corundum (001) surfaces. *Geochimica Et Cosmochimica Acta 75* (2011), 2062–2071.

[31] CATALANO, J., FENTER, P., AND PARK, C. Interfacial water structure on the (012) surface of hematite: Ordering and reactivity in comparison with corundum. *Geochim Cosmochim Ac 71* (2007), 5313–5324.

[32] CATALANO, J., FENTER, P., PARK, C., ROSSO, K., FRIERDICH, A., AND OTEMUYIWA, B. Fe(ii)-induced structural transformations of hematite surfaces and their impact on contaminants. *Geochim Cosmochim Ac 74* (2010a), A150–A150.

[33] CATALANO, J., FENTER, P., PARK, C., ZHANG, Z., AND ROSSO, K. Structure and oxidation state of hematite surfaces reacted with aqueous fe(ii) at acidic and neutral ph. *Geochim Cosmochim Ac 74* (2010b), 1498–1512.

[34] CAUËT, E., BOGATKO, S., WEARE, J., FULTON, J., SCHENTER, G., AND BYLASKA, E. Structure and dynamics of the hydration shells of the zn ion from ab initio molecular dynamics and combined ab initio and classical molecular dynamics simulations. *The Journal of chemical physics 132* (2010), 194502.

[35] CHEN, Y. Ab initio study of structure and dynamics of bulk, surface and the mineral/aqueous fluid interface regions. *UCSD Ph.D. Thesis* (2015).

[36] CHEN, Y., BYLASKA, E., AND WEARE, J. First principles estimation of geochemically important transition metal oxide properties. In *Molecular Modeling of Geochemical Reactions*, J. D. Kubicki, Ed. Wiley, 2016, ch. 4.

[37] CINQUINI, F., GIORDANO, L., PACCHIONI, G., FERRARI, A., PISANI, C., AND ROETTI, C. Electronic structure of nio/ag(100) thin films from dft+u and hybrid functional dft approaches. *Phys Rev B 74* (2006).

[38] COHEN, A. J., MORI-SÁNCHEZ, P., AND YANG, W. Insights into current limitations of density functional theory. *Science 321* (2008), 792 – 794.

[39] COHEN, A. J., MORI-SÁNCHEZ, P., AND YANG, W. Challenges for density functional theory. *Chem. Rev. 112* (2012), 289–320.

[40] CONDON, N., LEIBSLE, F., LENNIE, A., MURRAY, P., PARKER, T., VAUGHAN, D., AND THORNTON, G. Scanning tunnelling microscopy studies of α-Fe_2O_3(0001). *Surface Science 397* (1998), 278–287.

[41] CORA, F., ALFREDSSON, M., MALLIA, G., MIDDLEMISS, D., MACKRODT, W., DOVESI, R., AND ORLANDO, R. The performance of hybrid density functionals in solid state chemistry. *Struct Bond 113* (2004), 171–232.

[42] CORNELL, R. The iron oxides : structure, properties, reactions, occurrences, and uses. *Wiley-VCH, Weinheim* (2003).

[43] COX, P. A. *Transition Metal Oxides*. Clearendon Press, Oxford, 1992.

[44] DE LEEUW, N., AND COOPER, T. Surface simulation studies of the hydration of white rust fe(oh)$_2$, goethite α-feo(oh) and hematite α-fe$_2$o$_3$. *Geochimica Et Cosmochimica Acta 71* (2007), 1655–1673.

[45] DELLAGO, C., AND BOLHUIS, P. Transition path sampling and other advanced simulation techniques for rare events. *Adv. Polym. Sci* (2008).

[46] DUDAREV, S., BOTTON, G., SAVRASOV, S., HUMPHREYS, C., AND SUTTON, A. Electron-energy-loss spectra and the structural stability of nickel oxide: An lsda+u study. *Physical Review B 57* (1998), 1505–1509.

[47] DUPONT, T., HOFFMAN, J., JOHNSON, C., KIRBY, R. C., LARSON, M. G., LOGG, A., AND SCOTT, L. R. *The FEniCS project*. Chalmers Finite Element Centre, Chalmers University of Technology, 2003.

[48] FENTER, P., AND STURCHIO, N. Mineral-water interfacial structures revealed by synchrotron x-ray scattering. *Progress in Surface Science 77* (2004), 171–258.

[49] FETTER, A. L., AND WALECKA, J. D. *Quantum theory of many-particle systems*. McGraw-Hill, New York, 1971.

[50] FIELD, M., BASH, P., AND KARPLUS, M. A combined quantum mechanical and molecular mechanical potential for molecular dynamics simulations. *Journal of Computational Chemistry 11* (1990), 700–733.

[51] FORESMAN, J. B., AND FRISCH, A. *Exploring Chemistry with Electronic Structure Methods*. Gaussian, 1996.

[52] FRANK, R. L., LIEB, E. H., SEIRINGER, R., AND THOMAS, L. E. Bipolaron and n-polaron binding energies. *Physical review letters 104*, 21 (2010), 210402.

[53] FRANK, R. L., LIEB, E. H., SEIRINGER, R., AND THOMAS, L. E. Stability and absence of binding for multi-polaron systems. *Publications mathématiques de l'IHÉS 113*, 1 (2011), 39–67.

[54] GANDER, M., AND VANDEWALLE, S. Analysis of the parareal time-parallel time-integration method. *Siam J Sci Comput 29* (2007), 556–578.

[55] GEORGES, A., KOTLIAR, G., KRAUTH, W., AND ROZENBERG, M. Dynamical mean-field theory of strongly correlated fermion systems and the limit of infinite dimensions. *Rev Mod Phys 68* (1996), 13–125.

[56] GHOSE, S., WAYCHUNAS, G., TRAINOR, T., AND ENG, P. Hydrated goethite (alpha-feooh) (100) interface structure: Ordered water and surface functional groups. *Geochim Cosmochim Ac 74* (2010), 1943–1953.

[57] GOLUB, G. H. *Matrix Computations*. Johns Hopkins Press, 1996.

[58] GONTIER, D. Existence of minimizers for Kohn–Sham within the local spin density approximation. *Nonlinearity 28*, 1 (2015), 57.

[59] GRIESEMER, M., AND HANTSCH, F. Unique solutions to Hartree–Fock equations for closed shell atoms. *Arch. Rational Mech. Anal. 203*, 3 (2012), 883–900.

[60] HACKBUSCH, W. *Multi-grid methods and applications*, vol. 4. Springer-Verlag Berlin, 1985.

[61] HAMANN, D. Generalized norm-conserving pseudopotentials. *Physical Review B 40* (1989), 2980–2987.

[62] HAMANN, D., SCHLUTER, M., AND CHIANG, C. Norm-conserving pseudopotentials. *Physical Review Letters 43* (1979), 1494–1497.

[63] HARRISON, R. J., FANN, G. I., YANAI, T., GAN, Z., AND BEYLKIN, G. Multiresolution quantum chemistry: Basic theory and initial applications. *The Journal of chemical physics 121*, 23 (2004), 11587–11598.

[64] HEAD-GORDON, T., AND HURA, G. Water structure from scattering experiments and simulation. *Chemical Reviews 102* (2002), 2651–2670.

[65] HEHRE, W. J., STEWART, R. F., AND POPLE, J. A. self-consistent molecular-orbital methods. i. use of gaussian expansions of slater-type atomic orbitals. *The Journal of Chemical Physics 51*, 6 (1969), 2657–2664.

[66] HELD, K. Electronic structure calculations using dynamical mean field theory. *Adv. Phys. 56* (2007), 829.

[67] HIRSCH, J. E., AND FYE, R. M. Monte carlo method for magnetic impurities in metals. *Physical Review Letters 56* (1986), 2521.

[68] HOCHELLA, M., LOWER, S., MAURICE, P., PENN, R., SAHAI, N., SPARKS, D., AND TWINING, B. Nanominerals, mineral nanoparticles, and earth systems. *Science 319* (2008), 1631–1635.

[69] HOHENBERG, P., AND KOHN, W. Inhomogeneous electron gas. *Physical Review B 136* (1964), B864.

[70] HU, H. Electronic structure models: Solution theory, linear scaling methods, and stability analysis. *UCSD Ph.D. Thesis* (2014).

[71] JONES, F., ROHL, A., FARROW, J., AND VAN BRONSWIJK, W. Molecular modeling of water adsorption on hematite. *Phys Chem Chem Phys 2* (2000), 3209–3216.

[72] KAPPLER, A., AND NEWMAN, D. Formation of fe(iii)-minerals by fe(ii)-oxidizing photoautotrophic bacteria 1. *Geochimica et Cosmochimica Acta 68* (2004), 1217–1226.

[73] KATZ, J., GILBERT, B., ZHANG, X., ATTENKOFER, K., FALCONE, R., AND WAYCHUNAS, G. Observation of transient iron(ii) formation in dye-sensitized iron oxide nanoparticles by time-resolved x-ray spectroscopy. *J Phys Chem Lett 1* (2010), 1372–1376.

[74] KENDALL, R. A., APRÀ, E., BERNHOLDT, D. E., BYLASKA, E. J., DUPUIS, M., FANN, G. I., HARRISON, R. J., JU, J., NICHOLS, J. A., NIEPLOCHA, J., ET AL. High performance computational chemistry: An overview of nwchem a distributed parallel application. *Computer Physics Communications 128*, 1 (2000), 260–283.

[75] KERISIT, S. Water structure at hematite-water interfaces. *Geochimica Et Cosmochimica Acta 75* (2011), 2043–2061.

[76] KERISIT, S., AND ROSSO, K. Computer simulation of electron transfer at hematite surfaces. *Geochim Cosmochim Ac 70* (2006), 1888–1903.

[77] KIRR, E., KEVREKIDIS, P. G., AND PELINOVSKY, D. E. Symmetry-breaking bifurcation in the nonlinear Schrödinger equation with symmetric potentials. *Communications in mathematical physics 308*, 3 (2011), 795–844.

[78] KOHANOFF, J. Phonon spectra from short non-thermally equilibrated molecular dynamics simulations. *Computational Materials Science 2* (1994), 221–232.

[79] KOHN, S. R., WEARE, J. H., ONG, M. E. G., AND BADEN, S. B. Parallel adaptive mesh refinement for electronic structure calculations. *Proceedings of the Eighth SIAM Conference on Parallel Processing for Scientific Computing* (1997).

[80] KOHN, W., AND SHAM, L. Self-consistent equations including exchange and correlation effects. *Phys Rev 140* (1965), A1133–A1138.

[81] KOTLIAR, G., SAVRASOV, S., HAULE, K., OUDOVENKO, V.S., PARCOLLET, O., AND MARIANETTI, C. Electronic structure calculations with dynamical mean-field theory. *Rev Mod Phys 78* (2006), 865–951.

[82] KOTLIAR, G., AND VOLLHARDT, D. Strongly correlated materials: Insights from dynamical mean-field theory. *Physics Today 57* (2004), 53–59.

[83] KUBICKI, J., PAUL, K., AND SPARKS, D. Periodic density functional theory calculations of bulk and the (010) surface of goethite. *Geochemical Transactions 9* (2008a), 4.

[84] KUBICKI, J., PAUL, K., AND SPARKS, D. Periodic density functional theory calculations of bulk and the (010) surface of goethite. *Geochemical Transactions 9* (2008b).

[85] LARESE-CASANOVA, P., AND SCHERER, M. Fe(ii) sorption on hematite: new insights based on spectroscopic measurements. *Environ Sci Technol 41* (2007), 471–477.

[86] LENZMANN, E. Uniqueness of ground states for pseudorelativistic Hartree equations. *Analysis & PDE 2*, 1 (2009), 1–27.

[87] LIAO, P., KEITH, J., AND CARTER, E. Water oxidation on pure and doped hematite (0001) surfaces: Prediction of co and ni as effective dopants for electrocatalysis. *Journal of the American Chemical Society 134* (2012), 13296–13309.

[88] LIEB, E. H. Thomas-Fermi and related theories of atoms and molecules. *Reviews of Modern Physics 53*, 4 (1981), 603.

[89] LIEB, E. H., AND LOSS, M. *Analysis*, 2nd ed. American Mathematical Society, 2001.

[90] LIEB, E. H., AND SIMON, B. The Hartree-Fock theory for Coulomb systems. *Communications in Mathematical Physics 53*, 3 (1977), 185–194.

[91] LIONS, J., MADAY, Y., AND TURINICI, G. A "parareal" in time discretization of pde's. *Cr Acad Sci I-Math 332* (2001), 661–668.

[92] LIONS, P.-L. Solutions of Hartree-Fock equations for Coulomb systems. *Communications in Mathematical Physics 109*, 1 (1987), 33–97.

[93] LIU, P., KENDELEWICZ, T., BROWN JR, G., NELSON, E., AND CHAMBERS, S. Reaction of water vapor with α-Al_2O_3(0001) and α-Fe_2O_3(0001) surfaces: synchrotron x-ray photoemission studies and thermodynamic calculations. *Surface Science 417* (1998), 53–65.

[94] LO, C., TANWAR, K., CHAKA, A., AND TRAINOR, T. Density functional theory study of the clean and hydrated hematite ($1\bar{1}02$) surfaces. *Physical Review B 75* (2007), 075425.

[95] LOGG, A., MARDEL, K. M., AND WELLS, G., Eds. *Automated Solution of Differential Equations by the Finite Element method: The FEniCS Book*. Springer, 2012.

[96] LOGG, A., AND WELLS, G. N. Dolfin: Automated finite element computing. *ACM Transations on Mathematical Software (TOMS) 37*, issue 2, article 20 (2010).

[97] LYNE, P., HODOSCEK, M., AND KARPLUS, M. A hybrid qm-mm potential employing hartree-fock or density functional methods in the quantum region. *The Journal of Physical Chemistry A 103* (1999), 3462–3471.

[98] MARSMAN, M., PAIER, J., STROPPA, A., AND KRESSE, G. Hybrid functionals applied to extended systems. *J Phys-Condens Mat 20* (2008).

[99] MARX, D., AND HUTTER, J. Ab initio molecular dynamics : basic theory and advanced methods. *Cambridge University Press, Cambridge* (2012).

[100] MASLEN, E., STRELTSOV, V., STRELTSOVA, N., AND ISHIZAWA, N. Synchrotron x-ray study of the electron density in α-fe$_2$o$_3$. *Acta Crystallographica 50* (1994), 435–441.

[101] MCCORMICK, S. F. *Multigrid methods*, vol. 3. siam, 1987.

[102] NAVROTSKY, A., MAZEINA, L., AND MAJZLAN, J. Size-driven structural and thermodynamic complexity in iron oxides. *Science 319* (2008), 1635–1638.

[103] NEGELE, J. W., ORLAND, AND HENRI. *Quantum many-particle systems*. MA Perseus Books, 1998.

[104] NEWMAN, D. Feasting on minerals. *Science 12* (2010), 793.

[105] OLIVER, G. L., AND PERDEW, J. P. Spin-density gradient expansion for kinetic energy. *Physical Review A 20*, 2 (1979), 397–403.

[106] PARR, R., AND YANG, W. Density-functional theory of the electronic-structure of molecules. *Annual Review of Physical Chemistry 46* (1995), 701–728.

[107] PARR, R. G. *Quantum Theory of Molecular Electronic Structure*. W. A. Benjamin, 1972.

[108] PARR, R. G., AND YANG, W. *Density-Functional Theory of Atoms and Molecules*. Oxford Science Publications, 1989.

[109] PENG, H., AND PERDEW, J. P. Synergy of van der waals and self-interaction corrections in transition metal monoxides. *Physical Review B 96* (2017), 100101 1–5.

[110] PICKETT, W. Pseudopotential methods in condensed matter applications. *Computer Physics Reports 9* (1989), 115–197.

[111] PICKETT, W., ERWIN, S., AND ETHRIDGE, E. Reformulation of the lda+u method for a local-orbital basis. *Phys Rev B 58* (1998), 1201–1209.

[112] POZAN, Z., AND HENKELMAN, G. Hybrid density functional theory band structure engineering in hematite. *The Journal of Chemical Physics 134* (2011), 224706–1–9.

[113] RAPPOPORT, D., CRAWFORD, N., FURCHE, F., AND BURKE, K. Approximate density functionals: Which should i choose? *Encylopedia of Inorganic and Bioinorganic Chemistry* (2011).

[114] REED, M., AND SIMON, B. *Analysis of Operators, Vol. IV of Methods of Modern Mathematical Physics*. New York, Academic Press, 1978.

[115] REMLER, D., AND MADDEN, P. Molecular-dynamics without effective potentials via the car-parrinello approach. *Molecular Physics 70* (1990), 921–966.

[116] RICAUD, J. *Symétrie et brisure de symétrie pour certains problèmes non linéaires.* PhD thesis, Université de Cergy Pontoise, 2017.

[117] RICAUD, J. Symmetry breaking in the periodic Thomas–Fermi–Dirac–von Weizsäcker model. *arXiv preprint arXiv:1703.07284* (2017).

[118] RICCARDI, D., SCHAEFER, P., YANG, Y., YU, H., GHOSH, N., PRAT-RESINA, X., KÖNIG, P., LI, G., XU, D., GUO, H., ELSTNER, M., AND CUI, Q. Development of effective quantum mechanical/molecular mechanical (qm/mm) methods for complex biological processes. *The Journal of Physical Chemistry B 110* (2006), 6458–6469.

[119] RODEN, E. Geochemical and microbiological controls on dissimilatory iron reduction. *Comptes Rendus Geoscience 338* (2006), 456–467.

[120] ROEDDER, E. Fluid inclusions. *Mineralogical Society of America* (1984).

[121] ROHRBACH, A., HAFNER, J., AND KRESSE, G. Ab initio study of the (0001) surfaces of hematite and chromia: Influence of strong electronic correlations. *Physical Review B 70* (2004), 125426.

[122] ROLLMANN, G., ROHRBACH, A., ENTEL, P., AND HAFNER, J. First-principles calculation of the structure and magnetic phases of hematite. *Physical Review B 69* (2004), 165107.

[123] ROSSO, K., AND DUPUIS, M. Electron transfer in environmental systems: a frontier for theoretical chemistry. *Theor Chem Acc 116* (2006), 124–136.

[124] ROSSO, K., YANINA, S., AND GORSKI, C. Connecting observations of hematite ($\alpha - Fe_2O_3$) growth catalyzed by fe(ii). *Environ Sci Technol 44* (2010), 61–67.

[125] RUIZ, D. On the Schrödinger–Poisson–Slater system: behavior of minimizers, radial and nonradial cases. *Archive for rational mechanics and analysis 198*, 1 (2010), 349–368.

[126] RUSKAI, M. B., AND STILLINGER, F. H. Binding limit in the Hartree approximation. *J. Math. Phys. 25*, 6 (1984), 2099–2103.

[127] SAAD, Y., AND SCHULTZ, M. H. Gmres: A generalized minimal residual algorithm for solving nonsymmetric linear systems. *SIAM J. Sci. Stat. Comput. 7*, 3 (1986), 856–869.

[128] SENN, H., AND THIEL, W. Qm/mm methods for biological systems. *Reiher, M. (Ed.), Atomistic Approaches in Modern Biology. Springer Berlin Heidelberg* (2007), 173–290.

[129] SHICK, A., LIECHTENSTEIN, A., AND PICKETT, W. Implementation of the lda+u method using the full-potential linearized augmented plane-wave basis. *Physical Review B 60* (1999), 10763–10769.

[130] STADELE, M., MAJEWSKI, J., VOGL, P., AND GORLING, A. Exact kohn-sham exchange potential in semiconductors. *Phys Rev Lett 79* (1997), 2089–2092.

[131] STADELE, M., MOUKARA, M., MAJEWSKI, J., VOGL, P., AND GORLING, A. Exact exchange kohn-sham formalism applied to semiconductors. *Phys Rev B 59* (1999), 10031–10043.

[132] STUMM, W., AND MORGAN, J. Aquatic chemistry: An introduction emphasizing chemical equilibria in natural waters. *Wiley Interscience* (1981).

[133] STUMM, W., AND SULZBERGER, B. The cycling of iron in natural environments: Considerations based on laboratory studies of heterogeneous redox processes. *Geochimica Et Cosmochimica Acta 56* (1992), 3233–3257.

[134] SULEM, C., AND SULEM, P.-L. *The nonlinear Schrödinger equation: self-focusing and wave collapse*, vol. 139. Springer Science & Business Media, 1999.

[135] SZABO, A., AND OSTLUND, N. S. *Modern Quantum Chemistry*. Dover Publications, 1989.

[136] TANWAR, K., LO, C., ENG, P., CATALANO, J., WALKO, D., BROWN, G., WAYCHUNAS, G., CHAKA, A., AND TRAINOR, T. Surface diffraction study of the hydrated hematite ($1\bar{1}02$) surface. *Surface Science 601* (2007), 460–474.

[137] TANWAR, K., PETITTO, S., GHOSE, S., ENG, P., AND TRAINOR, T. Structural study of fe(ii) adsorption on hematite. *Geochimica Et Cosmochimica Act 72* (2008), 3311–3325.

[138] TANWAR, K.S., P. S. G. S. E. P., AND TRAINOR, T. Fe(ii) adsorption on hematite (0001). *Geochimica Et Cosmochimica Acta 73* (2009), 4346–4365.

[139] TATEBE, O. The multigrid preconditioned conjugate gradient method, 1993.

[140] TAYLOR, K., AND KONHAUSER, K. Iron in earth surface systems: A major player in chemical and biological processes. *Elements 7* (2011), 83–87.

[141] TETER, M. Additional condition for transferability in pseudopotentials. *Physical Review B 48* (1993), 5031–5041.

[142] THOMAS, M., BREHM, M., FLIGG, R., VÖHRINGER, P., AND KIRCHNER, B. Computing vibrational spectra from ab initio molecular dynamics. *Physical Chemistry Chemical Physics 15* (2013), 6608–6622.

[143] TRAINOR, T., CHAKA, A., ENG, P., NEWVILLE, M., WAYCHUNAS, G., CATALANO, J., AND BROWN JR, G. Structure and reactivity of the hydrated hematite (0001) surface. *Surface Science 573* (2004), 204–224.

[144] VALENTIN, D., C., PACCHIONI, G., AND SELLONI, A. Electronic structure of defect states in hydroxylated and reduced rutile tiO_2(110) surfaces. *Phys Rev Lett 97* (2006).

[145] VALIEV, M., BYLASKA, E., GOVIND, N., KOWALSKI, K., STRAATSMA, T., VAN DAM, H., WANG, D., NIEPLOCHA, J., APRA, E., WINDUS, T., AND DE JONG, W. Nwchem: a comprehensive and scalable open-source solution for large scale molecular simulations. *Comput. Phys. Commun. 181* (2010), 1477.

[146] VALIEV, M., AND ET AL. Nwchem: a comprehensive and scalable open-source solution for large scale molecular simulations. *Computer Physics Communications 181*, 9 (2010), 1477–1489.

[147] VAN EMDEN, H., AND YANG, U. M. Boomer amg: A parallel algebraic multigrid solver and preconditioner. *Applied Numerical Mathematics 41* (2002), 155–177.

[148] WANG, L., MAXISCH, T., AND CEDER, G. Oxidation energies of transition metal oxides within the gga+u framework. *Physical Review B 73* (2006), 195107.

[149] WEBER, K., ACHENBACH, L., AND COATES, J. Microorganisms pumping iron: anaerobic microbial iron oxidation and reduction. *Nat Rev Micro 4* (2006), 752–764.

[150] WEINSTEIN, M. I. Lyapunov stability of ground states of nonlinear dispersive evolution equations. *Communications on Pure and Applied Mathematics 39*, 1 (1986), 51–67.

[151] YANINA, S., AND ROSSO, K. Linked reactivity at mineral-water interfaces through bulk crystal conduction. *Science 320* (2008), 218–222.

[152] YIN, S., AND ELLIS, D. H_2o adsorption and dissociation on defective hematite (0001) surfaces: A dft study. *Surface Science 602* (2008), 2047–2054.

[153] YIN, S., AND ELLIS, D. Dft studies of cr(vi) complex adsorption on hydroxylated hematite (012) surfaces. *Surface Science 603* (2009), 736–746.

[154] YIN, S., MA, X., AND ELLIS, D. Initial stages of h_2o adsorption and hydroxylation of fe-terminated α-fe_2o_3(0001) surface. *Surface Science 601* (2007), 2426–2437.

[155] ZHAO, Y., AND TRUHLAR, D. Density functionals with broad applicability in chemistry. *Accounts Chem Res 41* (2008), 157–167.